X-ray Study of Stellar Winds with Suzaku

Yoshiaki Hyodo

Department of Physics, Graduate School of Science, Kyoto University
Kitashirakawa Oiwake-cho, Sakyo-ku, Kyoto, 606-8502, Japan
hyodo@cr.scphys.kyoto-u.ac.jp

This thesis was submitted to the Department of Physics,
Graduate School of Science, Kyoto University
on January 5 2009
in partial fulfillment of the requirements
for the degree of Doctor of Philosophy in physics.

Abstract

Stellar winds from massive stars play an important role for dynamical and chemical evolution of galaxies. To evaluate their effects in a galaxy scale, both the total number and the properties of massive stars should be understood. Most massive stars have soft X-ray emission, while some have additional hard emission. Although it is indicated that the binarity is important, the condition for hard X-ray production has not yet been elucidated. Also, some massive star clusters exhibit diffuse (pc scale) X-ray emission, where stellar winds may be depositing energy to the interstellar space. However, previous studies were not able to clarify the origin of the diffuse emission. It is even unclear whether the emission is physically related to the star cluster or not.

The X-ray Imaging Spectrometer (XIS) on board Suzaku has a good energy resolution, a low and stable background, and a large effective area, which are suited for narrow-band surveys and spectroscopy of both point-like and extended X-ray emission. Using the XIS, we performed a very deep survey in the direction of the central region of our Galaxy and pointing observations of three well-known star forming regions in our Galaxy (M 17, the Carina Nebula, and the Arches cluster).

A bright point-like source (CXOGC J174645.3–281546) was found in the 6.7 keV intensity map of the Galactic center region. The temperature and luminosity are similar to those of wind-collision binary. The spectral energy distribution in the infrared is very similar to those of eponymous Quintuplet cluster members, indicating that the source is a WC star+OB star binary.

We also present the results of X-ray spectroscopy of nine massive stars in M 17, the Carina nebula, and the Arches cluster. Many sources show hard X-ray emission. We obtained important clues for hard X-ray production mechanism in massive star binaries. WR 25 (WN6+O4f) in the Carina region shows hard X-ray emission with a flux variation correlated with the binary orbital phase, while the close binary HD 93205 (O3+O8) lacks hot component and is stable. These two facts indicate that the binary separation is a key parameter for hard X-ray emission. We speculate that the other two massive stars OI 352 in M 17, and HD 93250 in the Carina Nebula with hard X-ray emission are also colliding-wind binaries.

A variety of diffuse emission is apparently associated with some massive star clusters. We argue that the diffuse source in M 17 and in the west to η Carinae are prototypical stellar wind bubbles; the absorption columns typical to these regions indicate that the diffuse emission is physically associated with the star clusters and the O/Fe abundance ratio ($\lesssim$ 1 solar) is too low for supernova remnants caused by core-collapse type supernovae. On the other hand, the diffuse emission in the south side of η Carinae is unlikely to have physical relation with the Carina Nebula, because the absorption column is very low ($N_{\rm H} < 6 \times$

10^{20} cm^{-2}). A possible nature is a foreground type Ia supernova remnant. The absorption column of diffuse emission in the Arches cluster is consistent with that of the Galactic center, indicating a physical relation to the Arches cluster. Although massive stars in the Arches cluster are the sources of strong stellar wind, the diffuse emission is unlikely to be hot plasma created by the stellar wind. It shows a strong line from neutral iron. The origin is likely due to X-ray and/or electron fluorescent, but the flux of the X-ray photons or electrons are extremely insufficient to produce the diffuse X-rays.

Contents

List of Figures

List of Tables

Chapter 1

Introduction

The outer atmosphere of massive stars obtains momentum from UV photons radiated in their photosphere, and eventually the velocity exceeds the star's surface escape velocity. This outflow is called stellar wind and shows a terminal velocity (v_∞) of $\sim 10^3$ km s^{-1} and a mass-loss rate of 10^{-7}–$10^{-5} M_\odot$ yr^{-1}. The integrated mass, momentum, and energy deposited to the surrounding environment via stellar winds through the lifetime can be comparable to those by a supernova (SN) at its death (Leitherer et al., 1992). Stellar winds also contaminate the environment chemically by releasing heavy metals produced via thermonuclear reactions.

Stellar winds make a ring nebula around individual stars by sweeping out their surrounding matter (Chu, 1991). The most dramatic case is seen in starburst galaxies (e.g., M 82), in which a galaxy scale bubble is produced by superwind, a combination of stellar winds and supernovae (McCarthy et al., 1987). In our Galaxy, stellar winds is one of the prospective candidates for large scale structures, such as the bipolar dust lobe in the Galactic center (Bland-Hawthorn & Cohen, 2003), the Galactic ridge X-ray emission (Kaneda et al., 1997; Ebisawa et al., 2001), and the Galactic center diffuse X-ray emission (Koyama et al., 1989; Yamauchi et al., 1990). Of course, SN explosions are vital in these phenomena. However, the pre-explosion effects are equally important, which is poorly understood.

The interaction between stellar winds and ambient matter, hydrodynamic instability within stellar winds, collision of two stellar winds, or magnetically confined winds cause a shock to produce hot ($10^6 - 10^7$ K) plasma that emits X-rays. X-ray photons can penetrate through the natal molecular cloud from which massive stars are born, and also the interstellar matter in the Galactic plane where most of massive stars exist (Wood & Churchwell, 1989). Emission lines from highly ionized atoms in the X-ray band enable a reliable derivation of elemental abundances and plasma temperature because they are based on simple physics. Therefore, X-ray is an important yet unexplored tool to investigate the physics and chemistry of stellar winds quantitatively.

This thesis focuses on the X-ray emission of stellar winds from massive stars and massive star clusters using the Suzaku satellite. Other X-ray satellites, XMM-Newton and Chandra with better spatial resolutions, are supplementary used to investigate the point source properties. Infrared data by ground-based and space-based observatories in infrared bands are also used to constrain the nature of X-ray sources.

We select four fields that represents a wide variety of phenomena related to the X-ray emission from massive stars. The first field is the central region of our Galaxy. We perform a very deep survey of the Galactic center region to find new massive stars. We also select three Galactic fields, M 17, the Carina Nebula, and the Arches cluster, because these regions have unambiguous diffuse X-ray emission but with unclear physical origin.

The plan of this thesis is as follows. In chapter 2, we review the theoretical basis of stellar winds and survey recent observational results to clarify the problems to address in this work. The basic properties of the Suzaku observatory are shown in chapter 3. We present the timing and spectral features of massive stars and star clusters in our Galaxy obtained with Suzaku in chapter 4. In chapter 5, we discuss the nature and the emission mechanisms for both the discrete sources and diffuse emission. Finally in chapter 6, we summarize the results and conclude the thesis.

Chapter 2

Review

In the first subsection, we review the structure and evolution of massive stars. In section 2.2, the spatial distribution of WR stars is described. Theoretical studies on the X-ray emission from massive stars are summarized in the following subsections.

Contents

2.1 Evolution of Massive Stars

The radiation energy of stars at the main-sequence phase is produced by the nuclear fusion of H. The major energy-generating process of stars with mass of $\lesssim 1.5\ M_\odot$ is the pp chain,

$$\begin{cases} {}^1\mathrm{H} + {}^1\mathrm{H} & \rightarrow {}^2\mathrm{H} + \mathrm{e}^+ + \nu_\mathrm{e} \\ {}^2\mathrm{H} + {}^1\mathrm{H} & \rightarrow {}^3\mathrm{He} + \gamma \\ {}^3\mathrm{He} + {}^3\mathrm{He} & \rightarrow {}^4\mathrm{He} + 2\ {}^1\mathrm{H}. \end{cases} \tag{2.1}$$

Considering that the first and second steps occur twice for the third one, the net process is $4\,{}^1\mathrm{H} \rightarrow {}^4\mathrm{He} + 2\gamma + 2\nu_\mathrm{e} + 2\mathrm{e}^+$. The rate controlling reaction is the first step, which involves a weak interaction. The energy-generating rate is expressed as $\epsilon_\mathrm{pp} = 5.3 \times 10^5\, \rho X^2 T_7^{-2/3} \exp\left(-15.7 T_7^{-1/3}\right)$ erg s^{-1} g^{-1}, where ρ is the density in g cm^{-3},

X is the H mass fraction, and T_7 is the temperature in 10^7 K.

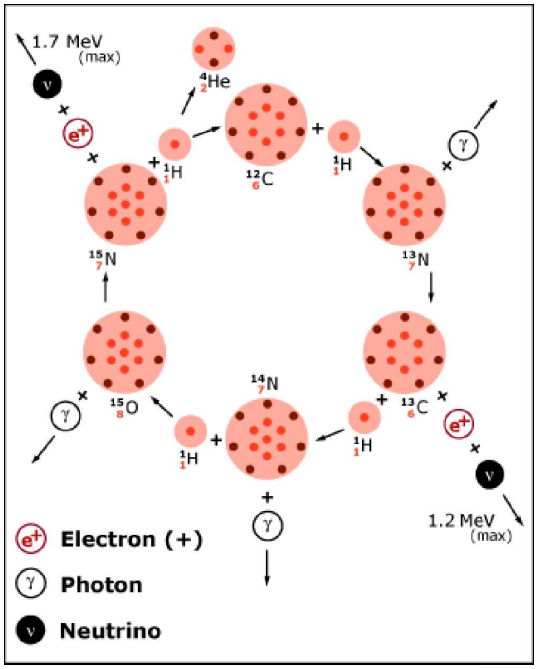

Figure 2.1: Diagram of CNO cycle (Bahcall, 1969). Protons and neutrons are shown in red and black dots, respectively.

Hydrogen burning can take place in another way, utilizing C, N, and O as catalysts. As shown in figure 2.1, the net reaction is $4\,{}^1\mathrm{H} \rightarrow {}^4\mathrm{He} + 3\gamma + 2\nu_\mathrm{e} + 2\mathrm{e}^+$. Since reaction involving C, N, and O have higher potential barriers than those involving only H and He, the CNO cycle requires a higher temperature than $\sim 1.8 \times 10^7$ K. The slowest step is the proton capture of ${}^{14}\mathrm{N}$ (${}^{14}\mathrm{N} + {}^1\mathrm{H} \rightarrow {}^{15}\mathrm{O} + \gamma$). The energy-generating rate is expressed as $\epsilon_\mathrm{CNO} = 4.9 \times 10^{26}\,\rho\,X\,Z_\mathrm{CNO}\,T_7^{-2/3} \exp\left(-70.5\,T_7^{-1/3}\right)$ erg s^{-1} g^{-1}, where Z_CNO is the mass fraction of C, N, and O.

Figure 2.2 shows the energy production rate of both processes at the center of a star. With the central temperature of 1.6×10^7 K for the Sun, the energy generation is dominated ($> 90\%$) by the pp chain. Since the reaction rate of the CNO cycle is much higher than that of pp chain ($\epsilon_\mathrm{CNO} \propto T^{19}$ and $\epsilon_\mathrm{pp} \propto T^4$ at $T = 1.6 \times 10^7$ K) for higher temperatures, it dominates the hydrogen burning for massive stars.

The difference of the dominant hydrogen burning process causes the difference in stellar structure. In the inner part of low-mass stars, the energy is transferred by radiation since the temperature gradient of the pp chain is small, while that in massive stars is transported by convection. The energy transfer in the outer layer of high mass stars is dominated by

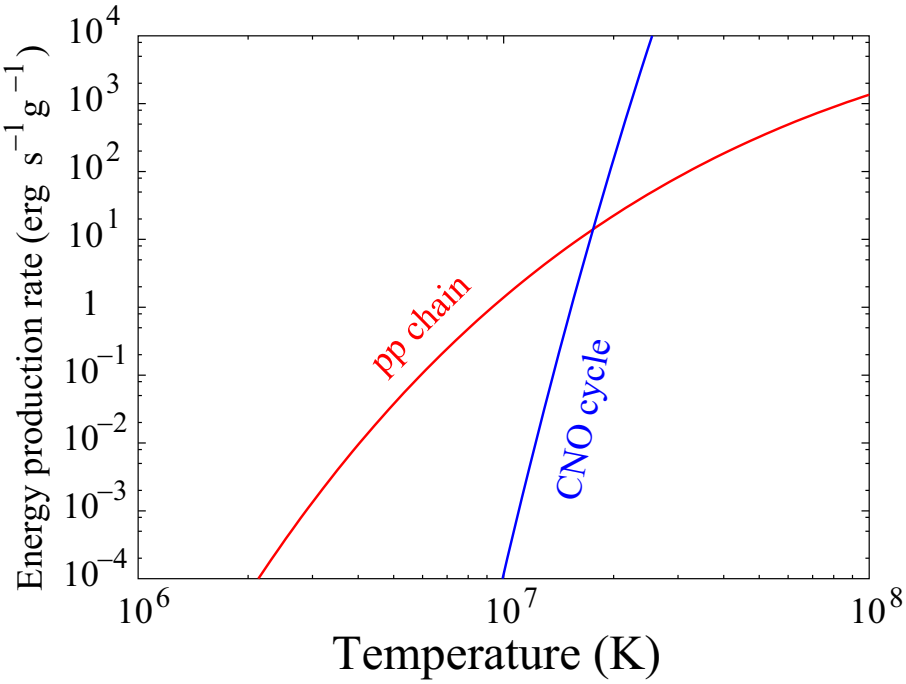

Figure 2.2: Energy production rate of the pp chain (red) and CNO cycle (blue) as a function of temperature. We adopted the values of the center of the Sun; $\rho = 156$, $X = 0.33$, $Z_{\rm CNO} = 0.005$ (Bahcall et al., 1995).

radiation, whereas that of low mass stars is by convection because of the high opacity due to the presence of H^-. A differential rotation can amplify the magnetic field in the outer layer of low mass stars, but not of high mass stars. Plasma production by magnetic reconnections (Shibata & Yokoyama, 1999) cannot take place in high mass stars.

When hydrogen is exhausted at the central core, the core starts to contract until He burning is ignited. Since the pressure gradient also rises, the star begins to expand and the effective temperature drops. Stars in this stage are called red giant.

If the initial mass exceeds $\sim 30 M_\odot$, the outer hydrogen layer is blown away by stellar winds and the helium layer is exposed without becoming a red giant. This class is called Wolf-Rayet stars, which is described in the next subsection. The post-main-sequence stellar evolution differs according to the initial mass ranges.

$$\begin{cases} \text{O–Of–BSG–LBV–WR–SN} & M_2 < M \\ \text{O–BSG–YSG–RSG–WR–SN} & M_1 < M < M_2 \\ \text{O–(BSG)–RSG–YSG–(Ceheid)–RSG–SN} & M < M_1, \end{cases} \tag{2.2}$$

where BSG, YSG, and RSG are blue, yellow, and red supergiants, respectively. LBV repre-

sents luminous blue variable. Various values are proposed for the lower- and upper- limits of initial mass depending on the calculation method, the metal abundance, and the initial spin period (Chiosi & Maeder, 1986; Maeder & Meynet, 1987; Meynet & Maeder, 2005). The typical values of M_1 and M_2 are ~ 25–40 and ~ 40–60, respectively.

2.2 Wolf-Rayet Stars

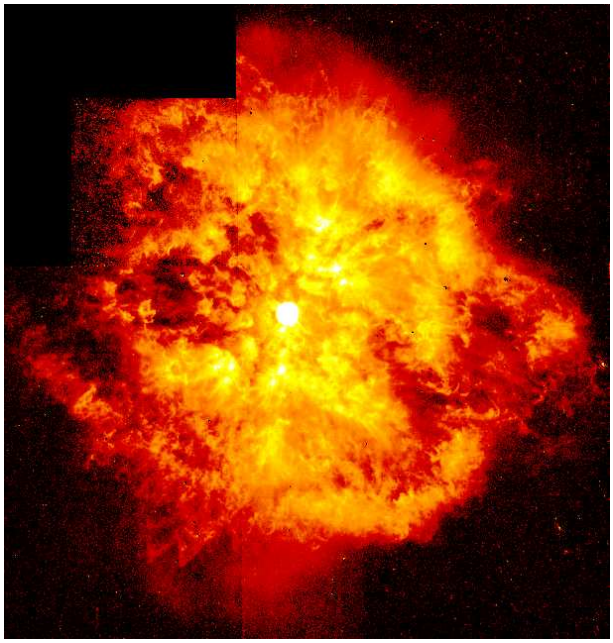

Figure 2.3: HST image of M1-67 around WR 124 (Grosdidier et al., 1998).

Wolf & Rayet (1867) discovered three peculiar early-type stars (now designated as HD 191765 = WR 134, HD 192103 = WR 135, HD 192641 = WR 137) having exceptionally broad emission lines in the Cygnus region. The widths of emission lines from highly excited He, C, and N are equivalent to Doppler velocities of $\sim 10^3$ km s^{-1}. This class of stars are named Wolf-Rayet (WR) stars after their discovery. Figure 2.3 shows the Hα image taken with the Hubble space telescope (Grosdidier et al., 1998). A typical spectrum of a WR star (WR 158) is shown in figure 2.4 (Rayner et al., 2003). Although the original definition of WR stars includes central stars in planetary nebulae (population II), we hereafter discuss only early-type stars (population I). Conti & Walborn (1976) suggested that WR stars are evolved massive stars that have lost the H shell through stellar winds with a mass-loss rate of 10^{-5}–10^{-4} $M_\odot$ yr^{-1}, and the "peeled onion skin" (Paczynski, 1973) is seen.

With the initial mass exceeding 20 $M_\odot$ (Meynet & Maeder, 2005), a WR star will cause a core-collapsed supernova (Type Ib or Ic). Actually, Soderberg et al. (2008) detected the moment that a WR star caused a supernova explosion for the first time with an intense X-ray outburst. Furthermore, WR stars are one of the strong candidates for the progenitors of gamma-ray bursts, the most energetic events in the universe. The pre-explosion activity also plays an important role by fueling mass, momentum, and energy into the circumstellar environment, which is comparable to that of a supernova (Leitherer et al., 1992).

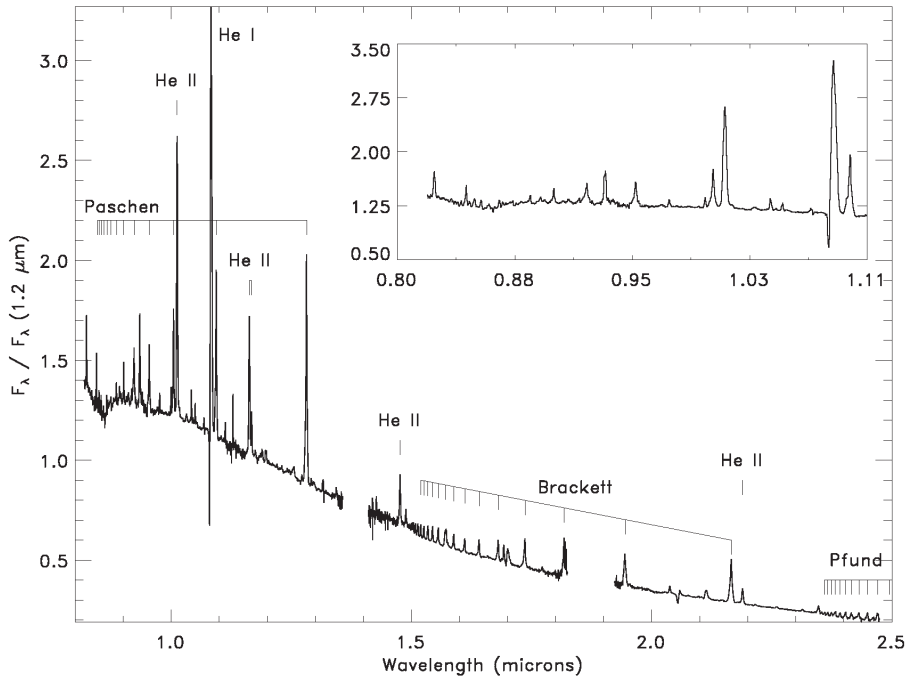

Figure 2.4: WR158 spectrum in the NIR bands. (Rayner et al., 2003)

WR stars are divided into three sub-groups according to line intensities (Beals , 1938; Barlow & Hummer, 1982).

$$\begin{cases} \text{WN star: N and He emission lines are intense.} \\ \text{WC star: He, C, and O emission lines are intense.} \\ \text{WO star: O emission lines are intense.} \end{cases} \tag{2.3}$$

Some exhibit the property of both the WN and WC types. In the latest catalogue compiling 298 WR stars identified in our Galaxy (van der Hucht, 2006), the spectral sub-type distribution is: 171 WN stars, 10 WN/WC stars, 113 WC stars, and 4 WO stars. In the local group besides our Galaxy, there are 132 stars in the Large Magellanic Cloud (Breysacher et al., 1999; Moffat, 2008), 12 stars in the Small Magellanic Cloud (Massey & Duffy, 2001; Massey et al., 2003), 29 stars in M 31 (Moffat & Shara, 1987; Armandroff & Massey, 1991), and 141 stars in M 33 (Massey & Johnson, 1998; Abbott et al., 2004).

Since the mass-loss rate of WR stars is larger than that of main-sequence O stars by more than ten-fold, it is vital to estimate the total number in the Galaxy. Although the number is rapidly increasing, it is considered that much more WR stars exist in the Galaxy (van der Hucht, 2001). Figure 2.5 shows the WR star surface number density as a function of Galactocentric distance. If we assume that the sample is complete between 7–12 kpc from the Galactic center, the difference between the extrapolated model and the observed number

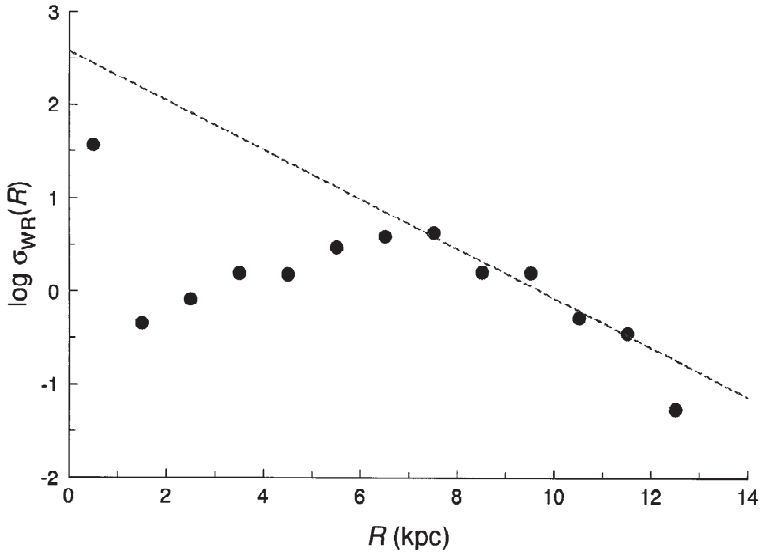

Figure 2.5: WR star surface number density as a function of Galactocentrinc distance (van der Hucht, 2001). The best-fit power-law is shown in the dashed line using the five points between 7 and 12 kpc.

implies that there are still more than 6000 WR stars undiscovered in the Galaxy. The inner part of the Galaxy is a promising region that harbors most of the unseen WR stars.

2.3 Diffuse X-ray Emission from Massive Stars

In early-type stars, stellar winds are driven by resonance lines in the UV bands. When an ion in the stellar atmosphere receives a photon corresponding to a resonance line, the ion is accelerated outward and the line is blue shifted. The ion can continue to be accelerated without shielding by inner ions. Since the opacity is large at resonance level, this mechanism effectively accelerate stellar winds (line-driven wind). The fundamental equation for spherically-symmetric winds is expressed as,

$$v\frac{dv}{dr} + \frac{1}{\rho}\frac{dp}{dr} + \frac{GM}{r^2}(1-\Gamma_{\rm R}) = 0, \tag{2.4}$$

in which $\Gamma_{\rm R}$ ($= \frac{4\pi r^2}{GMc}\int_0^\infty \kappa_\nu F_\nu d\nu$) represents the radiative pressure effect. The basic theory of stellar winds was constructed by Lucy & Solomon (1970) and Castor et al. (1975). Figure 2.6 shows the velocity structure of line-driven winds (Abbott, 1980). The velocity is shown in the unit of Mach number. The critical point is located in the supersonic region.

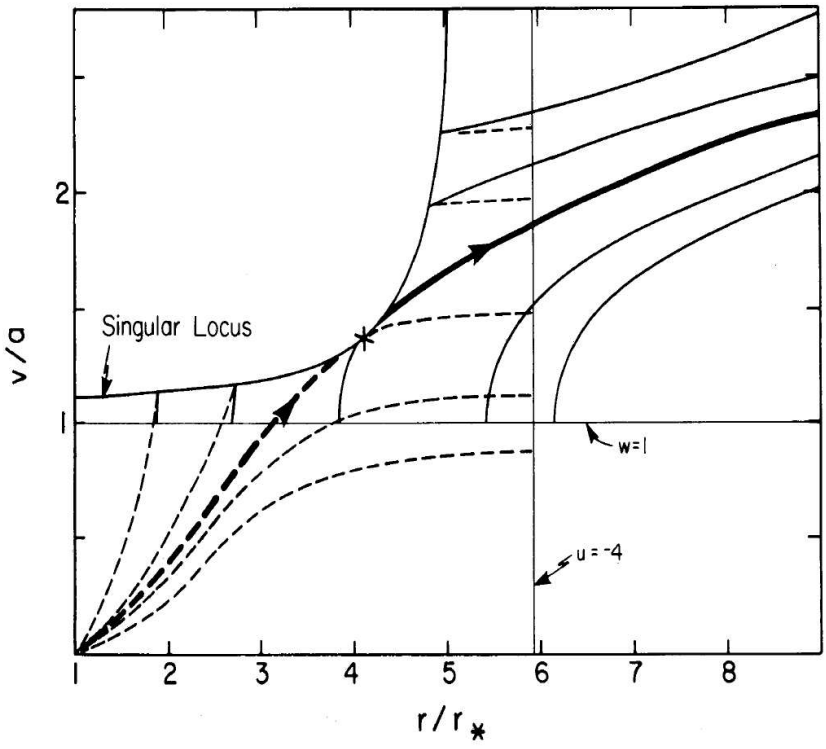

Figure 2.6: Velocity structure of line-driven stellar winds. The thick (dashed) line shows critical solution curve where a subsonic flow becomes a supersonic flow. The vertical line at $r/r_* \sim 6$ shows the critical point (Abbott, 1980).

Weaver et al. (1977) presented a self-similar solution of stellar winds interacting with the ISM. Radiative cooling and thermal conduction between the hot interior and ambient matters were taken into account. They showed a single O7 star ($\dot{M} = 10^{-6}\ M_{\odot}$) with an age of 10^6 yr forms a hot ($\sim 10^{6-7}$ K) bubble by the shock, which can be observed as soft extended (~ 10 pc) X-ray emission (figure 2.7).

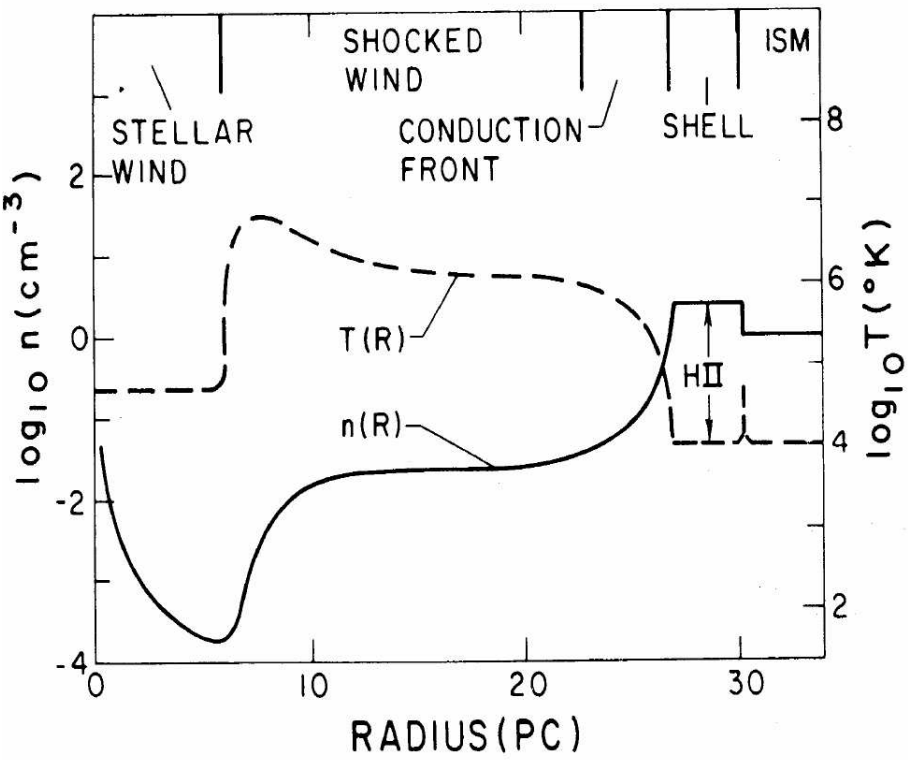

Figure 2.7: Temperature (dashed line) and density structure (solid line) of a stellar wind bubble around a single O7 star (Weaver et al., 1977).

Although Weaver et al. (1977) predicted X-ray emission with $L_{\rm X} \sim 2 \times 10^{33}$ erg s^{-1} from all O stars, there are only two single massive stars that showed X-ray emission from bubbles (S 308; Bochkarev 1988, NGC 6888; Wrigge et al. 1994, Wrigge 1999, Chu et al. 2003). Both of the central stars are Wolf-Rayet stars, hence no single early-type main-sequence star is known to show diffuse X-ray emission from the bubble. Figure 2.8 shows the composite image of NGC 6888.

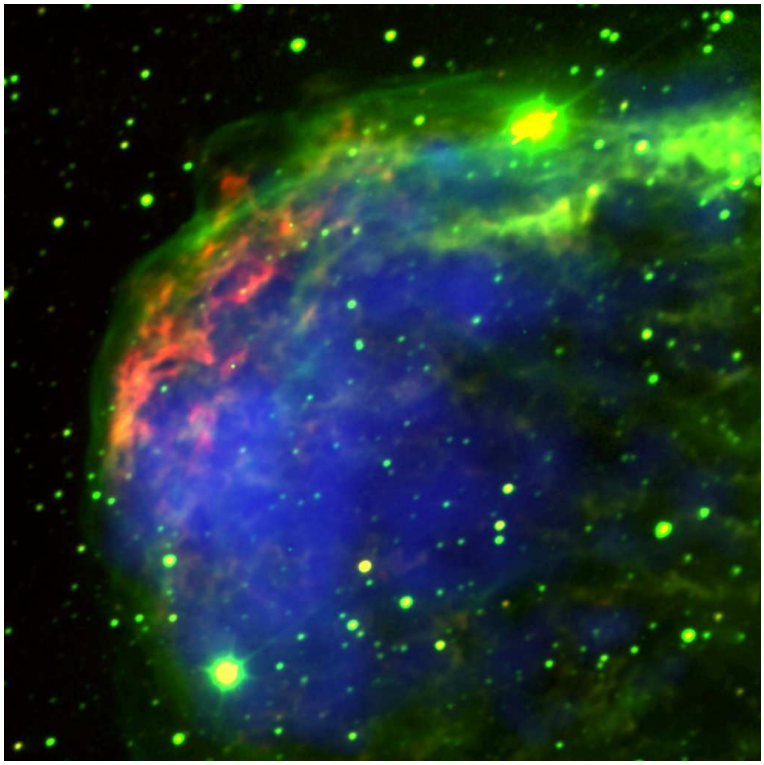

Figure 2.8: Color composite image of a stellar wind bubble around WR 136. The intensities of Hα line, O III line, and X-ray are shown in red, green, and blue respectively. The central star is out of the FOV. (Chandra Photo Album: http://chandra.harvard.edu/photo/2003/ngc6888/)

2.4 Point-like X-ray Emission from Massive Stars

The first detections of X-ray emission from early-type stars were made with the Einstein observations of the Cyg OB2 region and the Carina Nebula (Harnden et al., 1979; Seward et al., 1979). It is hard to explain the emission with coronal activity, since X-ray emission from corona should suffer significant photoelectric absorption by stellar wind, which is absent in the observed spectra. X-ray emission should arise farther out in the wind. The X-ray luminosity in the 0.2–4.0 keV band shows strong linear correlation $L_{\rm X}/L_{\rm bol} \sim 10^{-7}$ (Harnden et al., 1979; Pallavicini et al., 1981). The correlation is independent of the spectral type between A5–O3, indicating a universal mechanism for X-ray emission (figure 2.9).

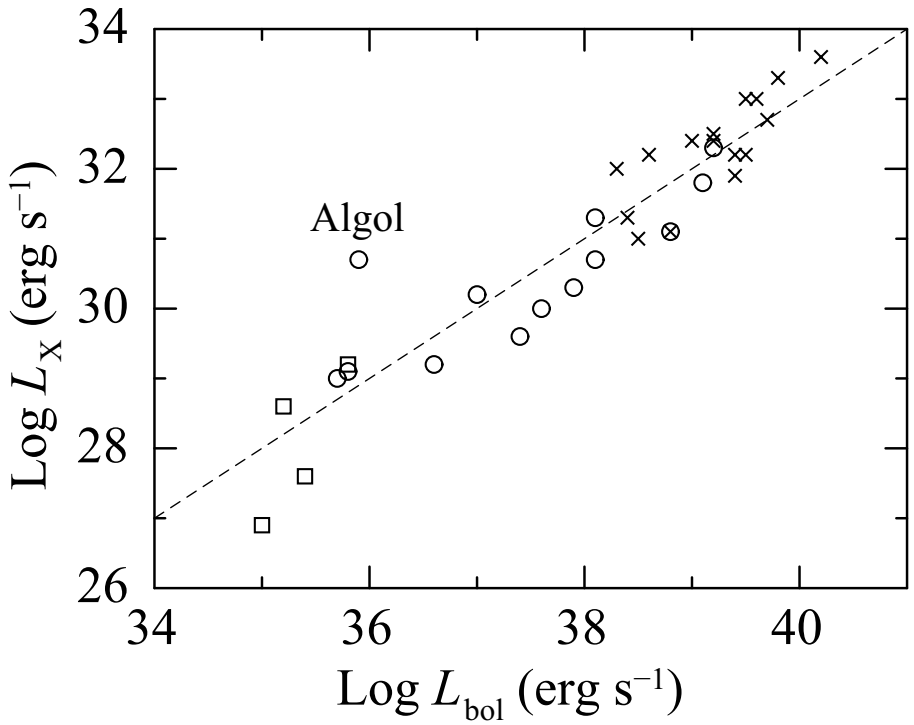

Figure 2.9: Bolometric luminosity and X-ray luminosity in the 0.2–4.0 keV band of early-type stars. Crosses, circles, and squares are for O stars, B stars, and A stars, respectively. The dashed straight line corresponds to the relationship $L_{\rm X} = 10^{-7} L_{\rm bol}$. The only deviated star is the peculiar binary β Per (Algol). Data are taken from Pallavicini et al. (1981).

Lucy & White (1980) and Lucy (1982) proposed a theoretical model for the structure of unstable line-driven winds in early-type stars. In their model, supersonic motion relative to the mean outflow is developed due to hydrodynamic instability. Feldmeier (1995) presented time-dependent numerical simulations for the O supergiant star ζ Pup ($T_{\rm eff} = 4.2 \times 10^4$ K, $R_* = 19\ R_\odot$, $M = 42\ M_\odot$, $v_\infty = 2 \times 10^3$ km s^{-1}, and $\dot{M} = 3 \times 10^{-6}\ M_\odot$ yr^{-1}). They assumed

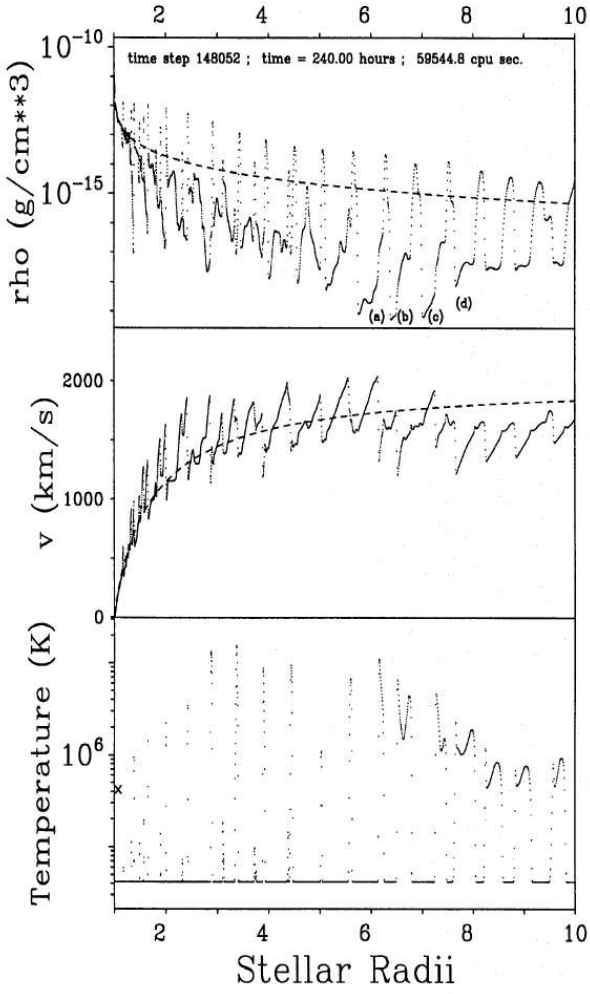

Figure 2.10: Structure of stellar wind where sound-wave instability produces many small-scale shock waves (Feldmeier, 1995). Top, middle, and bottom panels show the gas density, wind velocity, and temperature respectively. Dotted lines show the initial conditions.

1-dimensinal symmetry and gave perturbation with 1% amplitude and a period of 5000 s. Figure 2.10 shows a snapshot of the wind structure 10 days after the perturbation is given. A sequence of very narrow and dense shells with a temperature of $\sim 10^6$ K are formed by hydrodynamical instability.

The ASCA satellite detected hard X-rays from massive stars for the first time (Yamauchi et al., 1996; Tsuboi et al., 1997). The temperatures exceed ~ 3 keV and some sources show flux-variability, which cannot be explained by the wind-instability model described above. Head-on collision between two fast winds can yield a postshock temperature simply because the relative velocity is the sum of two winds' velocities.

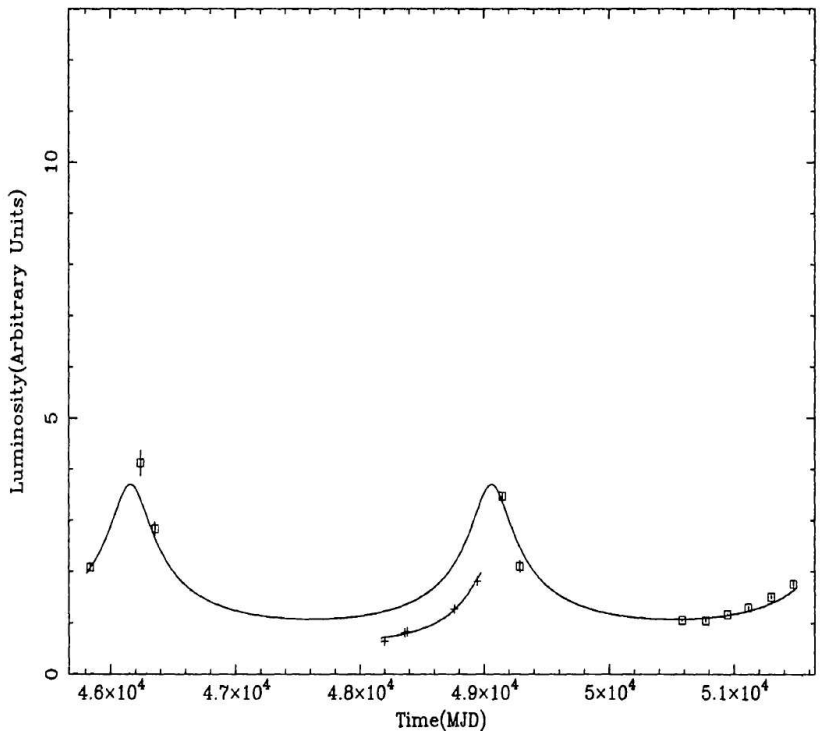

Figure 2.11: Luminosity history of WR 140 (Pollock et al., 2002). Data from EXOSAT (1–10 keV), ROSAT (0.3–2.0 keV), and ASCA (1-10 keV) are shown with squares, pluses, and triangles, respectively. The sold line shows the best-fit X-ray orbit of $e = 0.55$. The lightcurves of soft and hard bands were seperately fitted.

One example of the wind-wind collision is a binary composed of two massive stars. Stevens et al. (1992) presented a 2-dimensional hydrodynamical simulation of colliding winds of binary of two massive stars. If we assume that the stellar winds have reached the terminal velocity even at the periastron, the electron density ($n_{\rm e}$) and the volume (V) of the plasma scale as $n_{\rm e} \propto D^{-2}$ and $V \propto D^3$, where D is the binary separation. Recalling that the two winds collide at their terminal velocities, the plasma temperature does not depend on D. We thus find the luminosity scale as $L_{\rm X} \propto {n_{\rm e}}^2 V \propto D^{-1}$. From a Kepler's law of motion, $D \propto 1/(1 + e\cos\phi)$, hence $L_{\rm X} \propto 1 + e\cos\phi$. The prototype is WR 140 comprised of a WC 7 and a O4–5 V star. The X-ray emission is hard (Koyama et al., 1994) and shows a year-scale flux-variability. Pollock et al. (2002) reported the X-ray light curve spanning ~ 15 years (figure 2.11). Although the luminosity is well correlated with the orbital phase, the best-fit eccentricity of 0.55 is significantly lower than that derived by optical observations ($e = 0.88$; Marchenko et al. 2003).

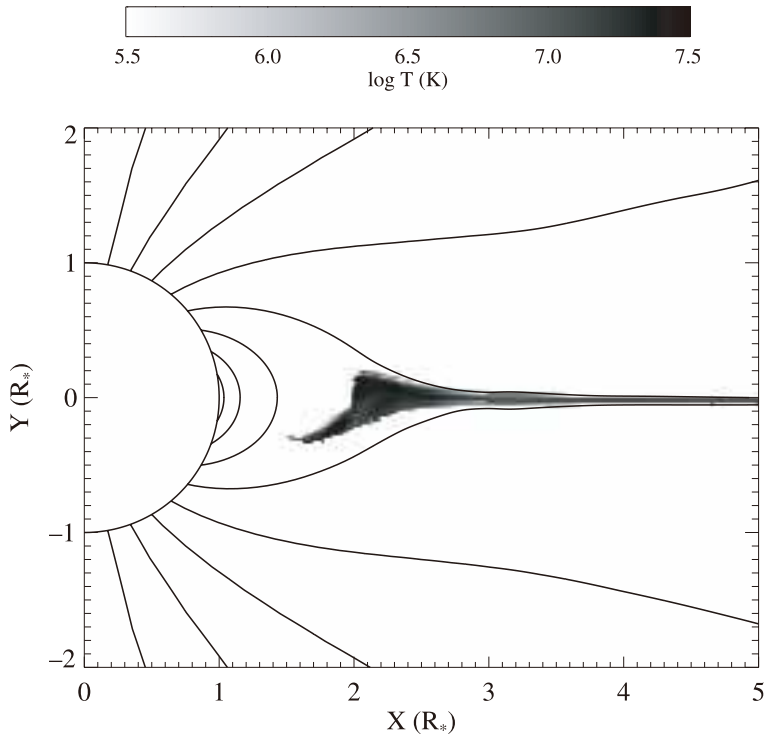

Figure 2.12: Temperature map of θ^1 Ori C obtained by two-dimensional hydrodynamical simulation (Gagné et al., 2005).

Another mechanism is magnetically channeled wind shock (MCWS). Stellar winds in large-scale dipole magnetic field are channeled along the magnetic field line and meet at the equator. This picture was first proposed for magnetic Ap/Bp stars (Shore & Brown, 1990; Babel & Montmerle, 1997), but can also be applied to O stars. The O5.5 V star θ^1 Orionis C is the only O star with measured magnetic field strength. This object is the primary ionizing source of M 42, and shows hard X-ray emission modulated with the spin period of 15.4 days (Stahl et al., 1993; Gagné et al., 1997). Donati et al. (2002) conducted spectropolarimetric observations of θ^1 Orionis C. Their model indicates that the dipole magnetic field has an intensity of ~ 1 kG and a tilt of $42^\circ \pm 6^\circ$ with respect to the rotation axis. Gagné et al. (2005) showed analyzed the phase-resolved Chandra/HETG spectra. They also performed 2-dimensional MHD simulation (figure 2.12) and showed that the observed spectra were well reproduced by MCWS produced at a distance two times the stellar radius.

Chapter 3

Instruments

In this chapter, we review the Suzaku satellite and the onboard instruments. The first subsection describes the overview of the spacecraft. In the following subsections, we show the principles of the telescope and the detectors. Then, the actual performance in the orbit and the calibration accuracy are shown.

Contents

3.1 Overview of Suzaku

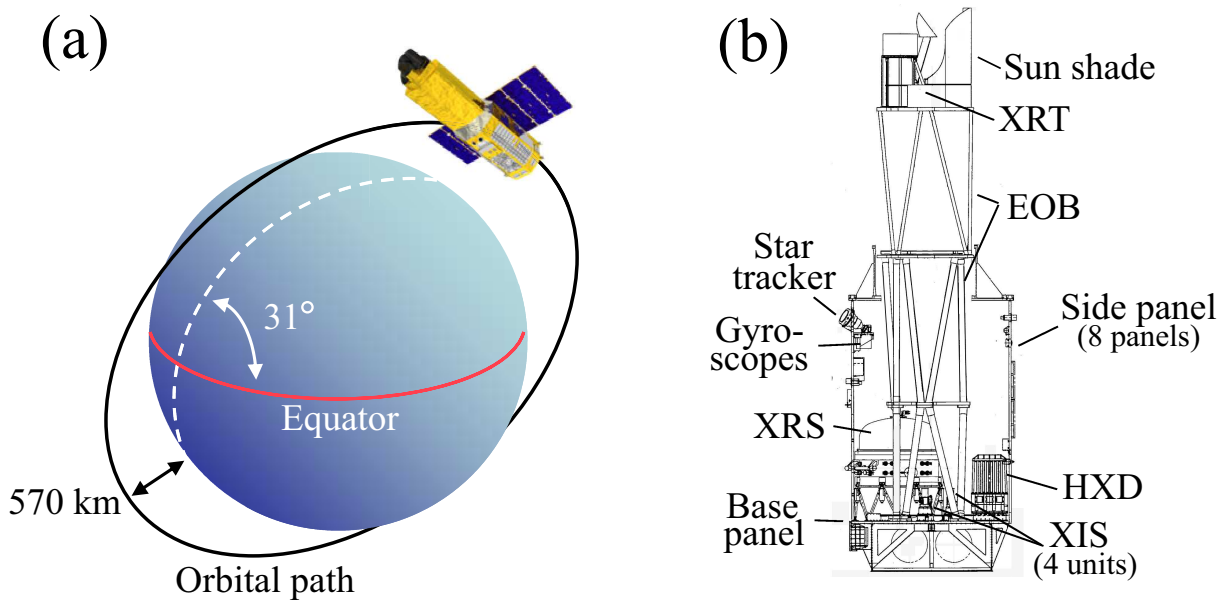

Figure 3.1: (a) Schematic view of the Suzaku satellite in orbit (Mitsuda et al., 2007). (b) Schematic cross-section of Suzaku with the internal structure after the EOB extension (Mitsuda et al., 2007).

Suzaku (Mitsuda et al., 2007) is the fifth Japanese X-ray astronomy satellite developed under a Japan–US collaboration. It was launched by a Japanese M-V 6 rocket from the Uchinoura Space Center (USC) on July 10, 2005, and was successfully put into a near circular orbit at a ~ 570 km altitude with an inclination angle of $\sim 31°$. The orbital period is ~ 96 minutes. Figure 3.1(a) shows a schematic view of Suzaku in orbit. The spacecraft length is 6.5 m along the telescope axis after extending the extensible optical bench (EOB) and the total weight is ~ 1700 kg.

The solar panel, providing the total electric power of ~ 660 W, is fixed on the satellite. This constrains the pointing direction to be $65° - 110°$ from the Sun for the battery charge. With this constraint, almost all targets are occulted by the earth for a certain fraction of every 96 minutes. Only objects near the orbital pole can be observed nearly continuously. The averaged observing efficiency is $\sim 45\%$

Suzaku carries three co-aligned scientific detector systems: the Hard X-ray Detector (HXD: Takahashi et al. 2007; Kokubun et al. 2007), the X-ray Imaging Spectrometer (XIS: Koyama et al. 2007a), and the X-ray Spectrometer (XRS: Kelley et al. 2007). Figure 3.2 shows the configuration of the detectors on the base panel. The XRS and four XIS cam-

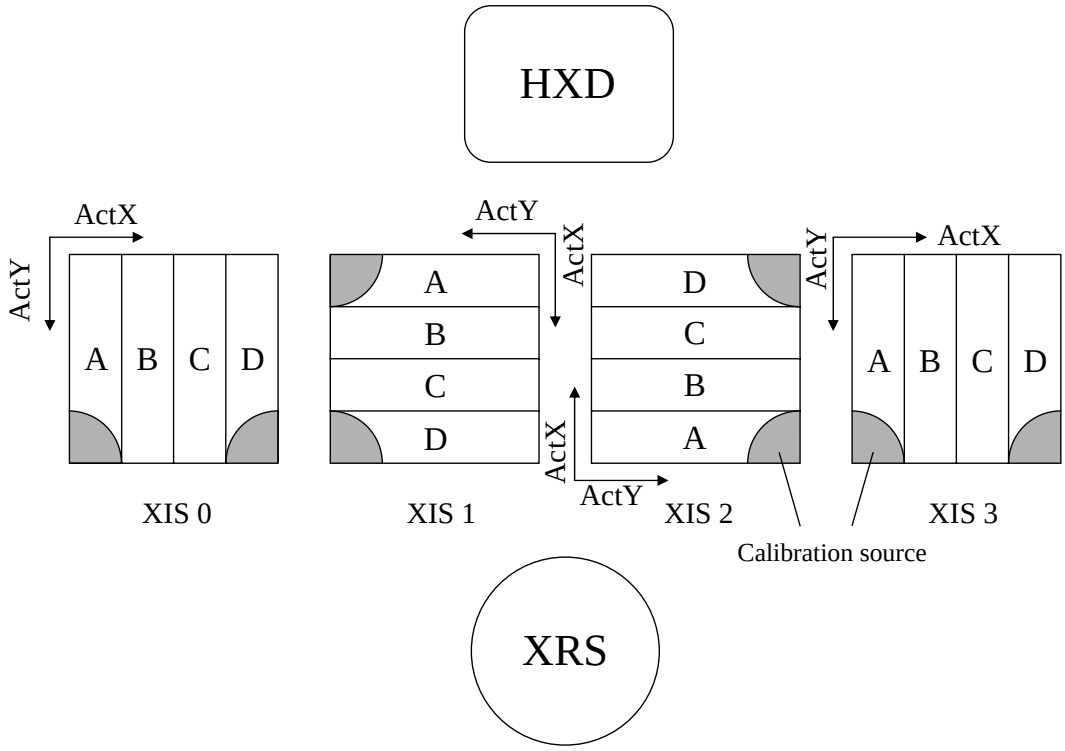

Figure 3.2: Configuration of the detectors in the Suzaku satellite. (the Suzaku technical description). The definition of the XIS coordinates is also shown.

eras are located at the focal plane of the corresponding X-ray Telescope modules (XRT: Serlemitsos et al. 2007). We will not discuss the XRS further, which became unoperational due to the evaporation of the liquid helium coolant a few weeks after the launch. The configuration of the detectors are shown in figure 3.2.

3.2 XRT

3.2.1 Overview of the XRT

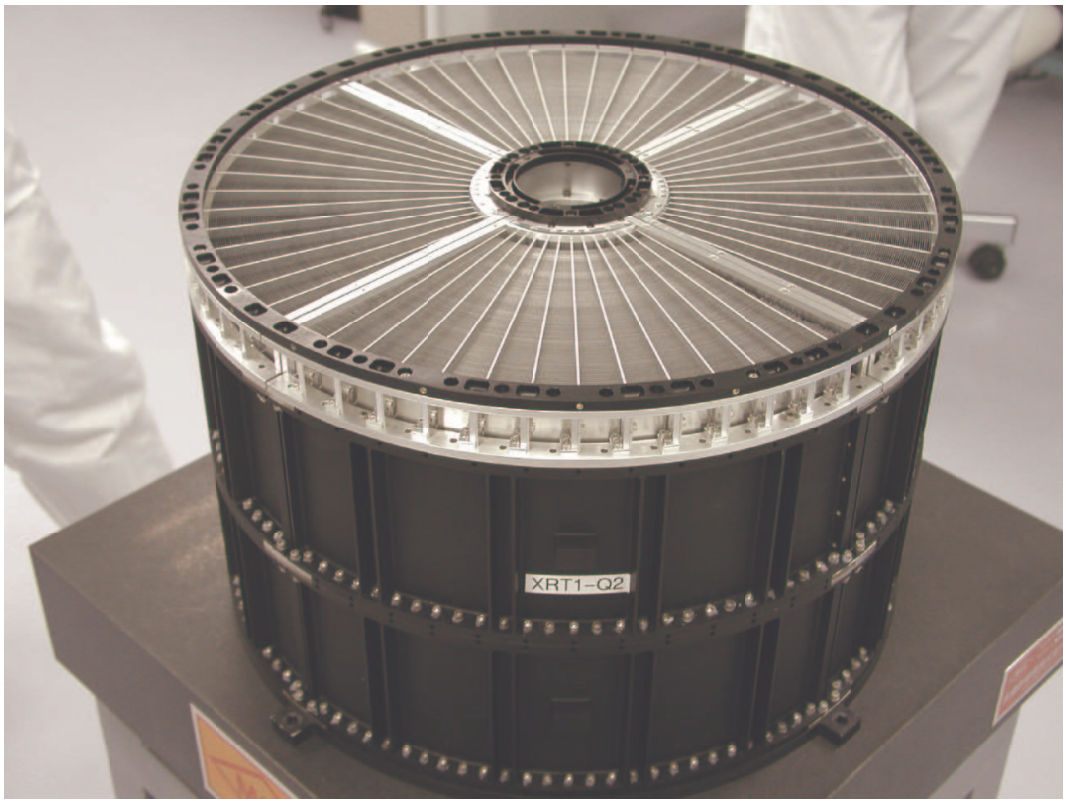

Figure 3.3: Picture of the XRT-I1 module (Serlemitsos et al., 2007).

Five XRT modules are installed on the top plate of the EOB. One is designated as XRT-S, dedicated for the XRS. The other four modules are adapted for each XIS camera and referred to as XRT-I0, I1, I2, and I3 (figure 3.3).

X-rays are reflected by smooth surfaces of high-electron-density material at very shallow angles of $\leq 1^\circ$ (grazing incidence). Since the reflection is non-dispersive, circular X-ray mirrors for grazing incidence can focus X-rays over a broad energy band. In this configuration, only a fraction of the geometric area of the telescope can be used to collect X-ray photons for imaging, so multiple layers are combined to increase the effective area.

In Wolter type-I reflective optics, X-rays are reflected twice by a parabolic surface and a hyperbolic surface sequentially (figure 3.4). The precise Wolter design yields a spatial resolution of ~ 1 arcsec, such as the X-ray telescope adopted for the Chandra X-ray Observatory.

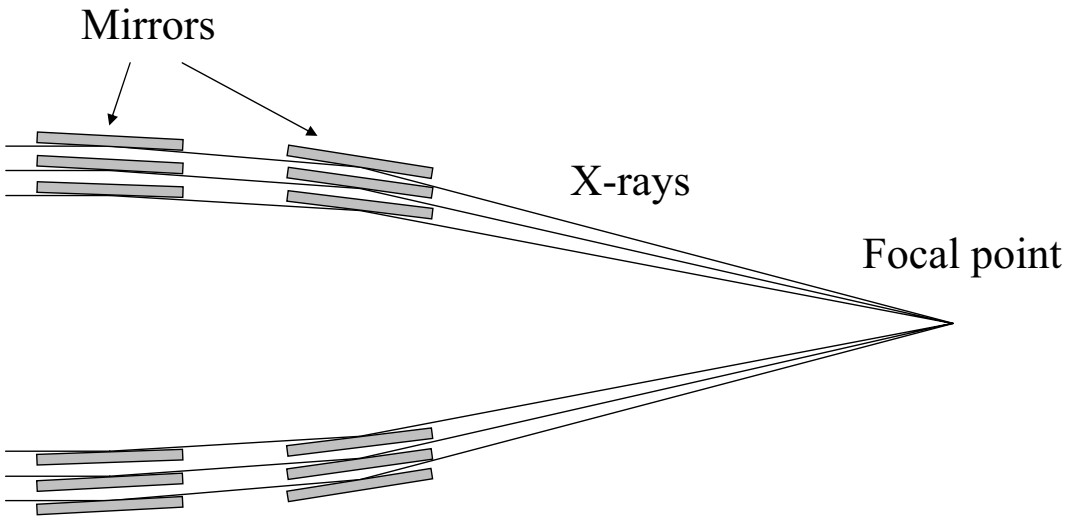

Figure 3.4: Schematic cross-section of Wolter-I type X-ray mirror. Incident X-rays are reflected twice at very shallow angles and concentrated at the focal point.

However, this sacrifices the effective area, as the small surface roughness requires a heavy substrate and limits the number of nesting layers.

Suzaku takes the opposite approach. It increases the effective area with 175 thin foil layers in each XRT-I module at the sacrifice of good spatial resolution. It is difficult to construct a precise Wolter geometry with thin foils with a thickness of ~ 180 μm adopted for XRT, so both the primary and secondary reflectors of XRT are approximated by simple cones, which limits the spatial resolution to about ~ 18 arcsec. Since the electron density strongly depends on the atomic number, the reflector surface is coated with Au with a thickness of ≥ 1000 Å.

Both the primary and secondary reflectors are made of four sections ("quadrants"). Since the spaces between two quadrants are dead areas, point source images appear to be a cross or a butterfly (figure 3.6).

3.2.2 Onborad Performance

The left panel of figure 3.5 shows the energy-dependent on-axis effective area including the detector efficiency. At larger off-axis angles, incident X-rays are partially obscured by neighboring reflectors. This vignetting effect is prominent at high energy because high energy photons have smaller critical angles and are efficiently reflected at innermost mirrors, where the cone angles is small and the reflectors are tightly packed, thus highly subject to

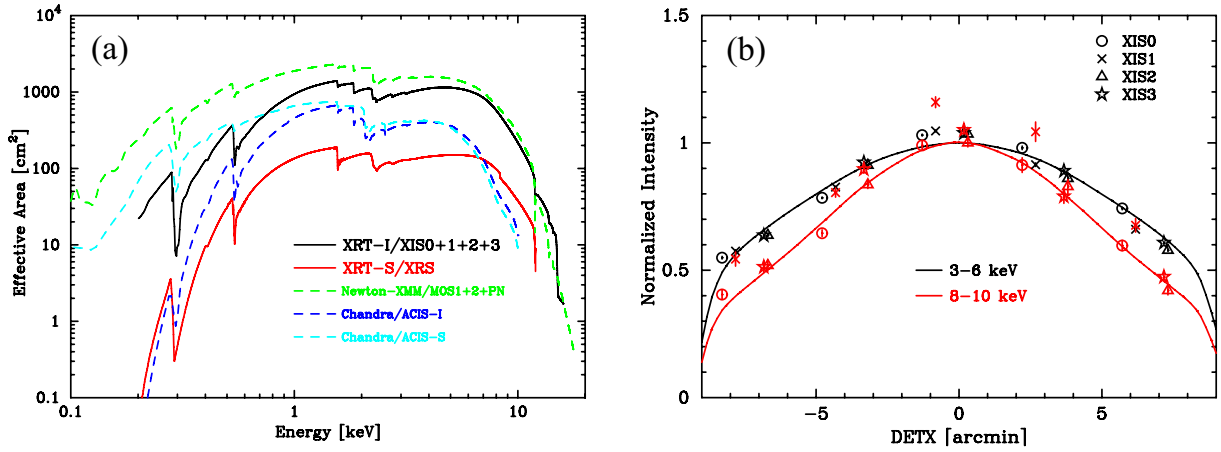

Figure 3.5: (a) Total effective area of the XRT combined with the XIS (Serlemitsos et al., 2007). Those of other X-ray missions are also shown for comparison. (b) Off-axis angle dependence of the effective normalized at the optical axes in the soft and hard bands shown with black and red points respectively (Serlemitsos et al., 2007). Data are obtained with the Crab nebula observations. The solid lines show the simulated model.

shadowing. Figure 3.5 (b) shows the vignetting curve in the soft (3–6 keV) and hard (8–10 keV) bands. Since the effective area is defined by the number of source photons within the CCD field of view (FOV) of a $17'.8 \times 17'.8$ square, the model curves show sharp drops at $\sim 8'$.

The angular resolution was verified with the SS Cyg data in quiescence (figure 3.6). Figure 3.7 shows the point spread function (PSF) and the encircled energy function, which are typical indicators of spatial resolution. Since the primary factor of the XRT spatial resolution is the misalignment of the nested reflectors, the PSF is nearly energy-independent.

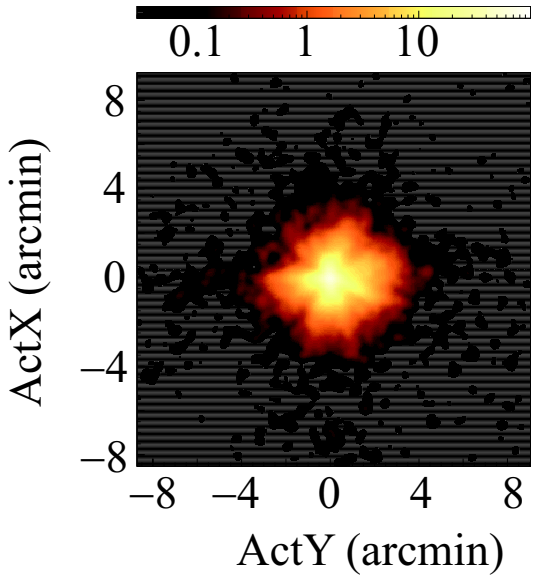

Figure 3.6: Image of SS Cyg at the optical axis taken with XRT-I2 (Serlemitsos et al., 2007). The color scale shows the X-ray counts pixel^{-1}

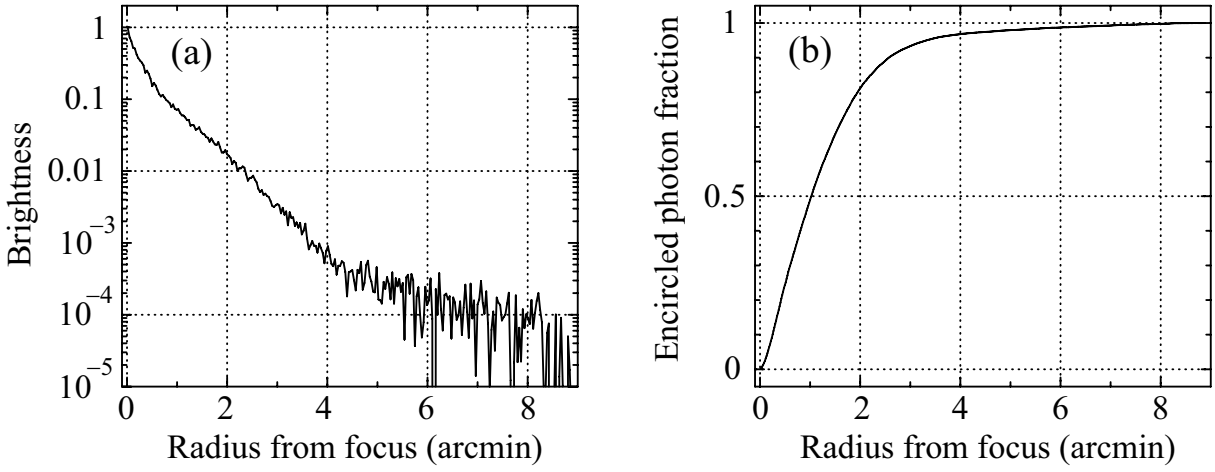

Figure 3.7: Point spread function (PSF, left panel) and the encircle energy fraction (EEF, right panel) of the XRT (for XIS2) at the focal plane (Serlemitsos et al., 2007).

3.3 XIS

3.3.1 Overview of the XIS

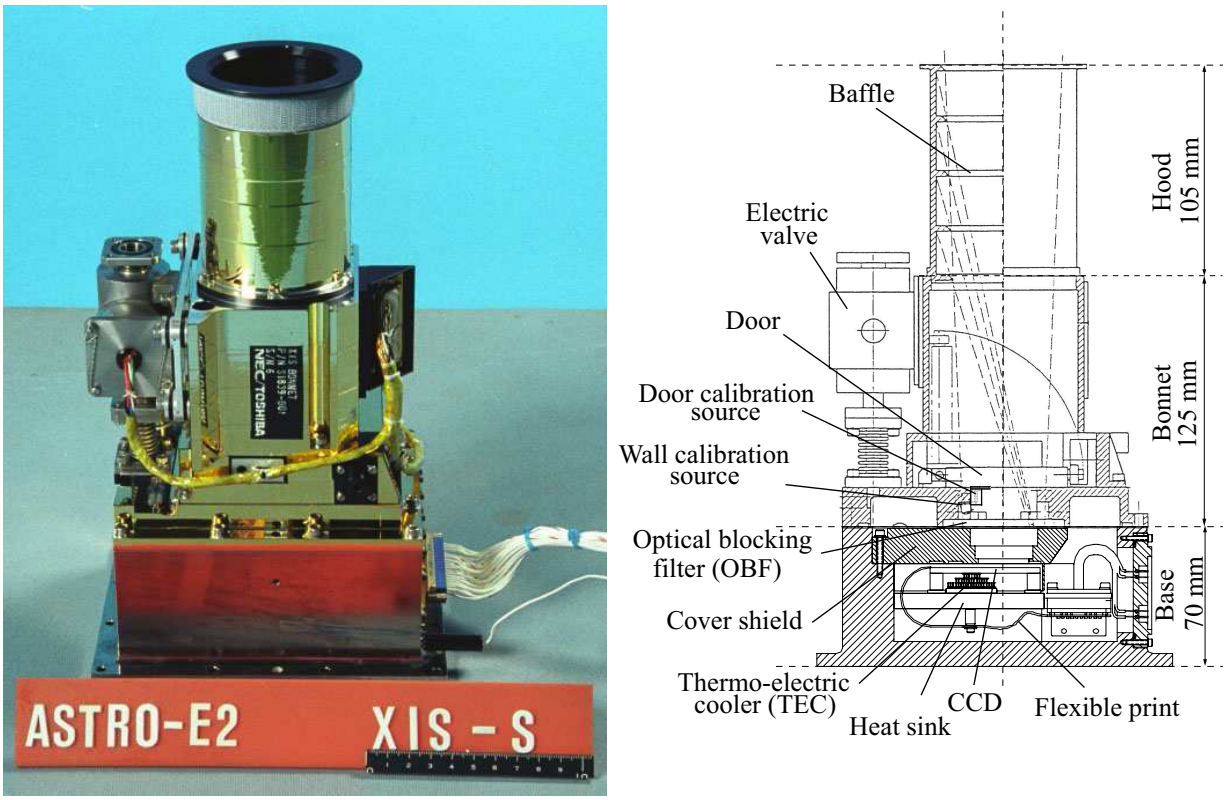

Figure 3.8: Left panel: Picture of one of the XIS sensors. Right panel: Cross section of the XIS sensor (Koyama et al., 2007a).

The XIS is comprised of four X-ray charge coupled device (CCD) camera systems (figure 3.8). X-ray CCD converts an incident X-ray photon to a cloud of electrons, the amount of which is proportional to the energy of the absorbed X-ray photon. The cloud made in the depletion layer in each pixel is transferred to the gate of the output transistor by three-phase electric potential clocking. In MOS-type CCDs (figure 3.9), the gate is made of poli-Si (Metal), the insulator is made of SiO_2 (Oxide), and the depletion layer is made of Si (Semiconductor). In the frame transfer mode, the charges are transferred from the imaging area (IA) to the frame store (FS) region after an exposure. Then, the charges in the FS region is transferred vertically along the ActY direction and horizontally along the ActX direction sequentially.

One side of a CCD is coated with the gate structure mainly made of Si and SiO_2 (front

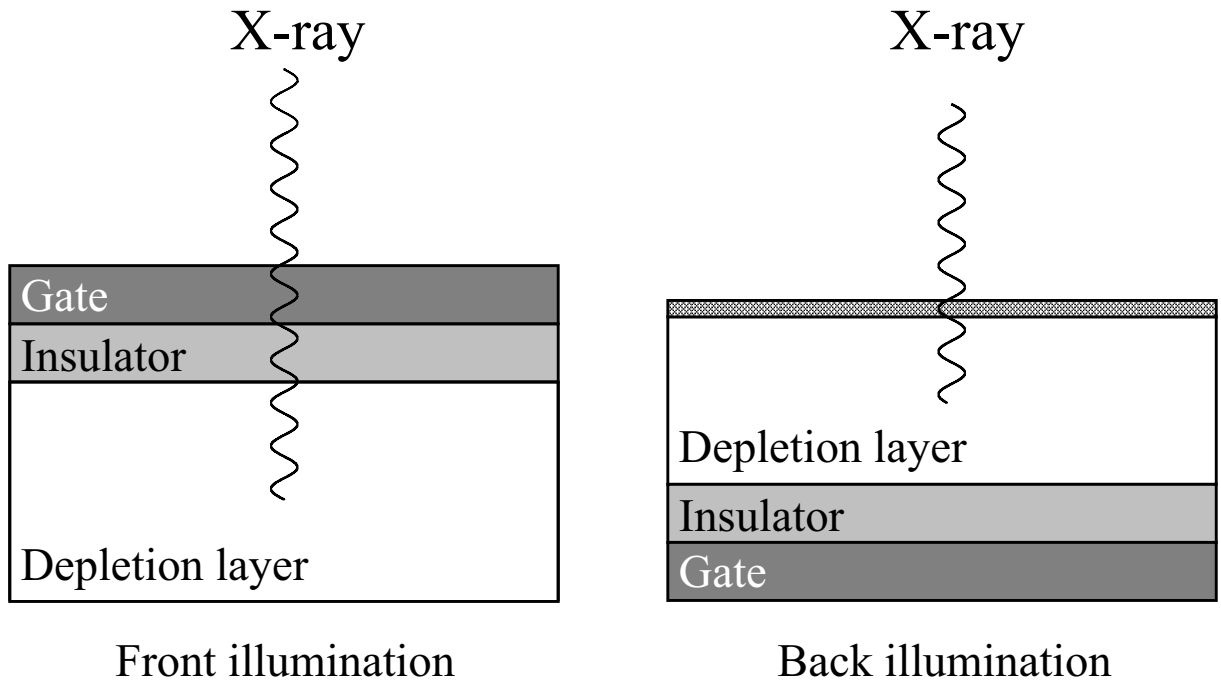

Figure 3.9: Difference of front illumination and back illumination in MOS-type CCD.

side). Front-illuminated (FI) CCDs detect X-rays that penetrate the gate structure with a thickness of ~ 0.7 μm, whereas the surface dead layer of back-illuminated (BI) CCDs have a thickness of ~ 10 nm (figure 3.9). Due to the absence of the gate structure, BI CCDs achieve a high quantum efficiency (QE) even below ~ 1 keV. On the other hand, FI CCDs employ thicker depletion layer than BI CCDs (~ 76 μm for FI CCDs and ~ 42 μm for BI CCD), and have higher QE for high energy photons.

In both the IA and FS regions, the CCD chips have a format of 1024×1024 pixels and four read-out nodes. Thus, a CCD chip is composed of four segments of 256×1024 pixels (figure 3.10). The pixel size of the IA is 24 μm$\times$24 μm. Combined with XRT, each pixel corresponds to $1.04'' \times 1.04''$ of the sky, and the field of view is $18' \times 18'$. Three of the chips (XIS 0, XIS 2, and XIS 3) are FI CCDs, and the remaining one (XIS 1) is a BI CCD. The QE of the FI CCDs is better than that of BI CCD above ~ 4 keV (figure 3.11). The detector is operated at a temperature of ~ -90°C controlled by Pertier coolers.

Each XIS has an optical blocking filter (OBF) to block optical and UV photons. The OBF is made of ~ 1400 Å polyimide ($C_{22}H_{10}N_2O_4$) coated with Al of a ~ 1200Å thickness.

For on-orbit calibration of the energy scale, each device is equipped with two radioactive sources (^{55}Fe). ^{55}Fe decays to leave ^{55}Mn via electron capture mainly (88.5%) from

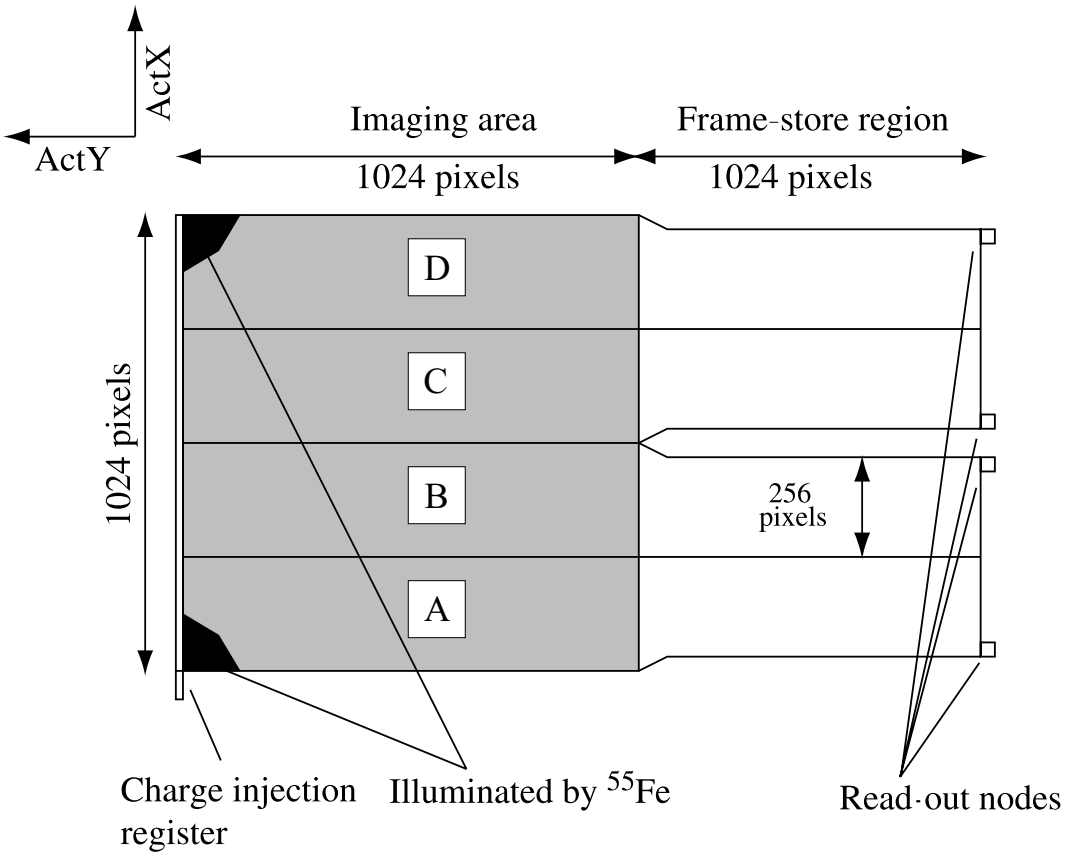

Figure 3.10: Schematic view of the XIS CCD (Koyama et al., 2007a).

the K-shell. Subsequently, fluorescent X-ray is emitted, accompanied by an L→K electron transition (Kα: 5.895 keV) or an M→K electron transition (Kβ: 6.513 keV). These sources illuminate two far corners from the read-out nodes. A small fraction of the X-rays from the calibration sources is scattered onto the entire CCD.

3.3.2 Onboard Performance

The charge transfer inefficiency (CTI) has been increasing since the launch due to charge traps caused by radiation damage (Nakajima et al., 2008; Ozawa et al., 2009). Consequently, the energy resolution has been degrading, which was initially of ~ 130 eV at 5.9 keV in full width at half maximum. (figure 3.12). To mitigate the degradation, spaced-row charge injection (SCI) technique is applied for almost all observations since October 2006. In the SCI technique, electrons are injected from the furthest side from the read-out nodes to fill the traps as "sacrificial charges". This prevents charges generated by X-rays from being

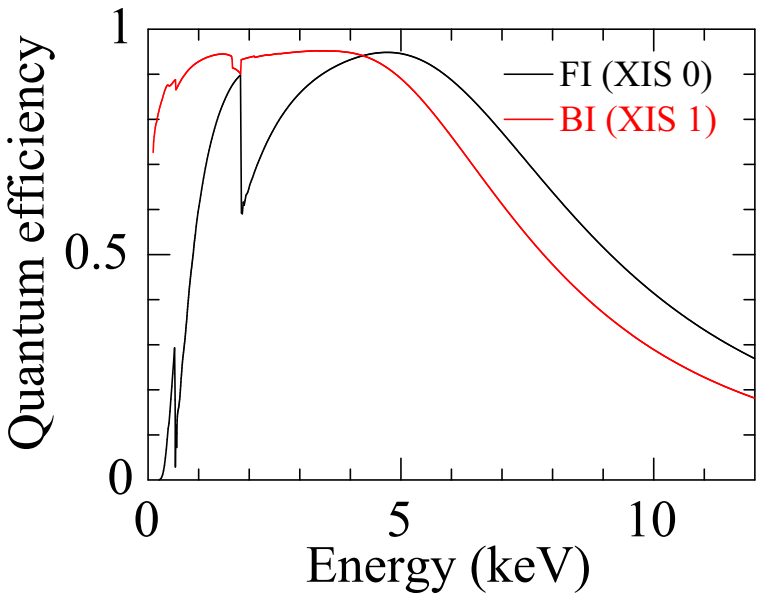

Figure 3.11: Quntum efficiency of the XIS as a function of incident photon energy. The black and red curves are for XIS 0 and XIS 1 respectively (Koyama et al., 2007a). The effect of contaminant on the OBF is not included.

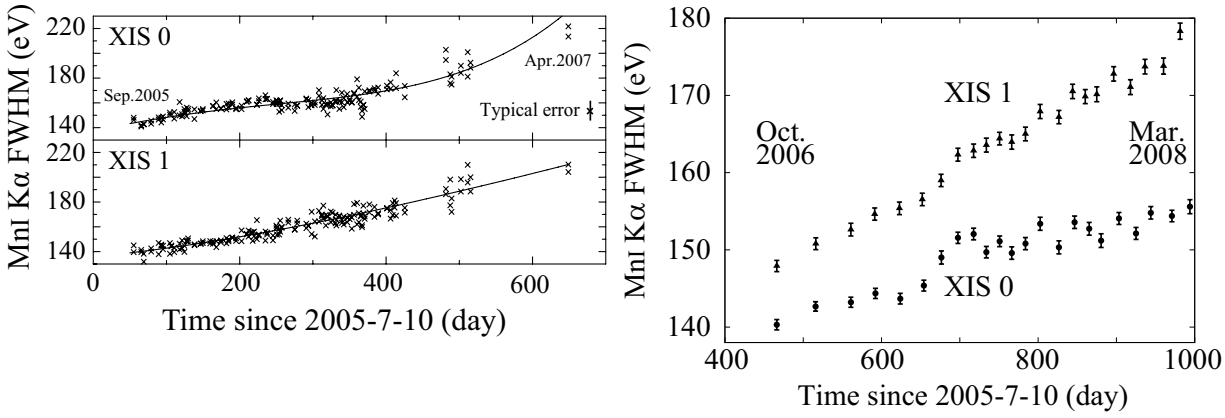

Figure 3.12: Long-term trend of energy resolution (Ozawa et al., 2009; Uchiyama et al., 2009).

captured by the traps and actively reduces the CTI. A new calibration method dedicated for SCI observations has been established (Uchiyama et al., 2009). With this method, the energy resolution still retains ~ 155 eV and ~ 175 eV at 5.9 keV for FI and BI CCDs respectively as of March 2008 (figure 3.12).

The low energy QE has degraded by unexpected contamination (due to out-gassing

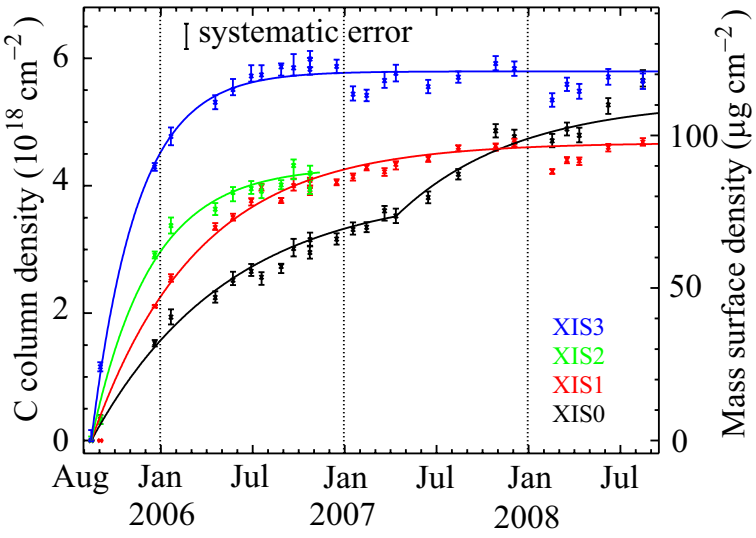

Figure 3.13: Long-term trend of on-axis contaminant represented by carbon column density (The Suzaku technical description). An empirical model is shown in solid lines.

from the satellite) accumulating on the OBF (Koyama et al., 2007a). The contaminant is mainly composed of carbon and oxygen. The time evolution of the contamination has been measured using regular observations of 1E 0102–072 (figure 3.13). Although the chemical composition of the contaminant is still uncertain, it is assumed to be C/O=6 in number. The effect of contamination is included in ancillary response files made by `xissimarfgen` (Ishisaki et al., 2007).

Figure 3.14 shows the non–X-ray background (NXB) accumulated during night-earth observations. The data obtained during the South Atlantic anomaly passages and in the calibration source areas are excluded. The flux of NXB depends on the geo-magnetic cut-off rigidity (COR, figure 3.14) and the position of CCDs. The COR distribution was recently updated and is called COR2. We hereafter use COR2. Tawa et al. (2008) modeled the NXB spectra as a function of COR2. The NXB can be constructed for any observations with an accuracy of $\sim 5\%$.

On November 9, 2006, XIS 2 suddenly showed an anomaly. About 2/3 of the image was unusable due to a large amount of charge leakage. This event was possibly caused by a micro-meteoroid impact, as seen in XMM-Newton and Swift. Since this anomaly, XIS 2 has been dysfunctional. Figure 3.15 shows the time of XIS 2 anomaly and start of SCI observations. The observations presented in this thesis are also shown sequentially.

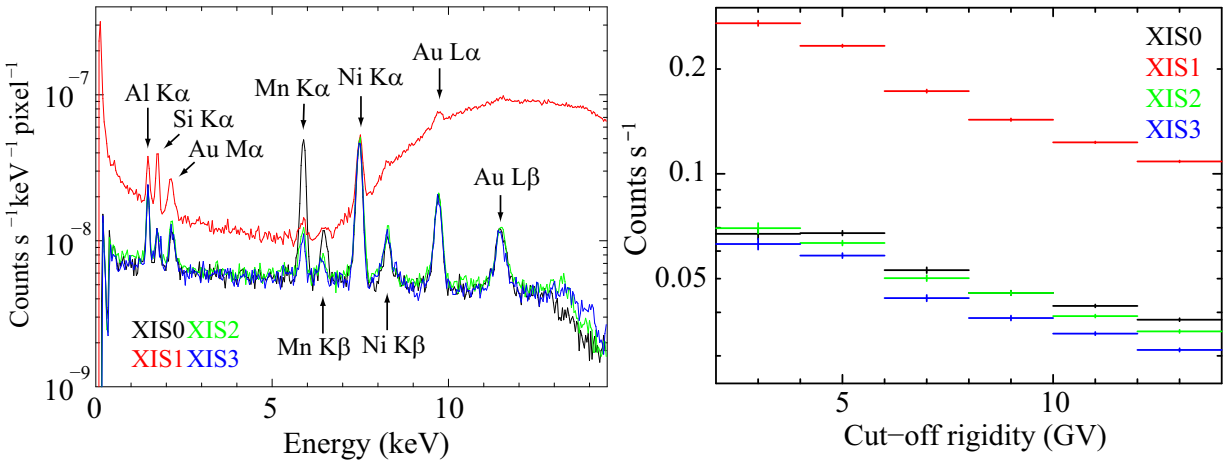

Figure 3.14: XIS spectra obtained during night earth observations.

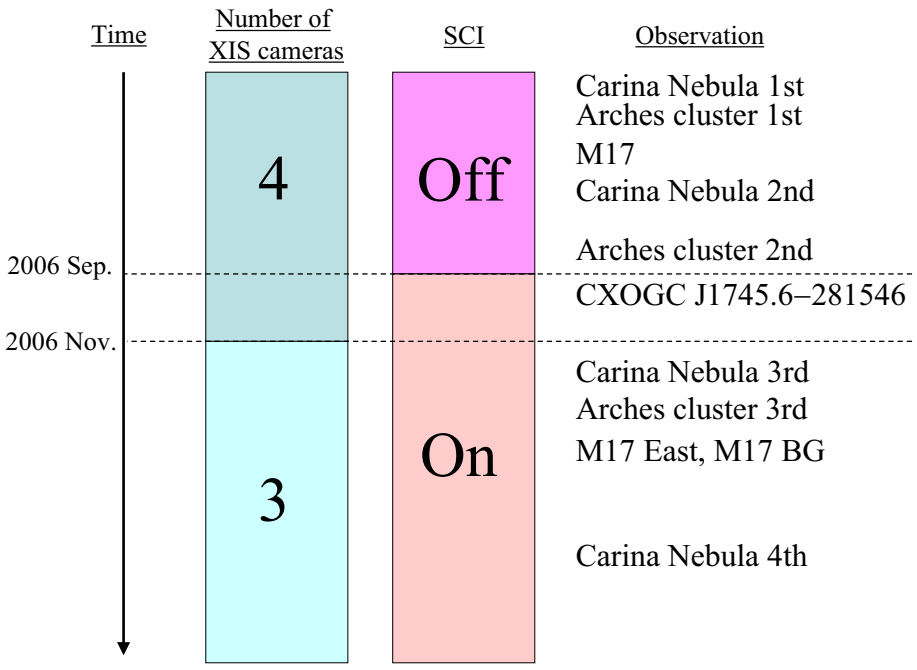

Figure 3.15: History of the observing condition of the XIS.

3.4 HXD

3.4.1 Overview of the HXD

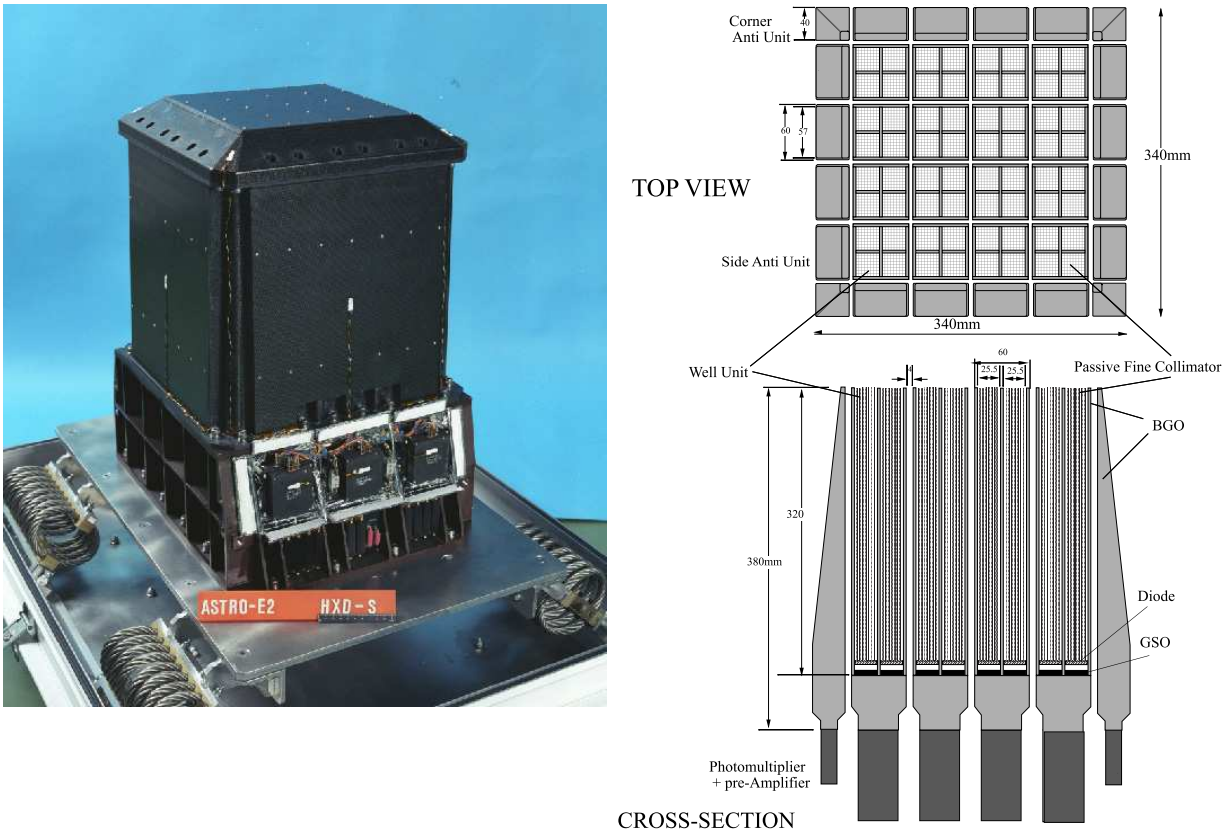

Figure 3.16: Picture of the HXD (Kokubun et al., 2007).

The HXD (figure 3.16) is a non-imaging collimated detector. It has a compound eye configuration to increase the effective area. The sensor consists of 16 well-counter units and 20 surrounding bismuth germanate crystal (BGO) anti-coincidence counters (figure 3.16).

Each well-counter unit is comprised of four (2×2) Si PIN diodes, which are located in front of a GSO scintillator. The PIN is sensitive in 10–60 keV, and gradually becomes transparent to higher energy photons. The GSO detects photons that pass through the PIN and is sensitive in 40–600 keV (figure 3.17). A coarse collimator and an active shield is made of BGO scintillators. A BGO scintillator is placed also below the GSO scintillators. The aspect ratio of the coarse collimators restricts the FOV of the GSO to be $4.^{\circ}5$ in FWHM. The PIN has extra "fine collimators" made of bronze and achieves a narrower FOV of $34' \times 34'$.

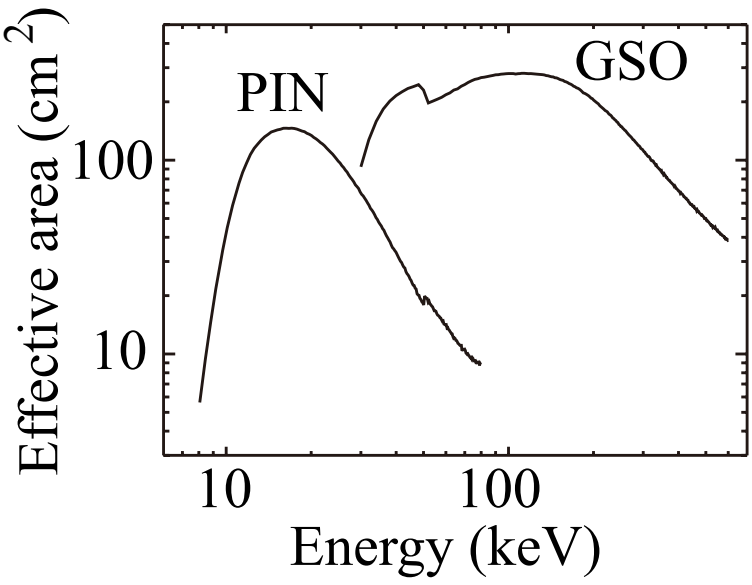

Figure 3.17: Effective areas of PIN and GSO (Takahashi et al., 2007)

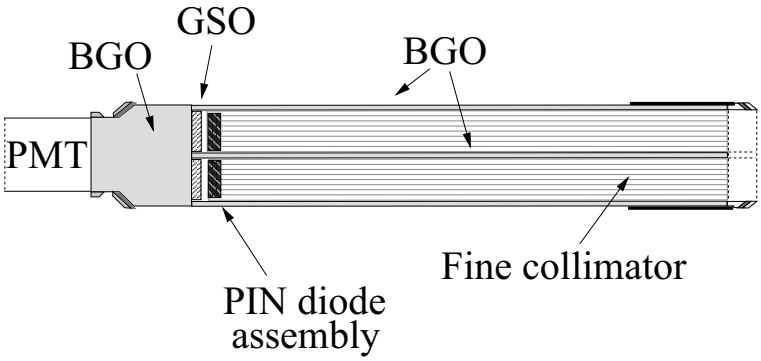

Figure 3.18: Schematic view of a well-counter unit (Takahashi et al., 2007).

All scitillator signals in one unit is read out from one photomultiplier tube (PMT). Since the BGO and GSO have different rise/decay times ($\sim$ 700 ns for BGO and $\sim$ 120 ns for GSO at a working temperature of -20°C), a single PMT can discriminate signals in the two types of scintillators.

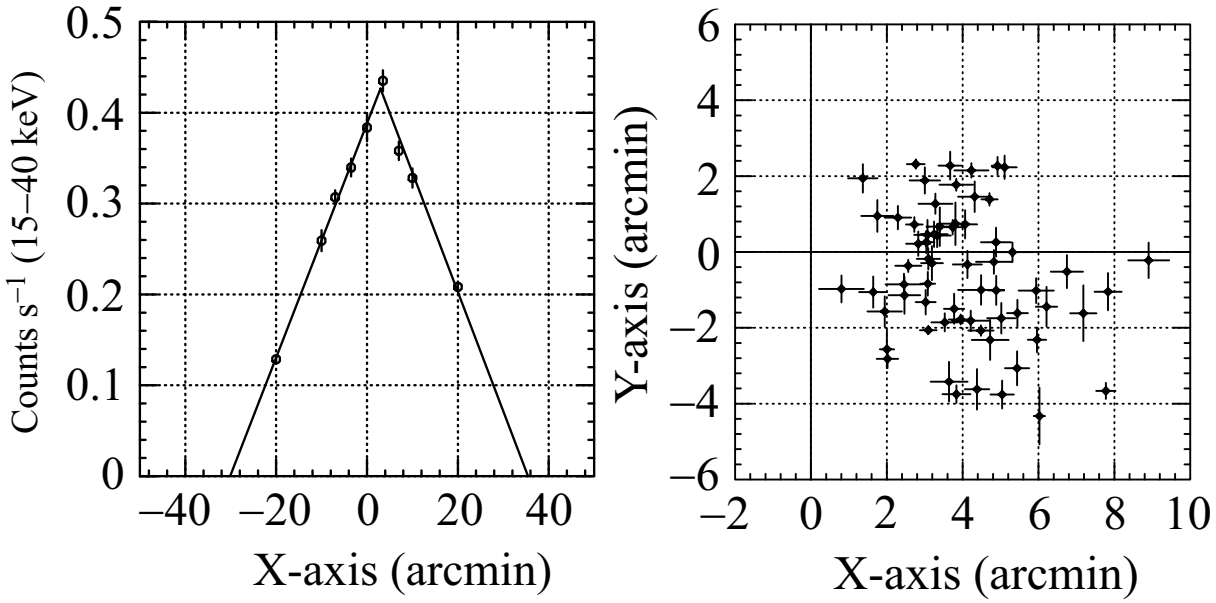

Figure 3.19: Angular response of PIN (Kokubun et al., 2007).

3.4.2 Onboard Performance

The angular response of PIN was measured using multiple pointing observations of the Crab Nebula. The observations were performed with offset angles of 0, $\pm 3'.5$, $\pm 7'$, $\pm 10'$, $\pm 20'$ in both the X and Y directions of the satellite. Background-subtracted spectra were constructed for all of the 64 PIN diodes individually. The resultant count rates in 15–40 keV are shown in figure 3.19. The fluxes are plotted against X- and Y- axes and the peak point was searched by fitting with a triangular function. Figure 3.19 shows the optical axes of 64 PIN diodes. Since the weighted mean is slightly shifted by $\sim 4'$ from the XIS optical axis, the effective area of PIN decreases by $\sim 10\%$ for the sources at the XIS-nominal position.

The NXB of the HXD depends on COR like that of the XIS. Figure 3.20 shows the NXB spectra with three COR regions, together with their ratios. The NXB increases at lower COR, and this trend is more significant at higher ($\geq$ 25 keV) energy band. The reproducibility of the latest NXB model (`bgd_d`) is 1.3% in 1σ.

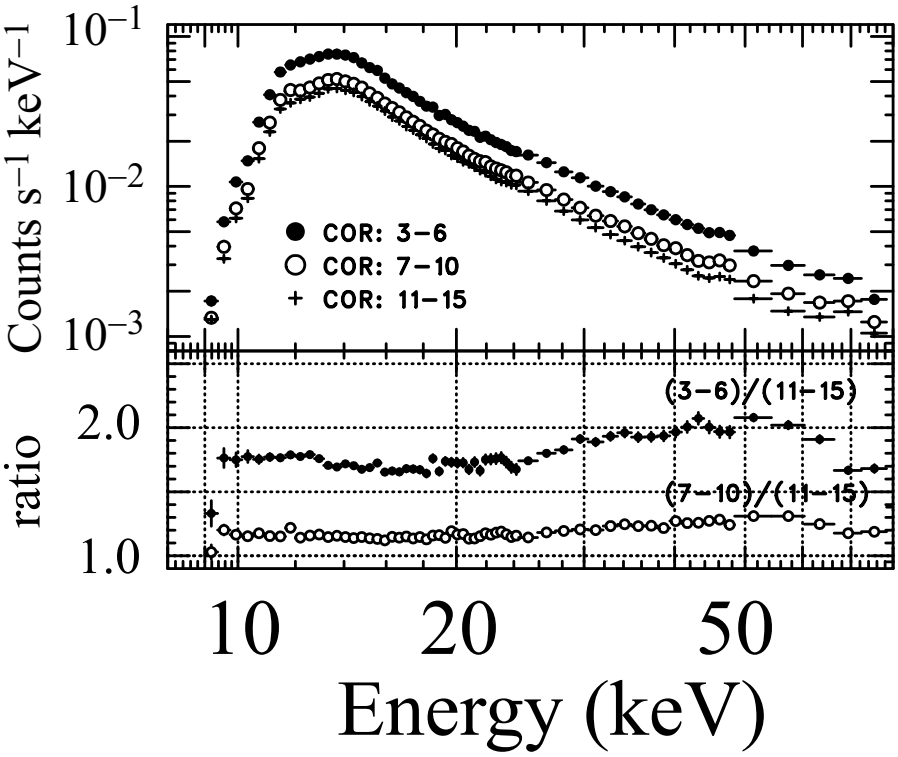

Figure 3.20: NXB spectra of the PIN sorted with COR (Kokubun et al., 2007). Events are extracted from the Earth occultation data.

Chapter 4

Observations & Results

In this chapter, we describe the Suzaku observations on four fields containing massive stars and massive star clusters. In section 3.1, we identify a new source serendipitously discovered during the Galactic center survey conducted with Suzaku. In sections 3.2 and 3.3, we present the analysis of two famous star forming regions, the Carina Nebula and M 17 (the Omega Nebula). Both regions contain discrete massive stars and diffuse emission. Finally in section 3.4, we show the analysis of the Arches cluster. The cluster also has point sources and diffuse emission, which are not spatially resolved with Suzaku's telescope. The goal of this chapter is to present light curves of all discrete sources and spectra of all discrete sources and diffuse sources.

Contents

4.1 A New Wolf-Rayet Star in the Galactic Center

4.1.1 Objectives

In the Galactic center region, WR stars as well as main-sequence massive stars are concentrated in three clusters near the Galactic center; the Arches (Nagata et al., 1995; Cotera et al., 1996; Serabyn et al., 1998; Figer et al., 1999b), the Quintuplet (Kobayashi et al., 1983; Okuda et al., 1990; Nagata et al., 1990; Figer et al., 1999a), and the Central cluster (Becklin & Neugebauer, 1968; Krabbe et al., 1995; Ghez et al., 2005). However, it is quite natural to expect that a much larger number of early-type stars remain unidentified. Portegies Zwart et al. (2001) claimed that the number of young massive star clusters may exceed 50 in the Galactic center region. The inconsistency with the observed value indicates that these clusters are too obscured to be visible in the optical and infrared bands, or that the cluster members are dissipated before the earliest member reaches its end, or that the predicted number is a gross overestimate. Kim et al. (1999) showed that the strong tidal disruption in the Galactic center region makes massive star clusters become unbound on a very short time scale comparable to the lifetime of an O star. Isolated early-type stars may be distributed throughout the region, unlike the other parts of the Galaxy where they are found in clusters.

Some early attempts have been made to discover unidentified early-type stars in the Galactic center region with the combination of X-ray and infrared (IR) observations. Muno et al. (2006a) made trailblazing observations of radio, IR, and X-ray to reveal the population of young massive stars in the Galactic center region. They detected strong Brγ and He I lines from two sources, and classified them as either Of or candidate LBV stars. Mauerhan et al. (2007) also conducted K-band spectroscopy of six bright hard X-ray sources with very red IR colors. Two of them, with IR colors of J–$K = 4$–5 mag, show broad hydrogen and helium emission lines characteristic of evolved O-type stars. They are classified as a Wolf-Rayet star of a spectral type of WN6 and an O-type Ia supergiant.

Likewise, Mikles et al. (2006) performed infrared spectroscopy of CXO J174536.1–285638, which is one of new Chandra sources discovered by Muno et al. (2003). They detected P Cygni profiles of He II lines of a 170 km s^{-1} wind. The spectral features in the X-ray and IR bands are most consistent with a colliding wind binary system such as η Carinae. This source is of particular interest in terms of a strong Fe XXV emission line, which is also prominent in our source, presented below. We see a high prospect of these methods to find similar sources en masse.

Near-IR spectroscopy may confront a challenge for even redder sources. In addition to a ~ 30 mag visual extinction ubiquitous toward the Galactic center region (Catchpole et

al., 1990; Schultheis et al., 1999), evolved early-type stars are behind an additional local extinction by their own mass loss. Photospheric emission is reprocessed into longer wavelength radiation in the optically thick circumstellar matter. The IR spectra turn out to be featureless by strong veiling (Figer et al., 1999a; Crowther et al., 2006). For such sources, the spectroscopy of the hard X-ray emission directly from the vicinity of the star is the only practical tool. These stars contribute to the 6.7 keV line emission, and the diagnosis of the line emission helps to identify their nature.

Suzaku has made a total of ~ 2 Ms mapping observations toward the central $\sim 1^\circ \times 3^\circ$ of our Galaxy. With the large effective area, this deep survey provides the best opportunity to perform a systematic search for WR stars. Figure 4.1 shows the XIS mosaic image of the Galactic center in the 6.55-6.8 keV. In addition to the diffuse emission prevailing the whole region, we see some local excess, which we identify as the SNR G0.61+0.01 (Koyama et al., 2007b), the pulsar wind nebula G0.9 + 0.1 (Mereghetti et al., 1998; Sidoli et al., 2000; Porquet et al., 2003), the Great Annihilator 1E 1740.7–2942 (Bouchet et al., 1991; Sakano et al., 1999; Gallo & Fender, 2002), the low-mass X-ray binary 1A 1742–294 (Lewin et al., 1976; Pavlinsky et al., 1994; Sidoli et al., 1999), and the Arches cluster. We found a bright, hard, and point-like source at $(l, b) \sim (0.7, 0.1)$, the nature of which is not addressed before. To identify the nature of this source, we perform temporal and spectral analysis.

4.1.2 Observations & Reduction

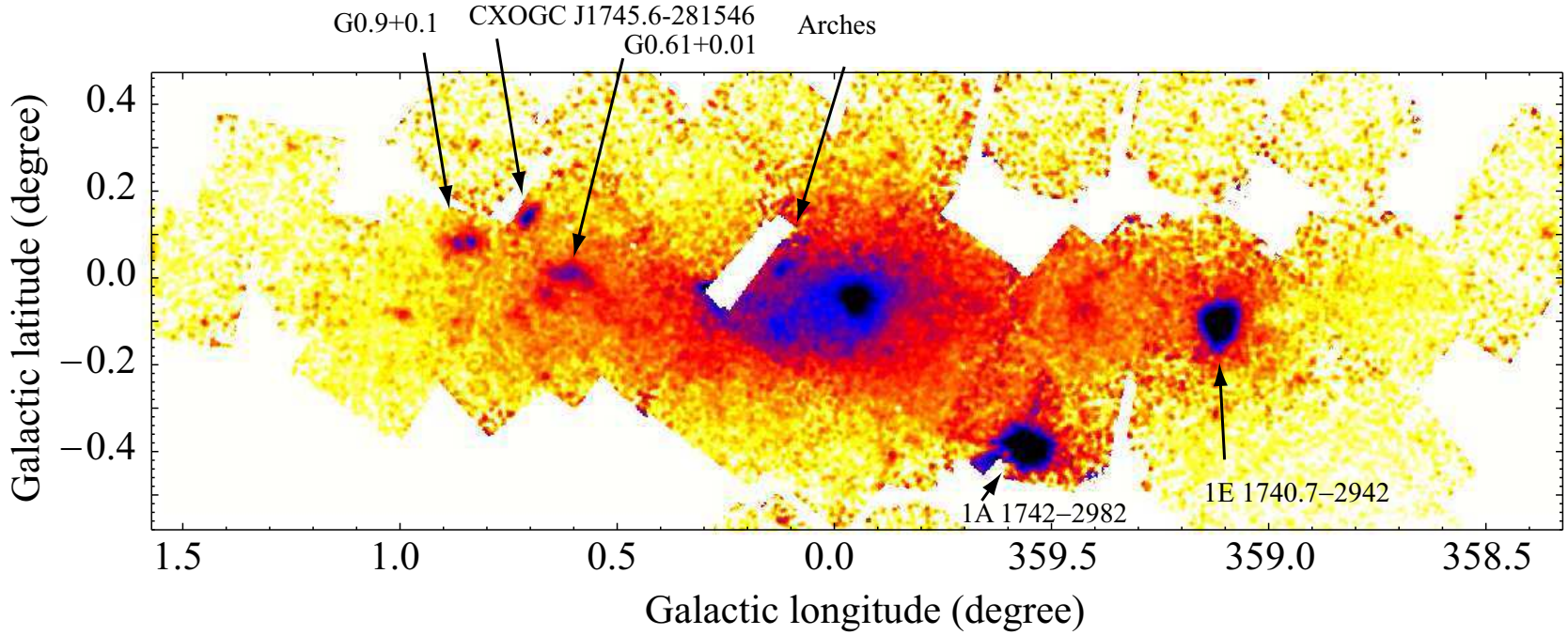

Figure 4.1: XIS mosaic image of the Galactic center region in the 6.55–6.8 keV band. The exposure correction is applied after the NXB is subtracted.

Table 4.1: Observation log of the Sgr B North region.

Start Date	ObsID	R. A.	Decl.	$t_{\rm exp}$*
		(J2000.0)		(ks)
2006-09-21	501040010	$17^{\rm h}46^{\rm m}46^{\rm s}$	$-28°22'51''$	70
2006-09-24	501040020	$17^{\rm h}46^{\rm m}46^{\rm s}$	$-28°22'51''$	50

* Exposure time after good time interval filtering described in the text.

The source was detected in the vicinity of the Sgr B molecular complex. The observations were conducted twice in 2006 September 21–23 and 24–25 (table 5.1). We removed the events taken during the South Atlantic Anomaly passages and at earth elevation angles below 3 degrees. After the filtering, the combined net integration time is $\sim$120 ks.

4.1.3 Band-limited Images & Source list

Table 4.2: Point source list in the Sgr B North region

Source Name	Position (J2000.)	
	RA	Dec
CXOGC J174645.3–281546	$17^{\rm h}46^{\rm m}45^{\rm s}$	$-28°15'56''$

Figure 4.2 shows the XIS images in the (a) 0.5–2.0 keV and (b) 2.0–7.0 keV bands. The two extended sources seen in the hard band image are Sgr B2 molecular cloud (Koyama et al., 1996; Murakami et al., 2000, 2001) and G0.61–0.01 (Koyama et al., 2007b). The brightest source near the northern edge of the FOV is the main topic of this section.

We extracted the source and background photons from the polygonal and dashed elliptical regions, respectively (figure 4.2b). We simulated a point source image at the source position using `xissim` (Ishisaki et al., 2007), and extracted source photons at various enclosed photon fractions. Consequently, we found that a 60% enclosed photon polygon maximizes the signal-to-noise ratio. The background region was selected from an ellipse adjacent to and at a similar off-axis angle with the source region.

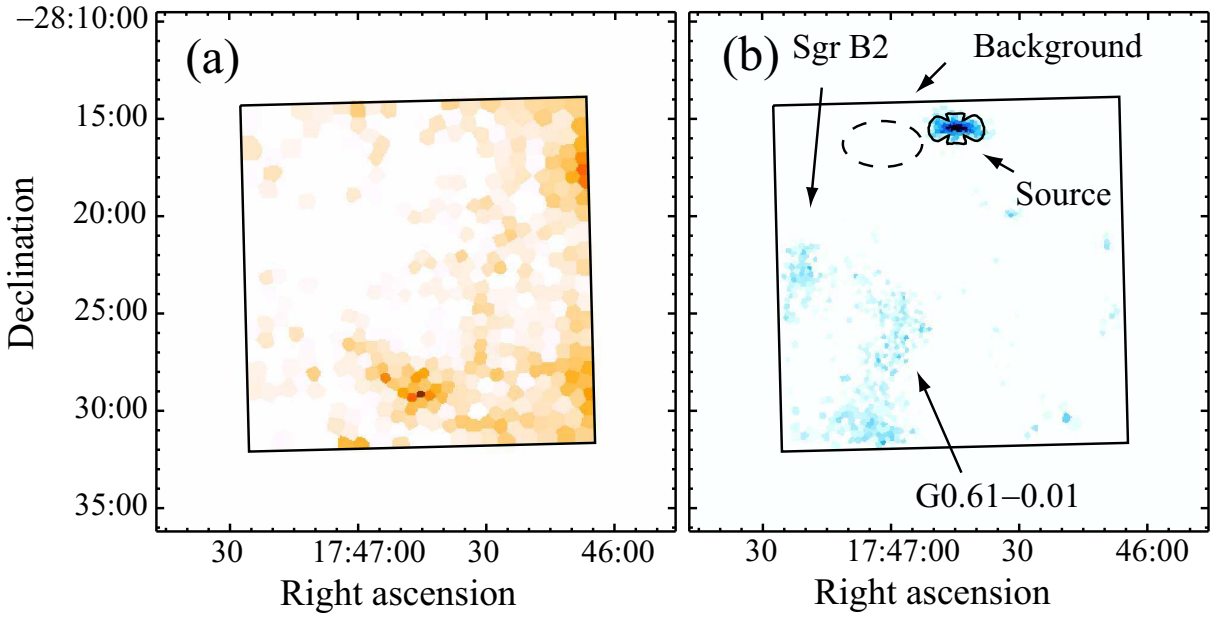

Figure 4.2: XIS images of the study field in the (a) 0.7–2.0 and (b) 2.0–7.0 keV bands. All four XIS images in the two observations are combined. The images were adaptively binned so that every bin has a signal-to-noise ratio larger than 8 using the weighted Voronoi tessellation algorithm (Cappellari et al., 2003; Diehl et al., 2006). Then, the NXB was subtracted and the vignetting was corrected. The FOV is shown with solid squares.

4.1.4 A Discrete source

Timing Analysis

Figure 4.3 shows the XIS light curve in the 2.0–7.0 keV band. The light curve with a bin width of 4000 s shows no variation. The constant model is not rejected with χ^2/degree of freedom (dof) = 67.6 / 57.

Spectral Analysis

Figure 4.4 shows the background-subtracted spectrum. Since the response function of each FI camera is essentially same and the energy gain is well calibrated, events of XIS 0, XIS 2, and XIS 3 are summed throughout this thesis. The spectrum is characterized by several emission lines as well as a hard continuum extending above 10 keV with a strong cut-off at ~ 3 keV. The lines are identified as Kα emission from highly ionized (He-like and H-like) atoms of Ar, Ca, and Fe. The spectrum was first fitted by a bremsstrahlung

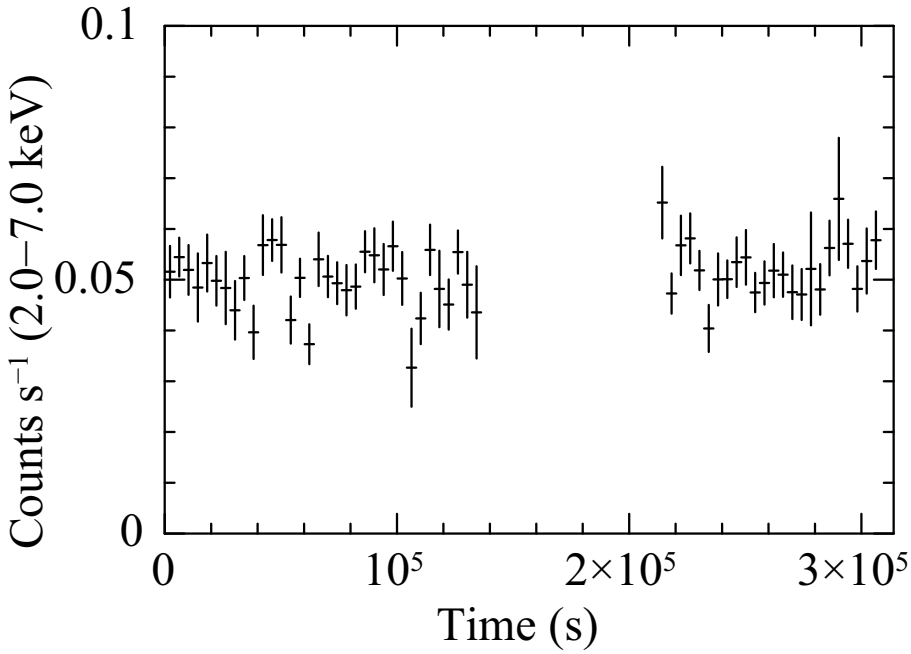

Figure 4.3: XIS light curve of CXOGC J174645.3–281546in the 2.0–7.0 keV band. The light curve is binned for each 4000 s.

model with Gaussian lines convolved by interstellar extinction (Morrison & McCammon, 1983) of solar abundances (Anders & Grevesse, 1989). We generated the ancillary response files (ARFs) of the XRT using `xissimarfgen` (Ishisaki et al., 2007) and response matrix files (RMFs) of the XIS using `xisrmfgen`. The strongest line is attributed to Fe XXIV Kα at 6.66 ± 0.01 keV with an energy flux of $(2.5 \pm 0.3) \times 10^{-13}$ erg s^{-1} cm^{-2}, which corresponds to an equivalent width (EW) of 950 ± 100 eV.

The line feature at 6.4 keV, which stems from quasi-neutral Fe and is a characteristic of the diffuse emission in this region, is not detected. By adding a narrow Gaussian line at 6.4 keV, we found a 90% upper limit of 1.5×10^{-14} erg s^{-1} cm^{-2}, which corresponds to an EW of 50 eV. Since the temperature derived from the continuum shape and those from the intensity ratios of He-like and H-like Kα lines are consistent with ~ 4 keV, the emission is inferred to originate from thermal plasma in a collisional equilibrium.

We then fitted the spectrum with an optically-thin thermal plasma model (APEC: Smith et al. 2001) with interstellar extinction. The abundances of Ar, Ca, and Fe relative to solar were left to vary, while other elements were fixed to 1 solar abundance. A single-temperature model yielded an acceptable fit with a plasma temperature ($k_{\rm B}T$) of ~ 3.8 keV, 1.0×10^{-12} erg s^{-1} cm^{-2} in X-ray flux ($F_{\rm X}$) in the 2.0–8.0 keV band and 2.4×10^{23} cm^{-2} in hydrogen column extinction ($N_{\rm H}$). No systematic deviation was found in the single temperature

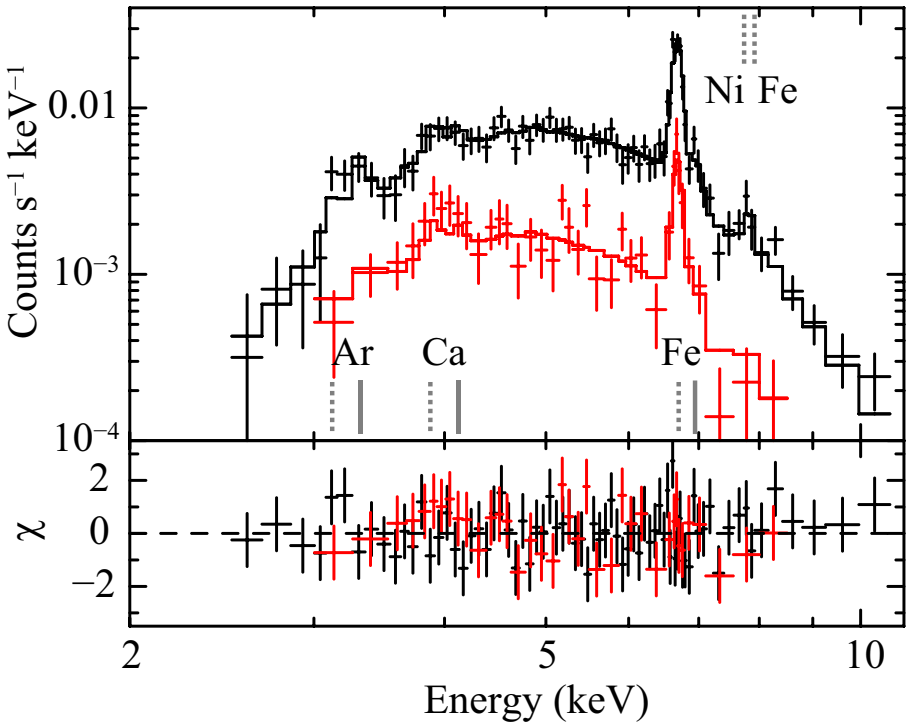

Figure 4.4: XIS spectra of CXOGC J174645.3–281546. The BI and summed FI spectra are respectively shown in black and red. The upper panel shows the data with crosses and the best-fit model with solid lines, while the lower panel shows the residual to the best-fit. Conspicuous emission lines are shown with gray dotted (He-like ion) and solid (H-like ion) lines.

fit (figure 4.4), indicating that no extra component is required.

To estimate the systematic error caused by the choice of background region, we repeated the same procedure with several different regions. Although the X-ray flux suffers $\lesssim 10\%$ systematic uncertainty, other best-fit parameters are consistent with each other.

Table 4.3: Best-fit spectral parameters.*

Parameter	Unit	Value
$N_{\rm H}$	(10^{23} cm^{-2})	$2.4^{+0.3}_{-0.2}$
$k_{\rm B}T$	(keV)	$3.8^{+0.5}_{-0.6}$
$Z_{\rm Ar}$	(solar)	$8.7^{+6.3}_{-4.9}$
$Z_{\rm Ca}$	(solar)	$3.2^{+2.3}_{-2.0}$
$Z_{\rm Fe}$	(solar)	$0.8^{+0.1}_{-0.1}$
$F_{\rm X}$†	(10^{-12} erg s^{-1} cm^{-2})	$1.00^{+0.03}_{-0.03}$
$L_{\rm X}$‡	(10^{34} erg s^{-1})	2.8
χ^2/d.o.f.		89.4/106

* The uncertainty indicates the 90% confidence ranges of the fit.
† Energy flux in the 2.0–8.0 keV band.
‡ Absorption-corrected luminosity in the 2.0–8.0 keV band. A distance of 8 kpc is assumed.

4.2 Carina Nebula

4.2.1 Objectives

In colliding wind binary systems with high eccentricity, the X-ray luminosity is expected to vary as a function of orbital phase due to the variation of volume emission measure of the plasma (Stevens et al., 1992). The spectral shape may also be modified by the variable absorption column of the cold wind material. The thermal X-ray emission from Cygnus OB2#8A (De Becker et al., 2006), η Carinae (Hamaguchi et al., 2007b), and WR 140 (Pollock et al., 2005) clearly depends on the orbital phase, implying that a major part of the plasma is produced by wind collision. For such study, repeated X-ray observations with a typical orbital period of massive stars binary of 100–1000 days are necessary.

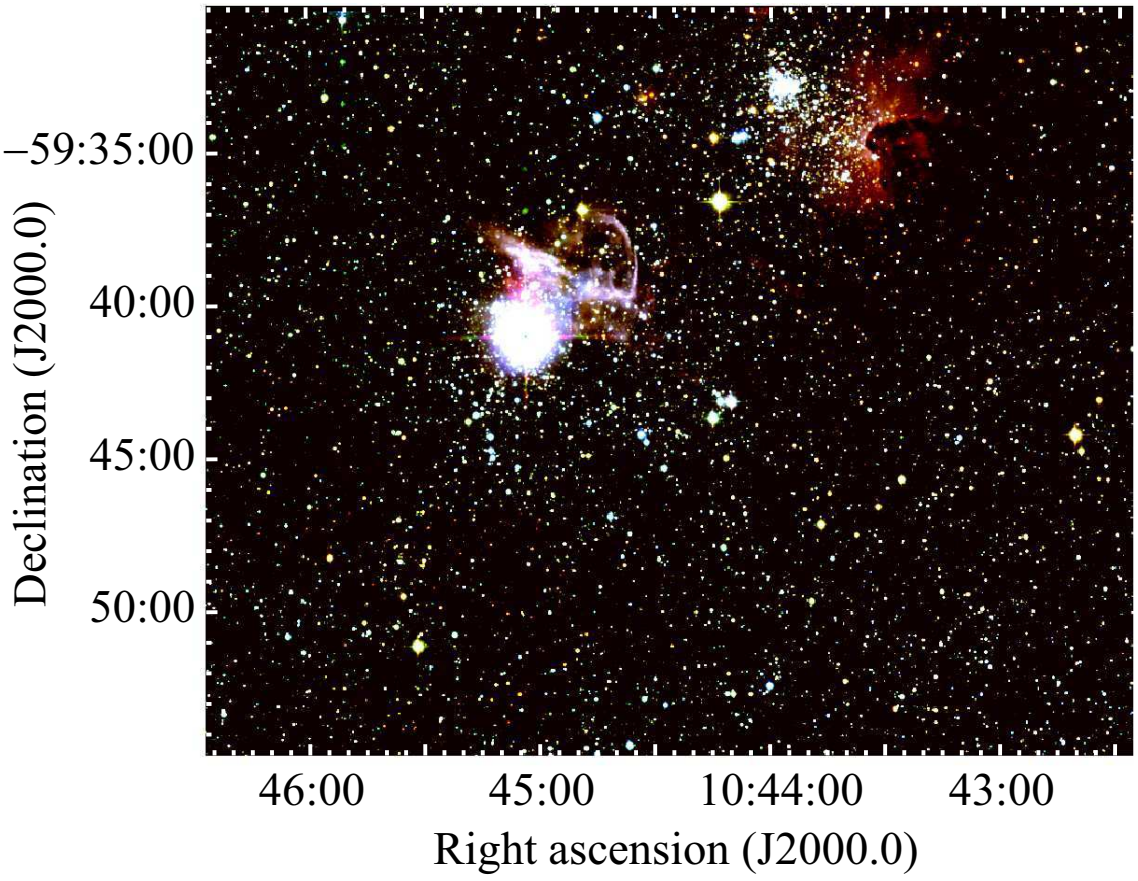

Figure 4.5: 2MASS image of the Carina Nebula. J, H, and K band intensities are shown in blue, green, and red, respectively.

The Carina Nebula is one of the brightest H II regions in the sky, which is composed of several star clusters (Trumpler 14–16, Collinder 228 and 232, and Bochum 10 and 11). This region harbours more than 64 O stars (Smith, 2006), including the luminous blue variable η Carinae, the WR star HD 93162 (=WR 25), the main-sequence O3 star (HD 93205), and the main-sequence O3+O8 binary (HD 93250). With the proximity of ~ 2.3 kpc (Davidson & Humphreys, 1997), the Carina region is one of the best regions in the Galaxy for systematic studies of massive stars. Actually, this region is extensively studied by Chandra (Evans et al., 2003, 2004; Sanchawala et al., 2007; Albacete-Colombo et al., 2008) and XMM-Newton (Albacete Colombo et al., 2003; Antokhin et al., 2008). Fortunately, the region is observed by Suzaku and other satellites repeatedly, as η Car is often used for a routine calibration source. Many early-type stars are within the fields of view. This rich data set is ideal to study long-term behaviors of these massive stars.

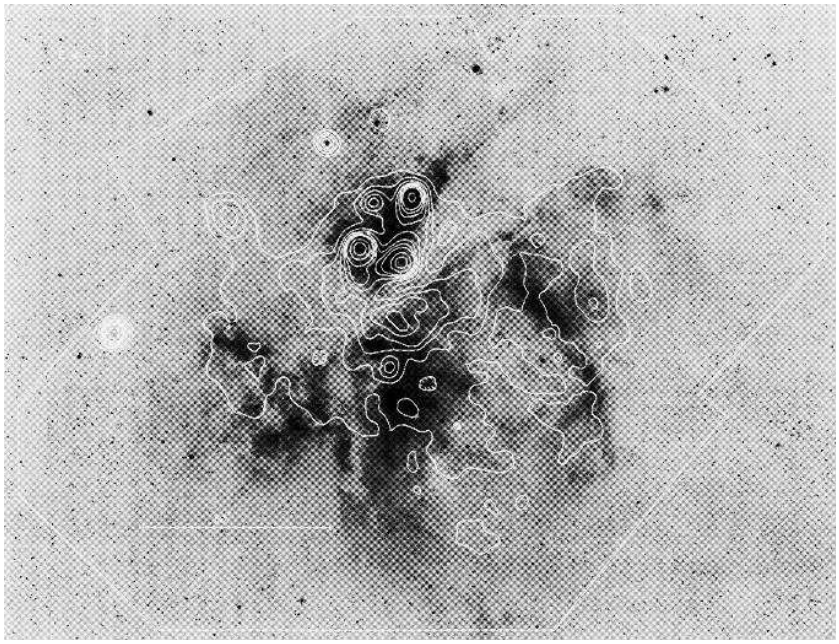

Figure 4.6: Einstein/IPC contour of the Carina Nebula overlaid on the B band image.

This region is also distinctive for the diffuse X-ray emission discovered by the Einstein observatory (Seward et al., 1979; Seward & Chlebowski, 1982). The emission extends over ~ 1 deg^2 with a total X-ray luminosity of $\sim 10^{35}$ erg s^{-1}. Hamaguchi et al. (2007) showed that the X-ray spectra are different between the north and south sides of η Carinae, especially below 1 keV. They argued that Fe and Si abundances in the south region are higher than those in the north region with a factor of 2–4 and N to O abundance is low ($\lesssim 0.4$). The authors concluded that the diffuse emission originates not from wind-blown bubbles, but from one or multiple supernova remnant(s).

4.2.2 Observations & Reduction

Table 4.4: Observation log of the Carina Nebula.

Start Date	ObsID	R. A.	Decl.	$t_{\rm exp}$*
		(J2000.0)		(ks)
2005-08-29	100012010	$10^{\rm h}45^{\rm m}07^{\rm s}$	$-59°41'04''$	68
2006-02-03	100045010	$10^{\rm h}44^{\rm m}59^{\rm s}$	$-59°41'09''$	22
2007-06-23	402039010	$10^{\rm h}44^{\rm m}52^{\rm s}$	$-59°43'41''$	63
2008-06-10	403035010	$10^{\rm h}44^{\rm m}55^{\rm s}$	$-59°43'53''$	35

* Exposure time after good time interval filtering described in the text.

Suzaku observed η Carinae four times (table 4.4). The former two observations were conducted at the XIS nominal position and without the SCI, while the latter two observations were conducted at the HXD nominal position and with the SCI. XIS 2 was not used in the latter two observations. Data taken at elevation angles below 4° from the Earth rim and 10° from the sunlit Earth rim were discarded. All data were processes using ver. 2.3 of the Suzaku pipeline software.

4.2.3 Band-limited Images & Source list

Table 4.5: Point source list in the Carina Nebula region

Source Name	Position (J2000.)		Spectral Type	Reference
	RA	Dec		
WR 25	$10^{\rm h}44^{\rm m}10^{\rm s}$	$-59°43'11''$	WN6+O4	1
HD 93205	$10^{\rm h}44^{\rm m}34^{\rm s}$	$-59°44'16''$	O3 V+O8 V	2, 3
HD 93250	$10^{\rm h}44^{\rm m}45^{\rm s}$	$-59°33'54''$	O3 V	2

References. — (1) van der Hucht (2001) (2) Levato et al. (1991) (3) Morrell et al. (2001)

Figure 4.7 shows the XIS images of the Carina region in the (a) soft (0.5–2.0 keV) and (b) hard (2.0–5.0 keV) bands. We see extended emission in the northeastern and south part of the field in the soft band, whereas the emission from point sources dominate the hard band image. Since Hamaguchi et al. (2007) argued that the diffuse emission shows spatial variation particularly in the soft band, we further divided the 0.5–2.0 keV events into three bands (0.5–0.7 keV, 0.7–1.0 keV, and 1.0–2.0 keV) to make a three color image (figure 4.8).

The uncertainty of the XIS sky coordinates is $\sim 20''$ (Uchiyama et al., 2008). To achieve

a higher astrometric accuracy, we registered the XIS frame using the three bright point sources (WR 25, HD 93205, and HD 93250). We do not use η Car, which has an extended structure in X-rays. We referred the sky position determined with Chandra (Evans et al., 2003), and shifted the XIS frame in each observation by 8–15″. The accuracy of the Chandra frame is $\sim 0.''5$.

We analyze the three point sources, WR 25, HD 93205, and HD 93250, which have not been discussed in detail in previous work (Hamaguchi et al., 2007). HD 93250 was out of the FOV in the latter two observations, while WR 25 and HD 93205 were detected in all of the four observations. We also analyze the diffuse emission according to the emission morphology (figure 4.8).

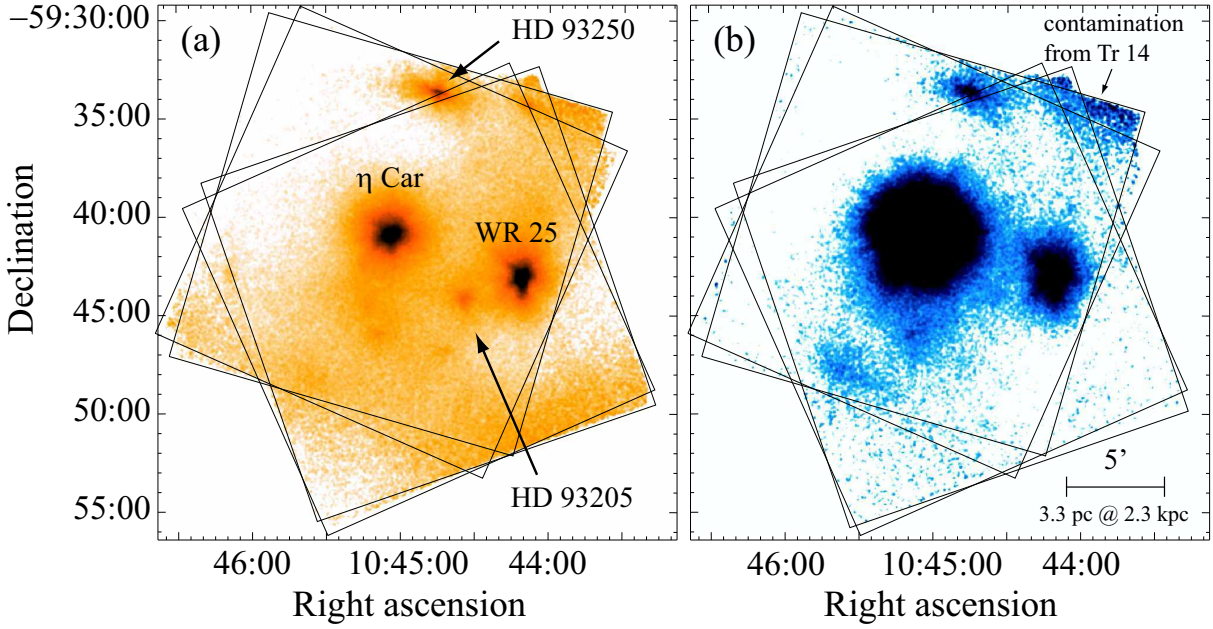

Figure 4.7: XIS images of Carina Nebula in the (a) 0.5–2.0 keV and (b) 2.0–5.0 keV bands. The FOVs of each observation are shown with solid squares.

4.2.4 Discrete Sources

Timing Analysis

We present the temporal and spectral behaviors of the three massive stars (table 4.5). Source photons are accumulated from elliptical regions of 40″–90″ in the axis lengths, while the background photons are from adjacent regions free of sources. The source light curves are

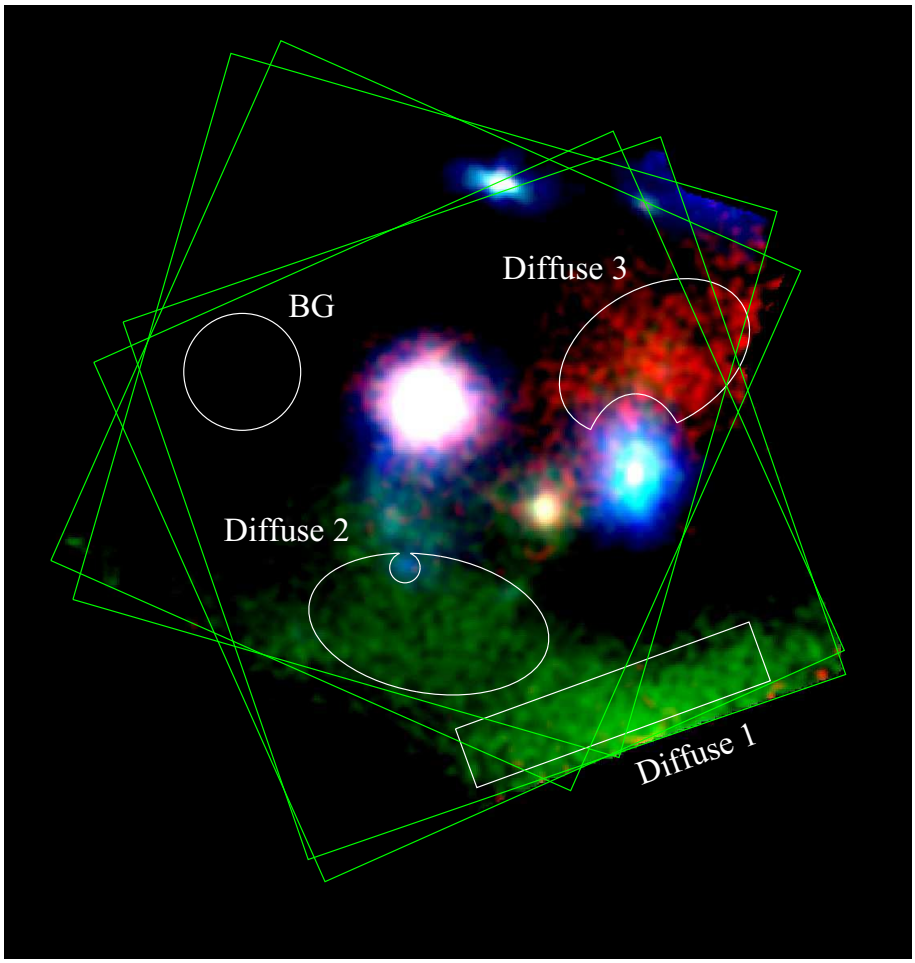

Figure 4.8: Three color image of the Carina Nebula in the soft band. The events in 0.5–0.7 keV, 0.7–1.0 keV, and 1.0–2.0 keV are shown in red, green, and blue, respectively. The FOVs of the four observations and the photon extraction regions are shown in are shown in green and white solid lines.

shown in figures 4.9–4.11. None of the three sources shows flux variation in each observation.

Spectral Analysis

Figures 4.12–4.14 show the spectra of the three sources. We see emission lines from highly ionized O, Ne, Mg, Si, S, and Fe, indicating an optically-thin thermal plasma origin. We then fitted the spectra with the APEC model attenuated by interstellar absorption. The summed FI and the BI spectra were fitted simultaneously. We first fitted the spectra with a single temperature model. If this model is rejected, an additional component with

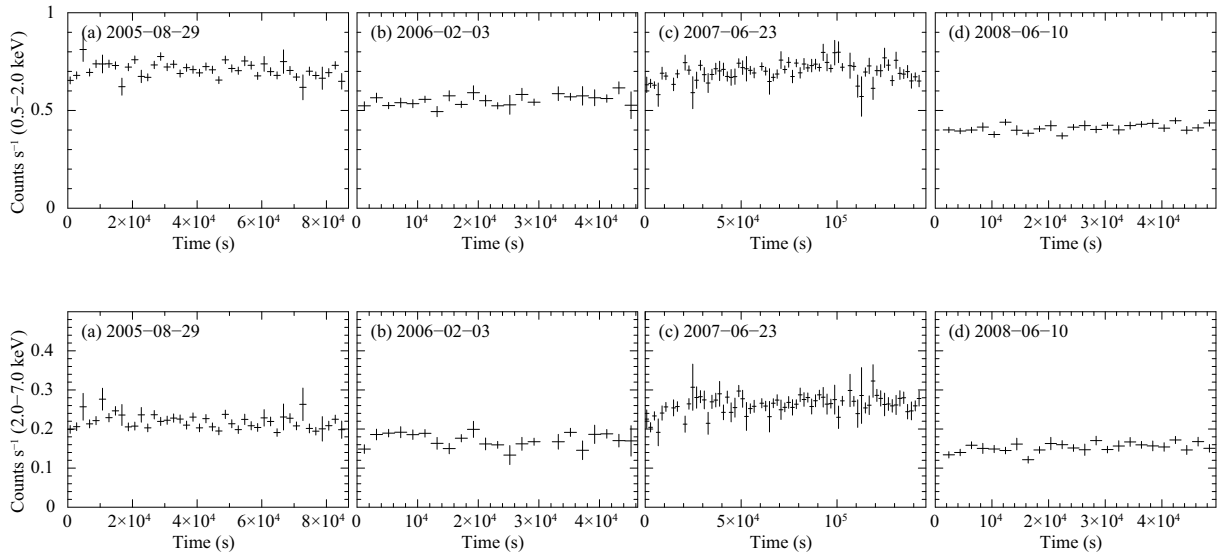

Figure 4.9: XIS light curves of WR 25. Upper and lower panels show the count rate in the soft (0.5–2.0 keV) and hard (2.0–7.0 keV) bands respectively.

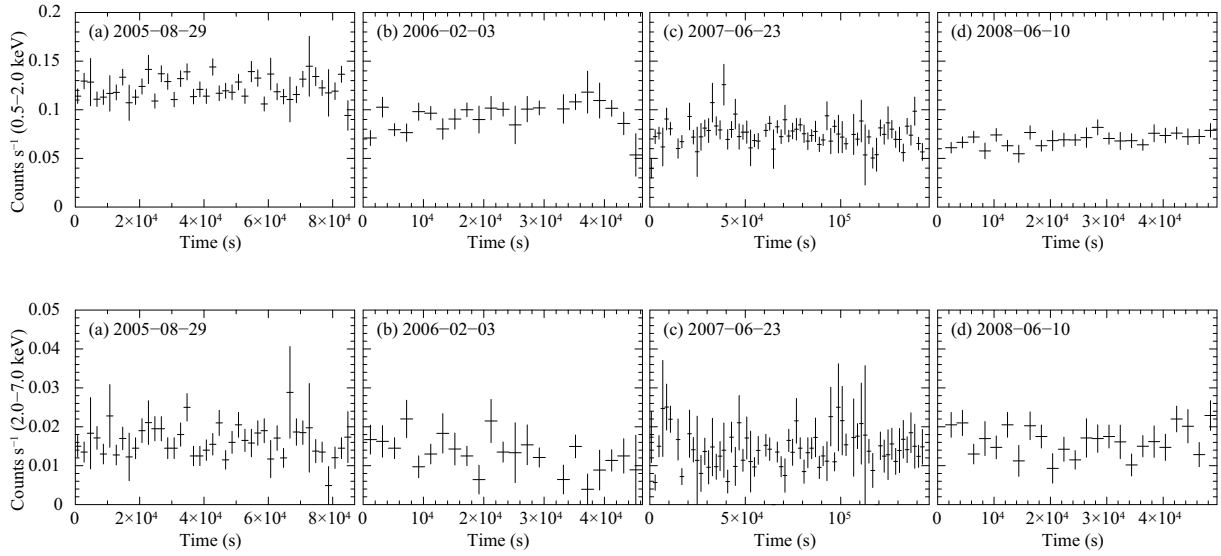

Figure 4.10: XIS light curves of HD 93205. Symbols follow figure 4.9.

a different temperature was added. The elemental abundances other than He was assumed to be common. The best-fit parameters are shown in tables 4.6–4.8. While the spectra of WR 25 and HD 93250 required two components of different temperatures, that of HD 93205 was well reproduced with a single-temperature component.

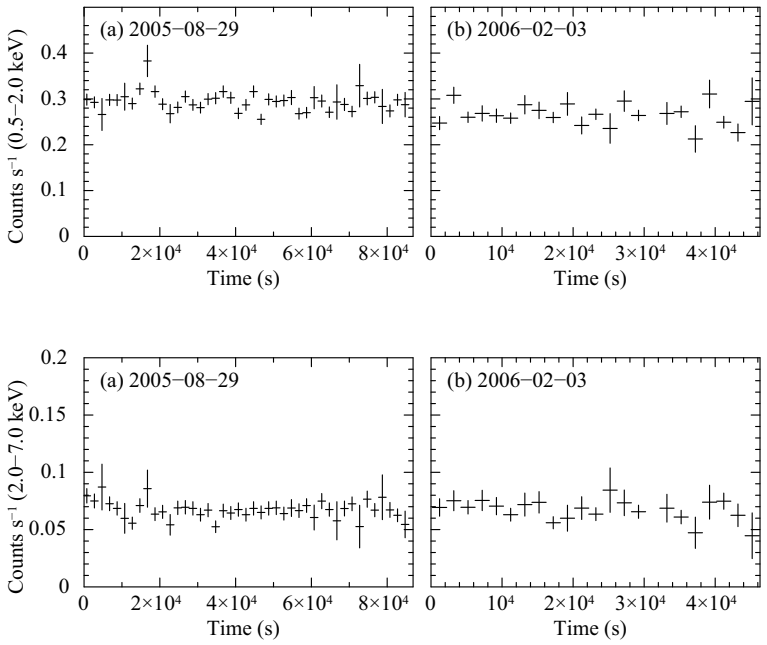

Figure 4.11: Same as figure 4.9, but for HD 93250.

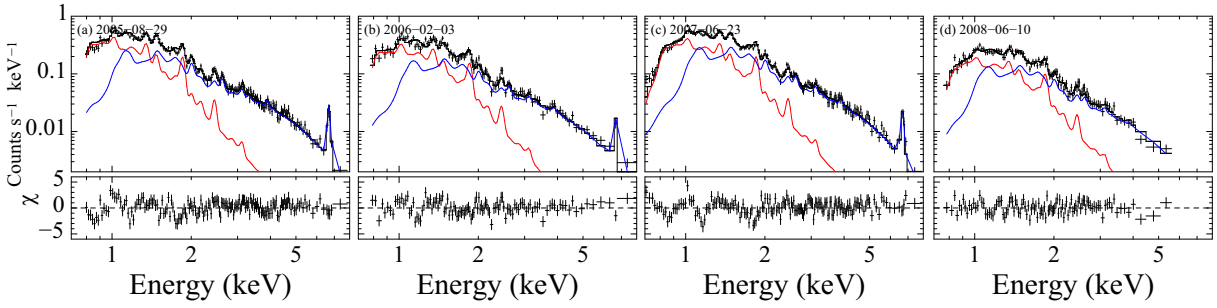

Figure 4.12: XIS spectra of WR25. Only FI spectra are shown for simplicity. The lower and higher temperature components are shown in red and blue, respectively.

Since spectral shapes of the all sources did not change significantly, we summed the photons from the four observations of WR 25 and HD 93205 and, the two former observations of HD 93250 in order to increase the photon statistics. The spectra were not well reproduced by one- or two- temperature APEC models. Allowing the elemental abundance of conspicuous emission lines to vary, we obtained acceptable fitting results. The best-fit parameters and the spectra are presented in table 4.9 and figures 4.15–4.17.

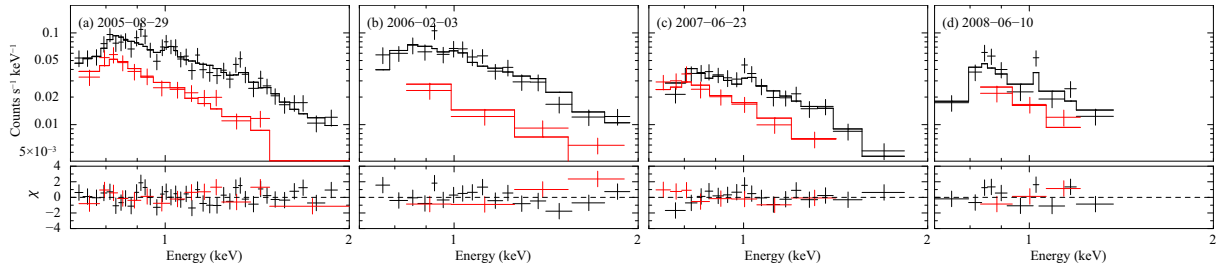

Figure 4.13: XIS spectra of HD 93205. The summed FI and BI spectra are shown in black and red, respectively.

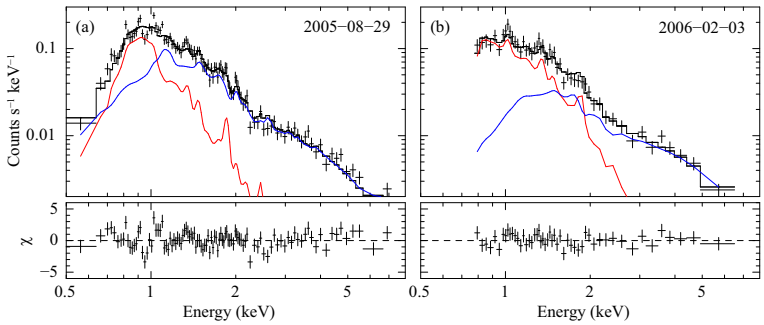

Figure 4.14: XIS spectra of HD 93250. Only FI spectra are shown for simplicity. The lower and higher temperature components are shown in red and blue, respectively.

Table 4.6: Best-fit parameters of WR 25.

Obs. Date (yyyy-mm-dd)	$N_{\rm H}$ (10^{21} cm^{-2})	$k_{\rm B}T_1$ (keV)	$k_{\rm B}T_2$ (keV)	Z (solar)	$F_{\rm X}$ (erg s^{-1} cm^{-2})
2005-08-29	8.1±0.3	0.63±0.01	2.3±0.1	0.7	4.8×10^{-12}
2006-02-03	8.2±0.5	0.61±0.03	2.3±0.1	0.7	4.1×10^{-12}
2007-06-23	7.3±0.2	0.63±0.01	2.1±0.1	0.6	6.8×10^{-12}
2008-06-10	7.2±0.5	0.64±0.02	1.8±0.1	0.4	3.8×10^{-12}

Table 4.7: Best-fit parameters of HD 93205.

Obs. Date (yyyy-mm-dd)	$N_{\rm H}$ (10^{21} cm^{-2})	$k_{\rm B}T$ (keV)	Z (solar)	$F_{\rm X}$ (erg s^{-1} cm^{-2})
2005-08-29	<2.7	0.58±0.05	0.06	4.3×10^{-13}
2006-02-03	<4.7	0.62±0.11	0.08	4.5×10^{-13}
2007-06-23	<2.0	0.58±0.05	0.04	4.4×10^{-13}
2008-06-10	2.7±1.1	0.54±0.06	1.0	4.0×10^{-13}

Table 4.8: Best-fit parameters of HD 93250.

Obs. Date (yyyy-mm-dd)	$N_{\rm H}$ (10^{21} cm^{-2})	$k_{\rm B}T_1$ (keV)	$k_{\rm B}T_2$ (keV)	Z (solar)	$F_{\rm X}$ (erg s^{-1} cm^{-2})
2005-08-29	1.8±0.5	0.73±0.03	3.0±0.2	0.7	1.3×10^{-12}
2006-02-03	4.8±1.4	0.60±0.03	$4.8^{+4.5}_{-1.6}$	0.7	1.3×10^{-12}

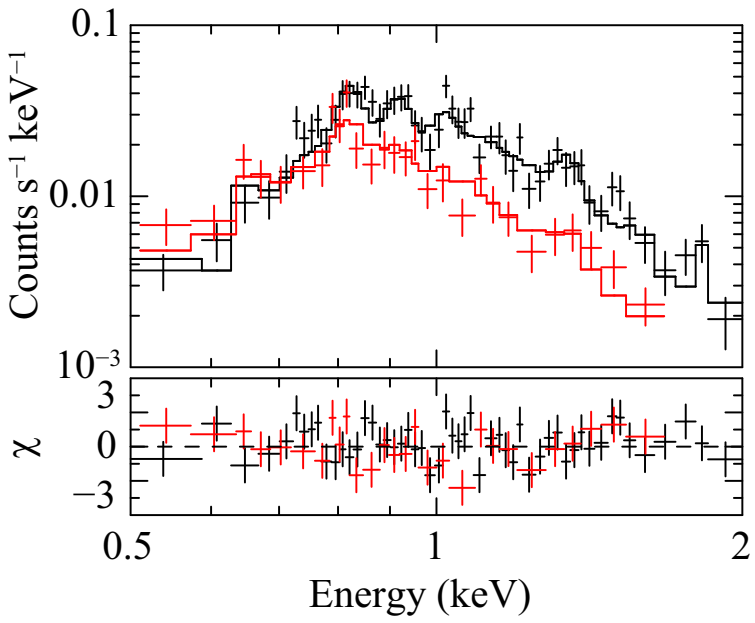

Figure 4.15: XIS spectrum of HD 93205. The summed FI and BI spectra are shown in black and red.

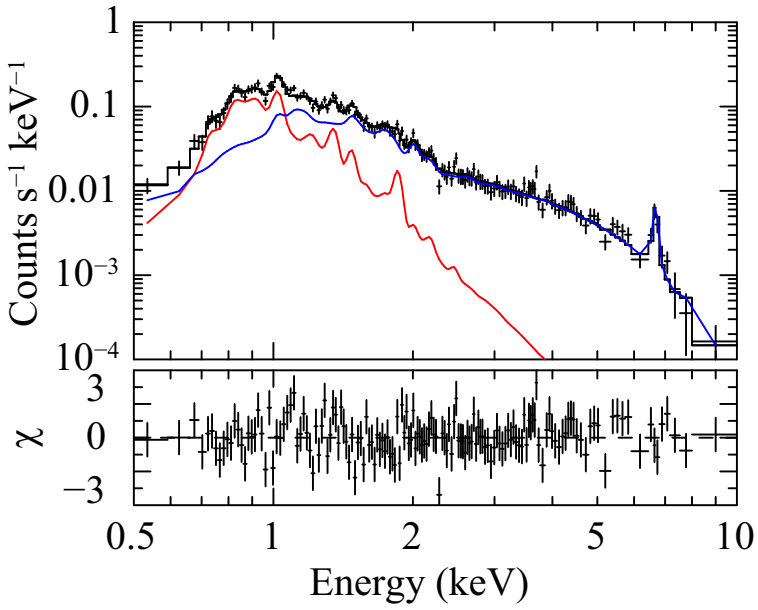

Figure 4.16: XIS spectrum of HD 93250. The summed FI spectrum shown with crosses. The lower and higher temperature components are shown in red and blue, respectively.

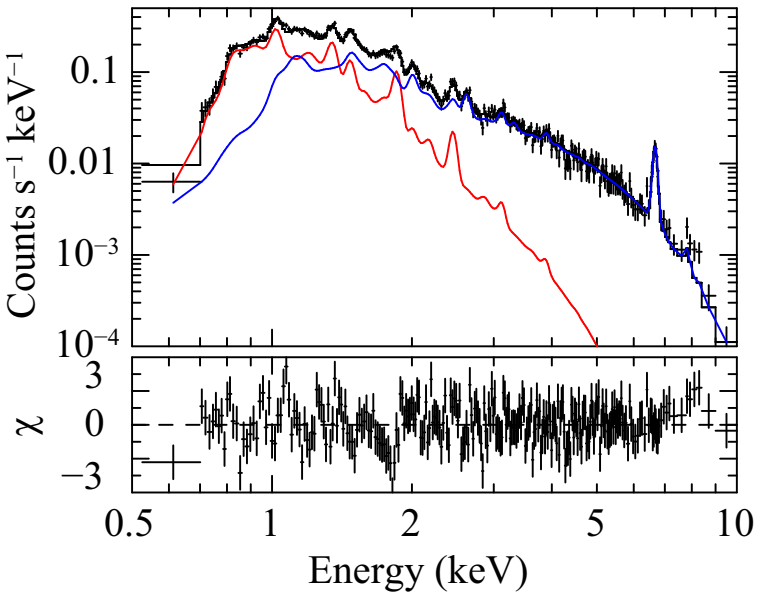

Figure 4.17: XIS spectrum of WR 25. Only FI spectra are shown for simplicity. The lower and higher temperature components are shown in red and blue, respectively.

Table 4.9: Best-fit APEC parameters for HD 93205, HD 93250, WR 25

Pars.	Units	HD 93205	HD 93250	WR 25
$N_{\rm H}{}^{*}$	(10^{21} cm^{-2})	$5.2^{+0.3}_{-0.9}$	2.2±0.4	7.1±0.4
$k_{\rm B}T_{\rm high}{}^{*\dagger}$	(keV)	...	3.1±0.2	2.33±0.06
$k_{\rm B}T_{\rm low}{}^{*\dagger}$	(keV)	$0.25^{+0.04}_{-0.02}$	0.62±0.03	0.62±0.01
$Z_{\rm Ne}{}^{*}$	(solar)	0.3	0.3	0.51 (0.34–0.71)
$Z_{\rm Mg}{}^{*}$	(solar)	0.49 (0.24–0.87)	0.3	0.51 (0.38–0.65)
$Z_{\rm Si}{}^{*}$	(solar)	1.07 (0.58–1.72)	0.3	0.53 (0.39–0.71)
$Z_{\rm S}{}^{*}$	(solar)	0.3	0.3	1.17 (0.98–1.38)
$Z_{\rm Ar}{}^{*}$	(solar)	0.3	1.67 (0.72–3.00)	1.44 (1.00–1.90)
$Z_{\rm Ca}{}^{*}$	(solar)	0.3	0.3	0.46 (0.01–0.90)
$Z_{\rm Fe}{}^{*}$	(solar)	0.33 (0.19–0.48)	0.36 (0.22–0.50)	0.28 (0.25–0.31)
$F_{\rm X}{}^{*\ddagger}$	(10^{-13} erg s^{-1} cm^{-2})	3.9 (3.8–4.0)	7.4 (7.1–7.7)	58.3 (57.8–58.8)
$L_{\rm X}{}^{\S}$	(10^{32} erg s^{-1})	3.2	4.9	30.0
χ^2/d.o.f.	.....	100.2/134	66.4/76	473.3/405

* The uncertainties in the parentheses are the 90% confidence range. Fixed values are shown without ranges.

† The plasma temperatures for the higher and lower temperature components. Only the higher temperature value is given for HD 93205, which is fitted by a single temperature model.

‡ The X-ray flux in the 1.0–8.0 keV band.

§ The absorption-corrected X-ray luminosity in the 1.0–8.0 keV band. A distance of 2.3 kpc is assumed.

4.2.5 Diffuse Sources

Based on the morphology, we extracted the source photons of diffuse emission from three regions ("Diffuse 1", "Diffuse 2", and "Diffuse 3" in figure 4.8). The background photons were accumulated from a region devoid of bright point sources and intense diffuse emission ("BG" in figure 4.8).

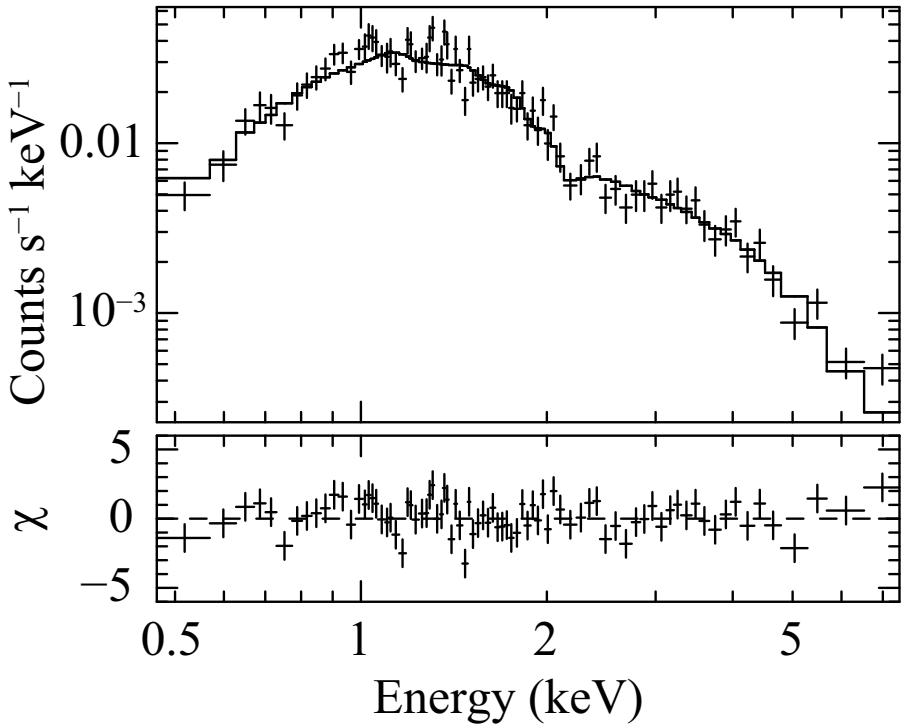

Figure 4.18: ACIS spectrum of integrated point sources in the Diffuse 3 region.

Many point sources contaminate the source spectra, especially in the "Diffuse 3" region. We estimate the point source emission observed with the XIS based on the position and flux derived by a Chandra observation. We used the Trumpler 14 observation (ObsID = 4495) covering the whole "Diffuse 3" region and detected 30 point sources using the `wavdetect` algorithm. Source and background photons were extracted using the ACIS Extract package (Broos et al., 2002). The spectrum was well described with a single temperature ($k_{\rm B}T \sim$ 4.3 keV) APEC model (figure 4.18). Using the position and flux of each source, we simulated the XIS events of point sources with `xissim`. We extracted the integrated point source spectrum and subtracted it from the diffuse spectrum.

Out-of-time events from η Carinae are not negligible in the SCI-on observations. It takes $\sim$ 127 ms to inject the SCI charges and $\sim$ 25 ms to read out the events. The "Diffuse 3"

region lies at almost the same ActY coordinate with $\sim 6'$ length in ActY direction. Therefore, $\sim (0.127+0.025)/8 \times (6/18) \sim 0.6\%$ of the η Carinae events contaminates the Diffuse 3 spectra obtained by XIS 0 and XIS 3. This effect was canceled by subtracting a normalized η Carinae spectrum by XIS.

The resultant spectra were well reproduced by an APEC model modified by an interstellar photo-electric absorption. The best-fit model and parameters are shown in figure 4.19 and table 4.10. Since the temperatures and the relative metal abundances are consistent between diffuse 1 and 2, we simultaneously fitted the spectra of two regions to obtain more constrained abundances. We tied the temperature and abundances of O, Ne, Mg, and Fe. The resultant abundances are $Z_{\rm O} = 0.05^{+0.04}_{-0.03}$, $Z_{\rm Ne} = 0.09^{+0.04}_{-0.03}$, $Z_{\rm Mg} = 0.15 \pm 0.04$, and $Z_{\rm Fe} = 0.27 \pm 0.03$.

Table 4.10: Best-fit parameters of the APEC model for the diffuse emission.*

Par.	Unit	Diffuse 1	Diffuse 2	Diffuse 3
$N_{\rm H}$	$(10^{21}$ cm$^{-2})$	< 0.1	0.6 ± 0.2	3.6 ± 0.3
$k_{\rm B}T$	(keV)	$0.55^{+0.01}_{-0.03}$	0.56 ± 0.01	0.18 ± 0.01
$Z_{\rm O}$	(solar)	$0.25^{+0.14}_{-0.08}$	< 0.06	0.09 ± 0.01
$Z_{\rm Ne}$	(solar)	0.25 ± 0.10	0.04 ± 0.04	0.16 ± 0.03
$Z_{\rm Mg}$	(solar)	0.22 ± 0.10	0.17 ± 0.04	0.32 ± 0.11
$Z_{\rm Fe}$	(solar)	$0.51^{+0.14}_{-0.08}$	0.21 ± 0.02	$0.19^{+0.09}_{-0.05}$
$F_{\rm X}$†	$(10^{-13}$ erg s^{-1} cm$^{-2})$	17 ± 3	14 ± 2	32 ± 2
$S_{\rm X}$‡	$(10^{-13}$ erg s^{-1} cm^{-2} arcmin$^{-2})$	0.9 ± 0.1	0.6 ± 0.1	2.1 ± 0.1
$L_{\rm X}$§	$(10^{33}$ erg s$^{-1})$	1.1	1.1	16

* The uncertainties indicate the 90% confidence range.

† X-ray flux in the 0.5–2.0 keV band.

‡ X-ray surface brightness in the 0.5–2.0 keV band.

§ Absorption-corrected X-ray luminosity in the 0.5–2.0 keV band. A distance of 2.3 kpc is assumed.

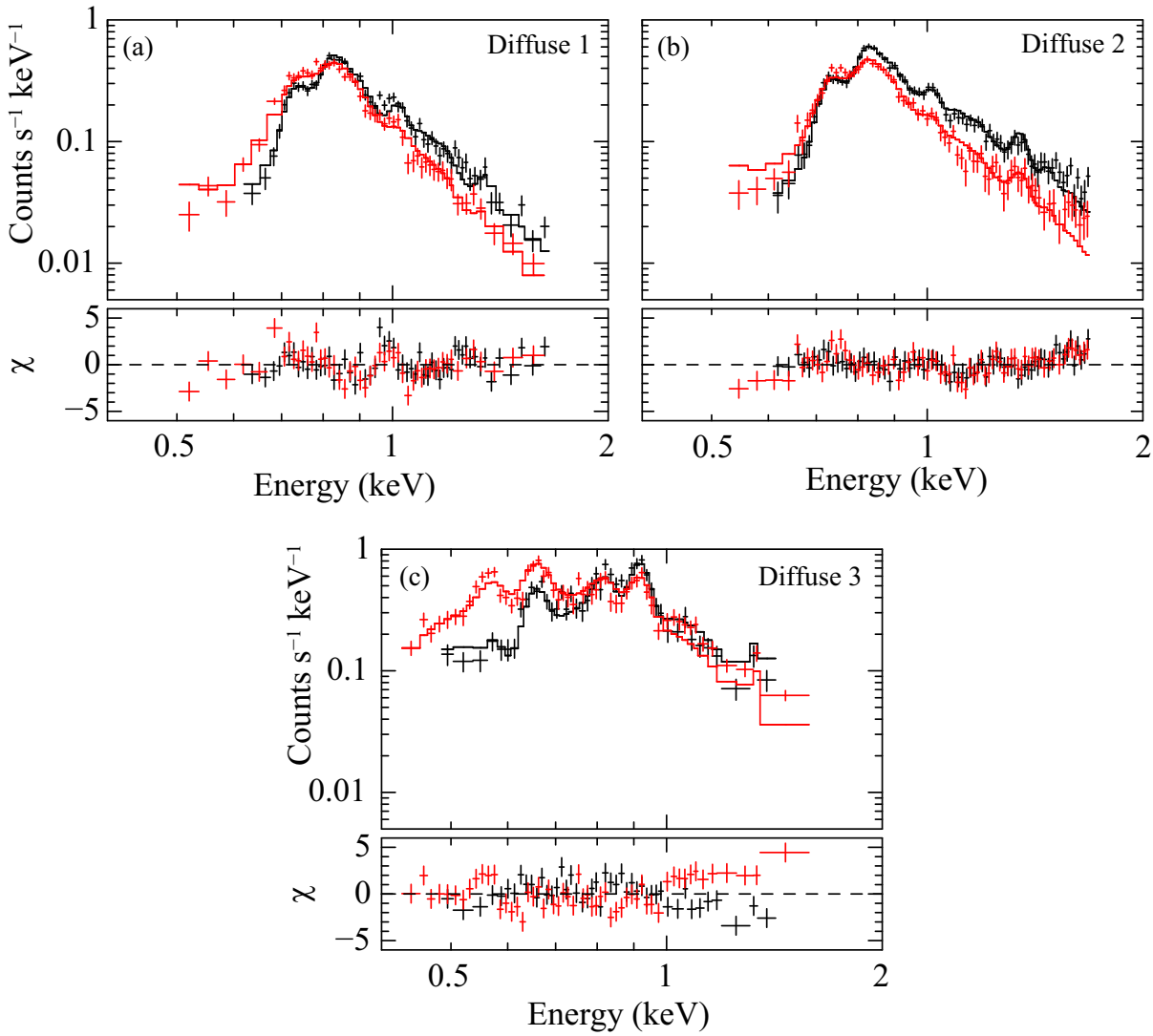

Figure 4.19: Background-subtracted spectra of diffuse emission in the Carina Nebula region. The summed FI and BI spectra are shown in black and red.

4.3 M 17

4.3.1 Objectives

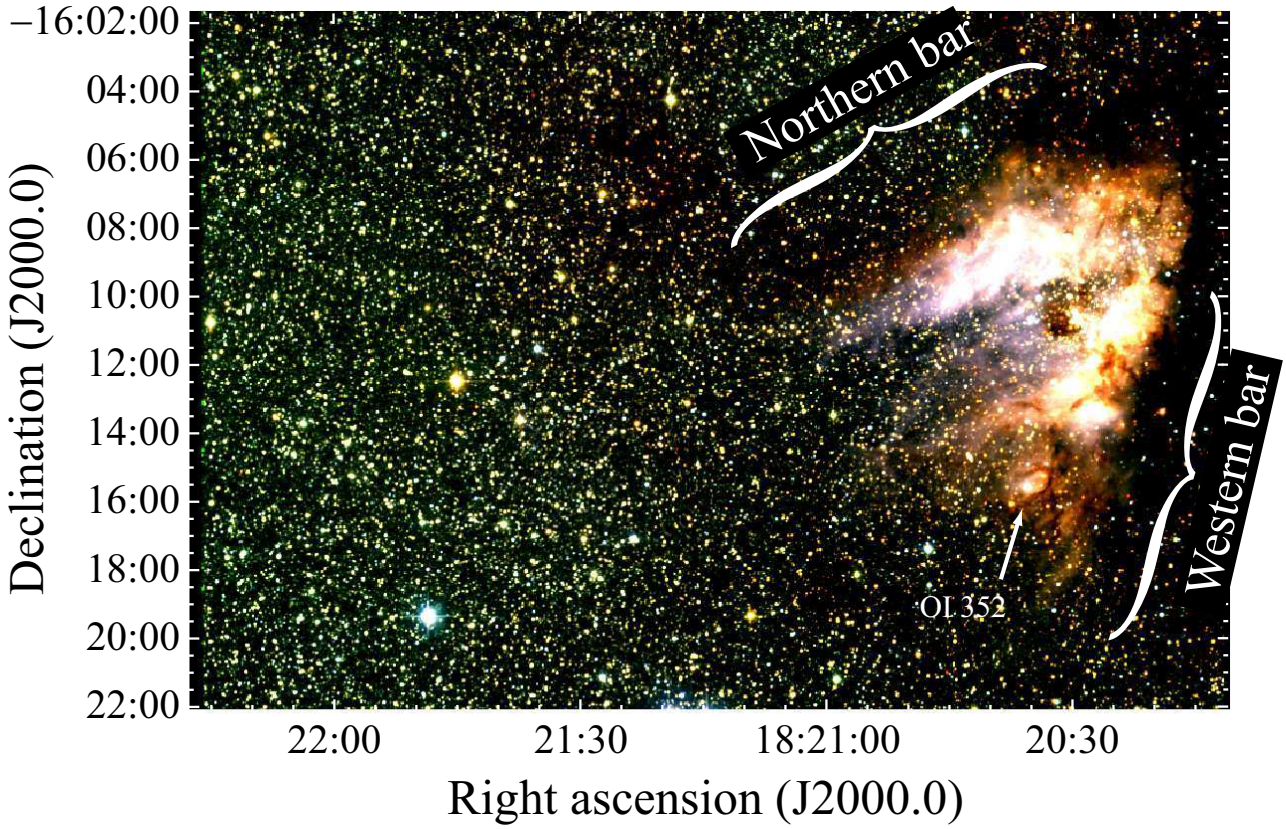

Figure 4.20: 2MASS J (blue), H (green), and K (red) mosaic image of the M 17 region.

M 17 (Omega Nebula) is a nearby Galactic H II region associated with giant molecular clouds (figure 4.20). Hoffmeister et al. (2008) identified 53 OB stars in the central OB association with near infrared spectroscopy and derived the distance to be 2.1 ± 0.2 kpc. A much larger number of young OB stars are suggested by near infrared photometry (Lada et al., 1991; Jiang et al., 2002). The earliest systems are two O4 binaries (CEN 1a and CEN 1b). The age of the cluster is estimated to be $\lesssim 1$ Myr based on the H-R diagram (Hanson et al., 1997; Hoffmeister et al., 2008). Strong winds and radiation from the central OB association sculpted the ambient matter to form a V-shaped cloud, which was traced by molecular and atomic hydrogen lines (Chrysostomou et al., 1992; Felli et al., 1984; Brogan & Troland, 2001). Each side of the V is called Northern and Western bars (figure 4.20).

The diffuse X-ray emission was found by Chandra and ROSAT (Townsley et al., 2003; Dunne et al., 2003). It has asymmetric morphology with respect to the OB association and fills the cavity of the molecular cloud toward the negative Galactic latitude (Povich et al., 2007; Pellegrini et al., 2007).

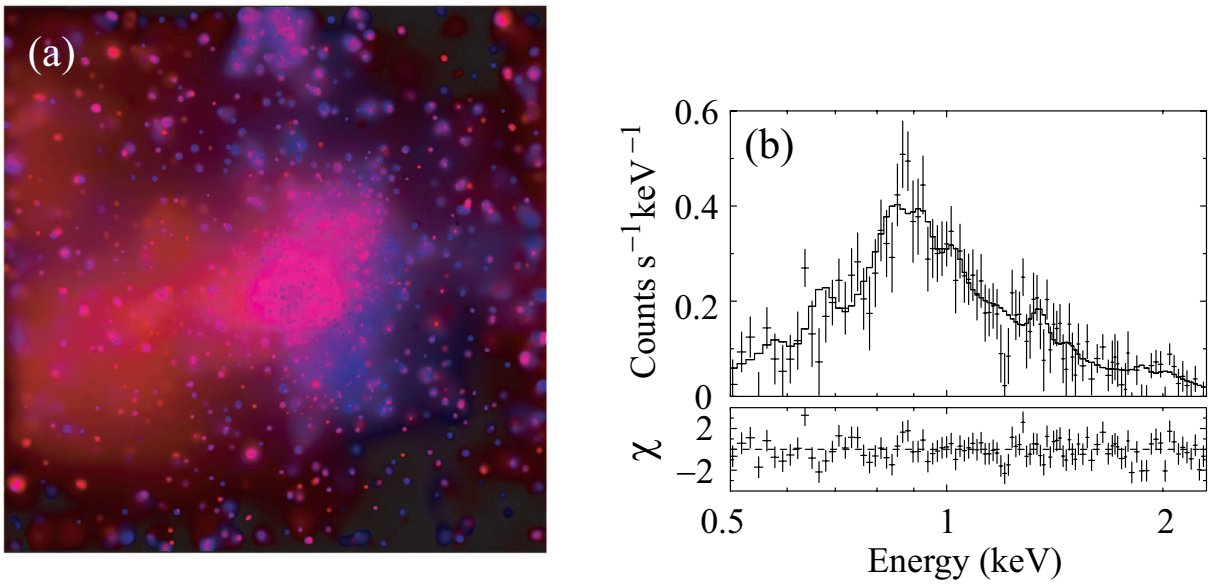

Figure 4.21: (a) Chandra image of M 17 with adaptive smoothing and exposure corrction. Low- (0.5–2.0 keV) and high- (2.0–8.0 keV) energy events are shown in red and blue. (b) Chandra/ACIS spectrum of the diffuse emission in M 17. The top panel shows the data in crosses and the best-fit model in the solid line, while the bottom panel shows the residual (Townsley et al., 2003).

Townsley et al. (2003) claimed the first unambiguous detections of such emission in the H II regions M 17 and the Rosette Nebula using the Advanced CCD Imaging Spectrometer (ACIS; Garmire et al. 2003) onboard the Chandra X-ray Observatory (Weisskopf et al., 2002). With a $\sim$40 ks integration time of M 17 (ObsID = 972), diffuse soft X-ray emission was detected (figure 4.21) apart from 886 point sources above $\sim 10^{29.3}$ erg s^{-1} (Broos et al., 2007). Dunne et al. (2003) showed the entire structure of the soft X-ray diffuse emission (figure 4.22) using the Position-Sensitive Proportional Counter (PSPC; Pfeffermann et al. 1987) onboard ROSAT (Truemper, 1982). They measured the total X-ray luminosity and compared to the wind-blown bubble models with and without heat conduction. They concluded that only the bubble without heat conduction can account for the observed X-ray luminosity of $\sim 2.5 \times 10^{33}$ erg s^{-1}. The magnetic field may be responsible for suppressing the heat conduction and mass evaporation between the hot gas and cold ISM (Dunne et al., 2003).

The results obtained by these high-resolution imaging studies are generally consistent with the wind-blown bubble models. However, the observational results are not still accurate

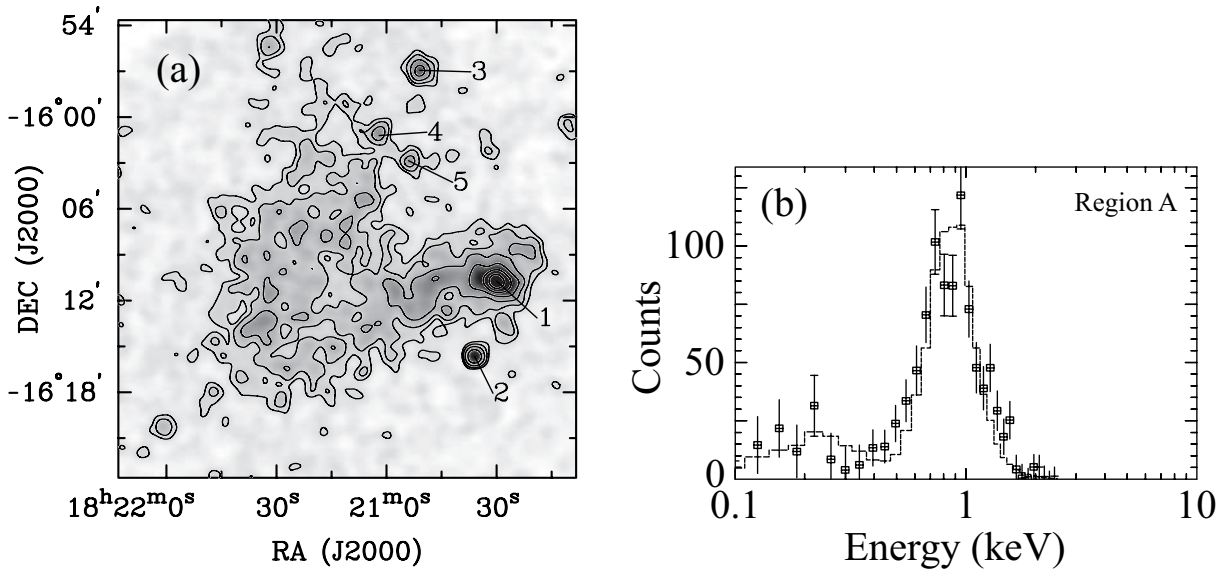

Figure 4.22: (a) ROSAT/PSPC image of M 17 smoothed with a Gaussian kernel of $\sigma = 20''$. (b) ROSAT/PSPC spectrum of a part of the diffuse emission in M 17. The data and best-fit model are shown in squares and dashed line (Dunne et al., 2003).

enough to compare to the theoretical works. It is often ambiguous whether the observed diffuse emission is from wind-blown bubbles or from supernovae, which give rise to diffuse emission with a similar X-ray spectral hardness and luminosity in a similar spatial scale. The largest uncertainty stems from the lack of spectral analysis based on line diagnostics in a spatially-resolved manner.

Resolving emission lines is crucial to examine whether the spectrum is thermal and to determine the temperature and the chemical composition of the plasma. For example, the intensity ratio of Kα lines between O VII and O VIII and that between Ne IX and Ne X are steep functions of the plasma temperature at 1–10 MK (Tucker & Gould, 1966). In between the O and Ne Kα complex, Fe L series lines dominate the spectrum. The metallicity of these elements is one of the factors to determine the X-ray luminosity expected from a wind-blown bubble (Chu et al., 1995). The anomaly in the O and Fe abundance ratio can be used to discriminate different types of supernovae (Tsujimoto et al., 1995; Thielemann et al., 1996; Nomoto et al., 1997) if the emission is of a supernova origin. The previous studies using ROSAT and Chandra were incapable of resolving these lines, limiting their ability to diagnose the plasma emission.

The XIS onboard Suzaku has a good spectral resolution, a low background, and a large effective area, which are particularly suited for spectroscopy of extended X-ray emission. The capability to resolve key elements with sufficient statistical significance has been il-

lustrated by several initial studies on extended emission in H II regions (Hamaguchi et al., 2007; Tsujimoto et al., 2007). Hamaguchi et al. (2007) resolved various emission lines from the diffuse emission in the Carina Nebula. Based on the low nitrogen-to-oxygen ratio and the spatial variation of the Fe and Si abundances, they suggested that the diffuse emission originates not from wind-blown bubbles but from one or multiple old supernova remnant(s).

4.3.2 Observations & Reduction

Table 4.11: Observation log around the M17 region.

Obs. Name	Start Date	ObsID	Aim point (J2000.0)		$t_{\rm exp}$* (ks)	
			RA	Dec	XIS	HXD†
M 17 West	2006-03-11	501003010	$18^{\rm h}20^{\rm m}49^{\rm s}$	$-16°10'58''$	110	86
M 17 East	2007-10-04	502052010	$18^{\rm h}21^{\rm m}33^{\rm s}$	$-16°12'22''$	121	94
M 17 BG	2007-10-07	502053010	$18^{\rm h}22^{\rm m}34^{\rm s}$	$-15°34'49''$	75	63

* Exposure time after good time interval filtering described in the text.

† Before the dead time correction.

Suzaku made two on-source observations of the M 17 region. Since the diffuse emission is prevailing over the entire FOV, an off-source region $\sim 35'$ apart from the OB association was also observed to construct the background spectra. The layout of the three observed fields are shown in figure 4.23. We discarded data taken during the elevation angles below 4° from the Earth rim and 10° from the day Earth rim. We used the data processed with the pipe-line process version 2.3. The observation log is shown in table 4.11.

4.3.3 Band-limited Images & Source list

Figure 4.24 shows the mosaic image of M 17 East and West region in the (a) 0.5–2.0 keV and (b) 2.0–5.0 keV bands. The two images are strikingly different. In the hard-band, the image is dominated by the OB association consisting of hundreds of point sources (Broos et al., 2007). We also see excess emission from a group of protostars in M 17 North (Wilson et al., 1979; Henning et al., 1998; Broos et al., 2007), OI 352 (Ogura & Ishida, 1976; White et al., 1994), and three point sources in the M 17 East field. We designate the three point sources Suzaku J182132–1610.4, Suzaku J182132–1613.4, and Suzaku J182140–1604.1. In the soft band, The diffuse emission is clearly seen as was claimed by Dunne et al. (2003) and Townsley et al. (2003).

We tuned the sky coordinates using Suzaku J182132–1610.4 Suzaku J182132–1613.4 and

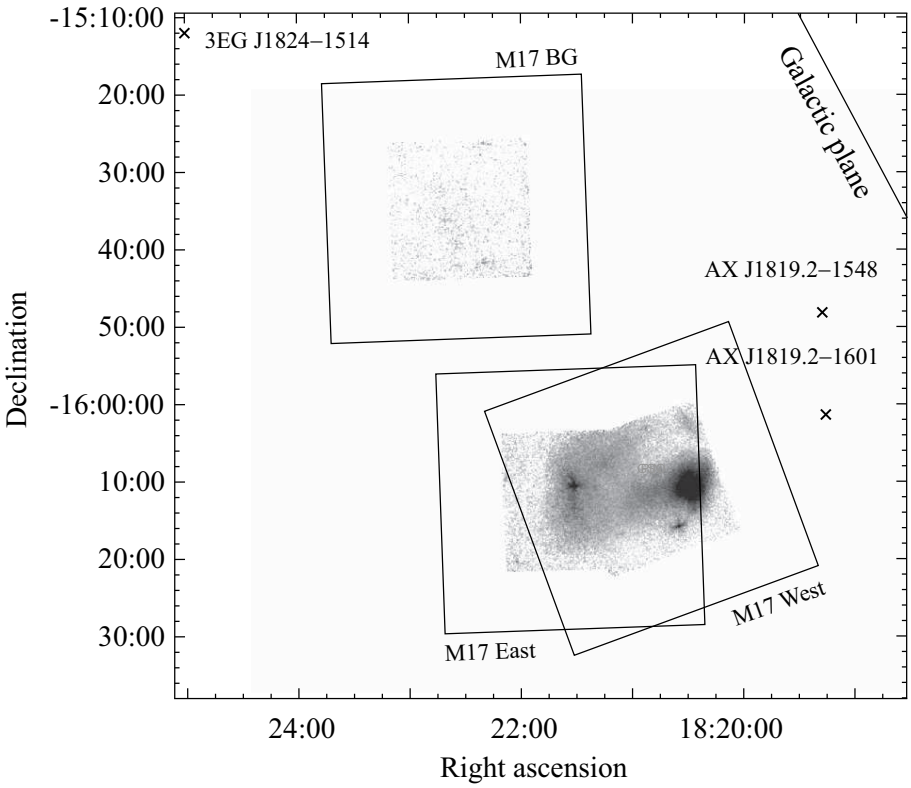

Figure 4.23: Mosaic XIS image of the three Suzaku observations in the M 17 region. The FOVs of PIN are displayed with solid lines, while the soft-band XIS images are shown in gray scale. Point sources in the INTEGRAL general reference catalog (http://isdc.unige.ch/Data/cat/29/catalog.html) are shown with crosses.

OI 352. Suzaku J182140–1604.1 was not used because the image is smeared near the FOV edge. The three sources are also detected in the Chandra/ACIS observation (ObsID = 7391). We shifted the Suzaku coordinates so that the positions match with those of the Chandra observations. Since no bright point source are detected in the background observation, we did not perform the astrometry tuning for M 17 BG.

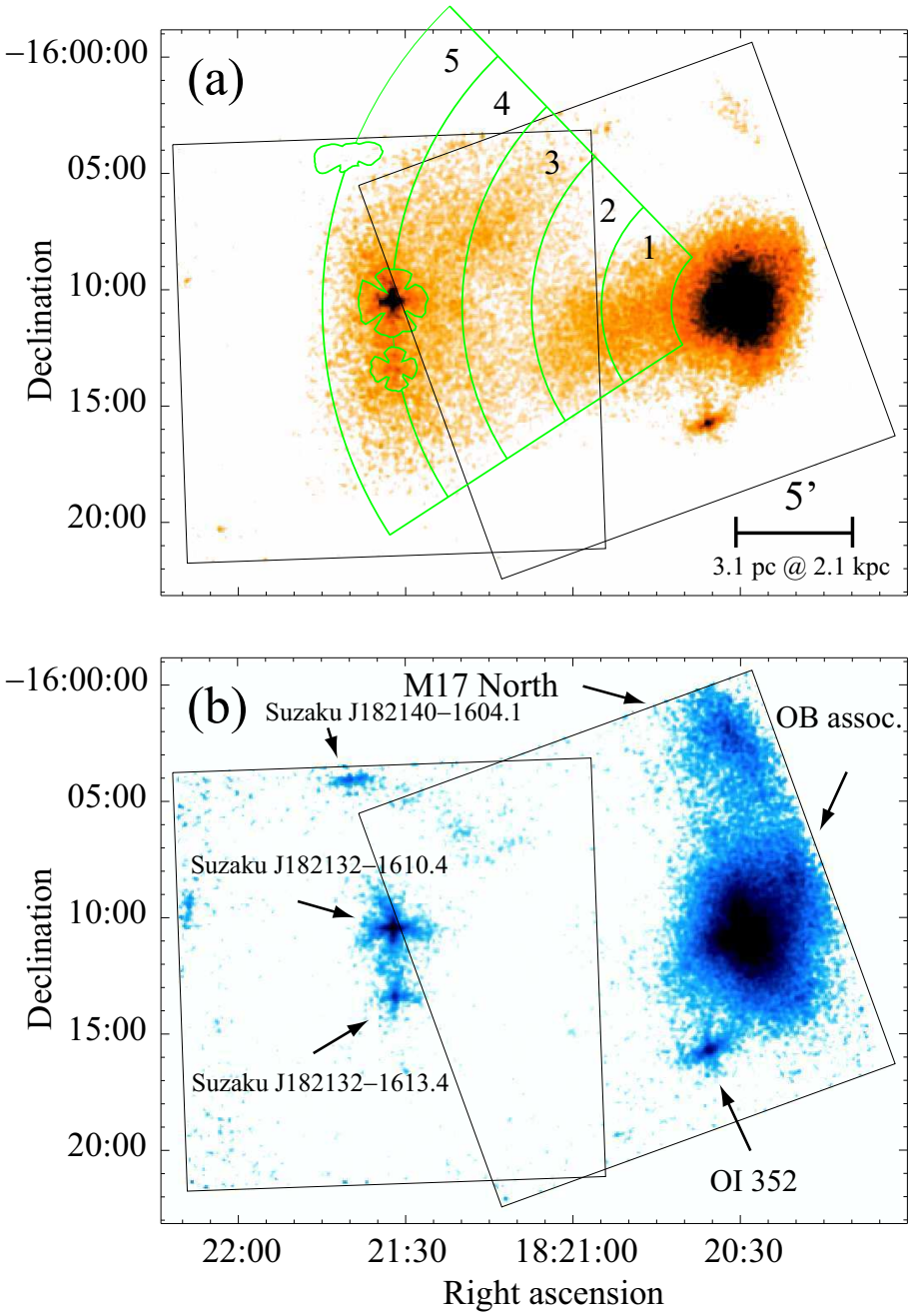

Figure 4.24: XIS images of the on-source observations in the (a) 0.5–2.0 keV and (b) 2.0–5.0 keV bands. Both images are smoothed with a Gaussian kernel of 12″ after the NXB is subtracted. The effects of exposure, vignetting, and contamination on the OBF are corrected. The coordinates are reregistered using the point sources referring the Chandra frame. The FOVs and the source regions of diffuse emission are shown in white and green solid lines.

Table 4.12: Point source list of the M 17 region

Source ID	Position (J2000.)		Nature	Reference
	RA	Dec		
OB association	$18^{h}20^{m}30^{s}$	$-16°11'$		
OI 352	$18^{h}20^{m}36^{s}$	$-16°15'42''$	O8 V	1, 2
M 17 North	$18^{h}20^{m}30^{s}$	$-16°03'$	protostars	3, 4, 5
Suzaku J182132–1610.4	$18^{h}21^{m}32^{s}$	$-16°10'28''$		
Suzaku J182132–1613.4	$18^{h}21^{m}32^{s}$	$-16°13'24''$		
Suzaku J182140–1604.1	$18^{h}21^{m}40^{s}$	$-16°04'10''$		

References. — (1) Ogura & Ishida (1976) (2) White et al. (1994) (3) Wilson et al. (1979) (4) Henning et al. (1998) (5) Broos et al. (2007)

4.3.4 Discrete sources

Timing Analysis

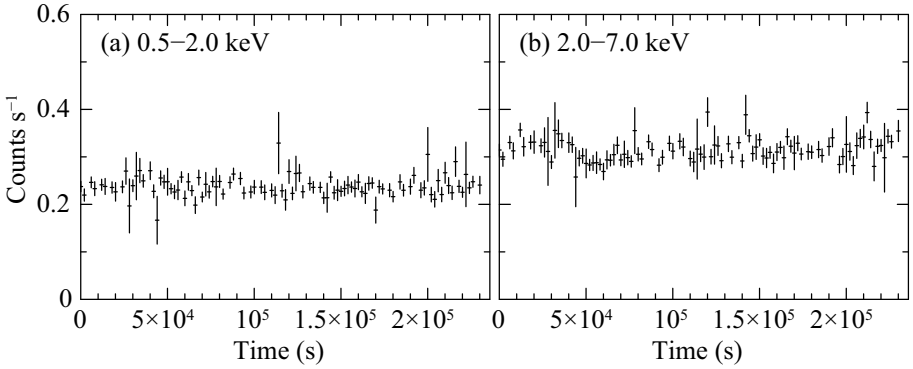

Figure 4.25: XIS light curves of the OB association in the (a) 0.5–2.0 keV and (b) 2.0–7.0 keV bands. The events of four chips are summed. The background is not subtracted.

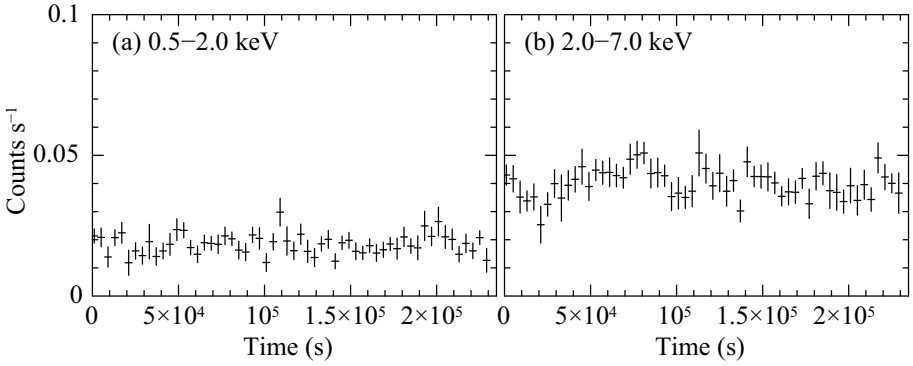

Figure 4.26: XIS light curves of M 17 North. The XIS 1 events are not included.

We extracted source photons of point sources (Suzaku J182132–1610.4, Suzaku J182132–1613.4, Suzaku J182140–1604.1, and OI 352) from polygonal regions along the PSF as is described in §3.1.1. The OB association photons were extracted from a circular region with a radius of 1′ around the cluster center at (RA, Dec) = ($18^{\rm h}20^{\rm m}29.9^{\rm s}$, $-16°10\ '45''$) in the equinox J2000.0 (Chini et al., 1980). We collected M 17 North photons from an elliptical region with semi-minor and semi-major axes of 1.′5 and 2.′5, respectively. The corresponding background photons were accumulated from nearby regions individually.

The XIS light curves of the discrete sources are shown in figures 4.25–4.30. Among the six sources, only Suzaku J182132–1610.4 showed significant flux variation. Soon after the

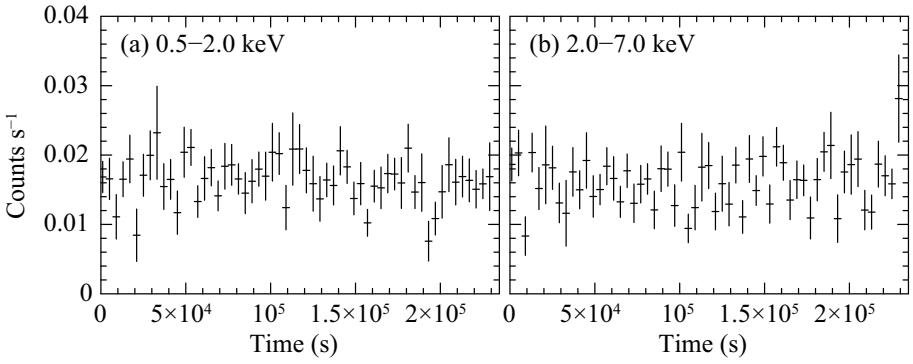

Figure 4.27: XIS light curves of OI 352.

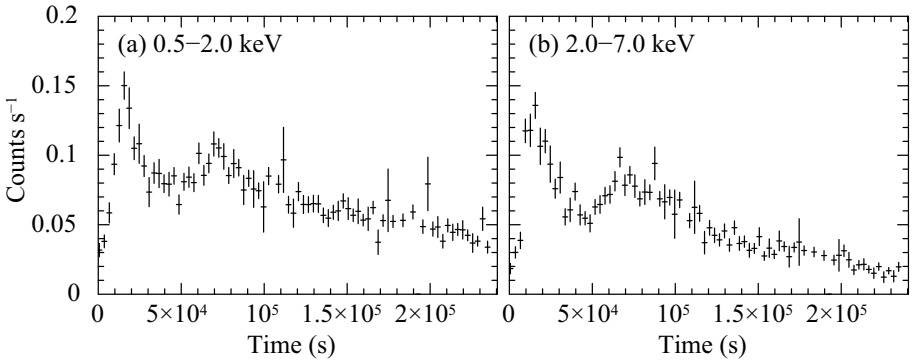

Figure 4.28: XIS light curves of Suzaku J182132–1610.4 The events of three chips are summed.

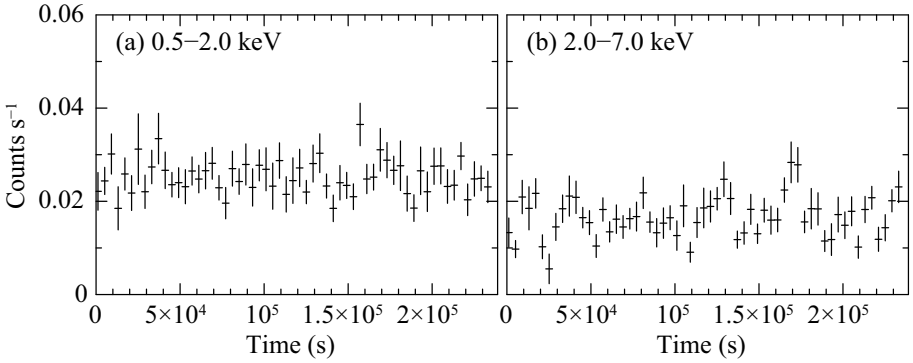

Figure 4.29: XIS light curves of Suzaku J182132–1613.4. Symbols follow figure 4.28.

observation start, a flare was detected in both the soft and hard bands. In the decay phase, a weaker flare was also detected. The source was still in the decay phase at the end of the

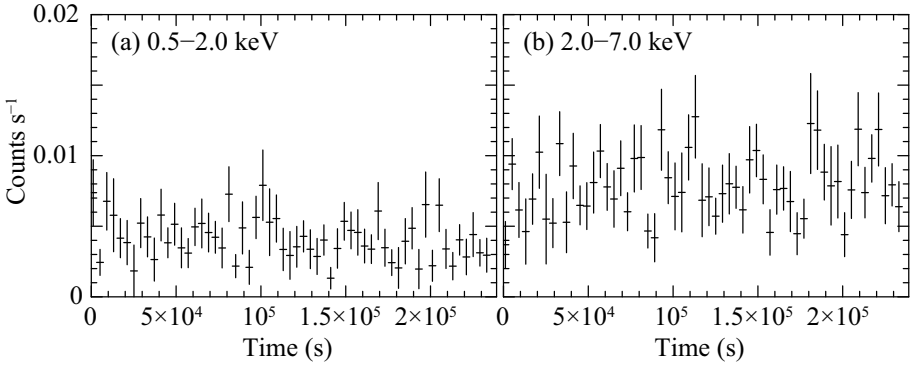

Figure 4.30: XIS light curves of Suzaku J182140–1604.1. Symbols follow figure 4.28.

observation.

Spectral Analysis

The spectra of the discrete sources are shown in figures 4.31 and 4.32. The summed FI and BI spectra were fitted simultaneously, but only the summed FI data and the best-fit model are shown for simplicity. The spectra of the three sources in the M 17 West observation are characterized by a hard continuum and Kα lines from He- and H-like ions of Mg, Si, S, Ar, Ca, and Fe. On the other hand, the three point sources in the M 17 East observation show only Fe emission line. The spectra were first fitted with a single thin-thermal plasma model (APEC; Smith et al. 2001) attenuated by interstellar extinction (Morrison & McCammon, 1983). If the model is rejected, we added an additional plasma component of a different temperature. The elemental abundances with distinctive emission lines were left free. The best-fit parameters are summarized in table 4.13.

Since the three point sources in M 17 East region show only Fe emission lines, we assumed that all elemental abundances relative to the solar values are the same. All spectra were well reproduced with a single temperature plasma model modified by interstellar photo-electric absorption. The spectra and the best-fit parameters are shown in table 4.14 and figure 4.32.

Table 4.13: Best-fit APEC parameters for the discrete spectra.

Pars.	Units	OI 352	M 17 North	OB association
$N_{\rm H}{}^{*}$	(10^{22} cm^{-2})	1.7 (1.4–2.0)	2.4 (2.1–2.7)	1.3 (1.2–1.4)
$k_{\rm B}T_{\rm high}{}^{*\dagger}$	(keV)	3.8 (3.1–4.7)	2.7 (2.4–3.2)	4.0 (3.9–4.1)
$k_{\rm B}T_{\rm low}{}^{*\dagger}$	(keV)	0.56 (0.47–0.65)	...	0.59 (0.56–0.62)
$Z_{\rm Ne}{}^{*}$	(solar)	0.3	0.3	0.51 (0.34–0.71)
$Z_{\rm Mg}{}^{*}$	(solar)	0.49 (0.24–0.87)	0.3	0.51 (0.38–0.65)
$Z_{\rm Si}{}^{*}$	(solar)	0.30 (0.16–0.58)	0.3	0.53 (0.39–0.71)
$Z_{\rm S}{}^{*}$	(solar)	1.07 (0.58–1.72)	0.3	1.17 (0.98–1.38)
$Z_{\rm Ar}{}^{*}$	(solar)	0.3	1.67 (0.72–3.00)	1.44 (1.00–1.90)
$Z_{\rm Ca}{}^{*}$	(solar)	0.3	0.3	0.46 (0.01–0.90)
$Z_{\rm Fe}{}^{*}$	(solar)	0.33 (0.19–0.48)	0.36 (0.22–0.50)	0.28 (0.25–0.31)
$F_{\rm X}{}^{*\ddagger}$	(10^{-13} erg s^{-1} cm^{-2})	3.9 (3.8–4.0)	7.4 (7.1–7.7)	58.3 (57.8–58.8)
$L_{\rm X}{}^{\S}$	(10^{32} erg s^{-1})	5.5	8.4	52
χ^2/d.o.f.	.....	100.2/134	66.4/76	473.3/405

* The uncertainties in the parentheses are the 90% confidence range. Fixed values are shown without ranges.

† The plasma temperatures for the higher and lower temperature components. Only the higher temperature value is given for M 17 North, which is fitted by a single temperature model.

‡ The X-ray flux in the 1.0–8.0 keV band.

§ The absorption-corrected X-ray luminosity in the 1.0–8.0 keV band. A distance of 2.1 kpc is assumed.

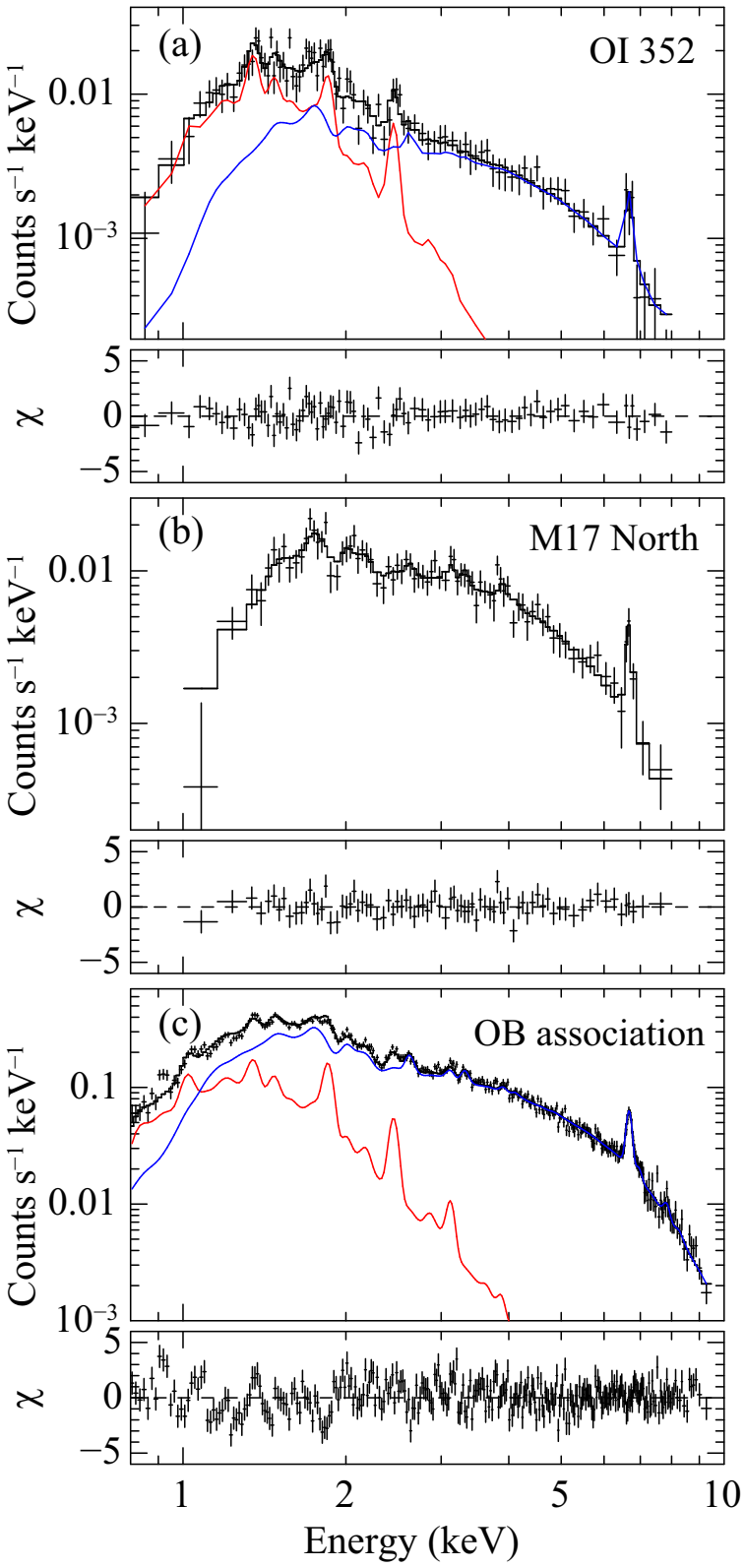

Figure 4.31: Background-subtracted spectra of (a) OI 352, (b) M 17 North, and (c) the OB association. Red and blue lines show two components separately. We show the summed FI data in crosses and the best-fit models in solid lines. Lower panels show the residual between the data and model.

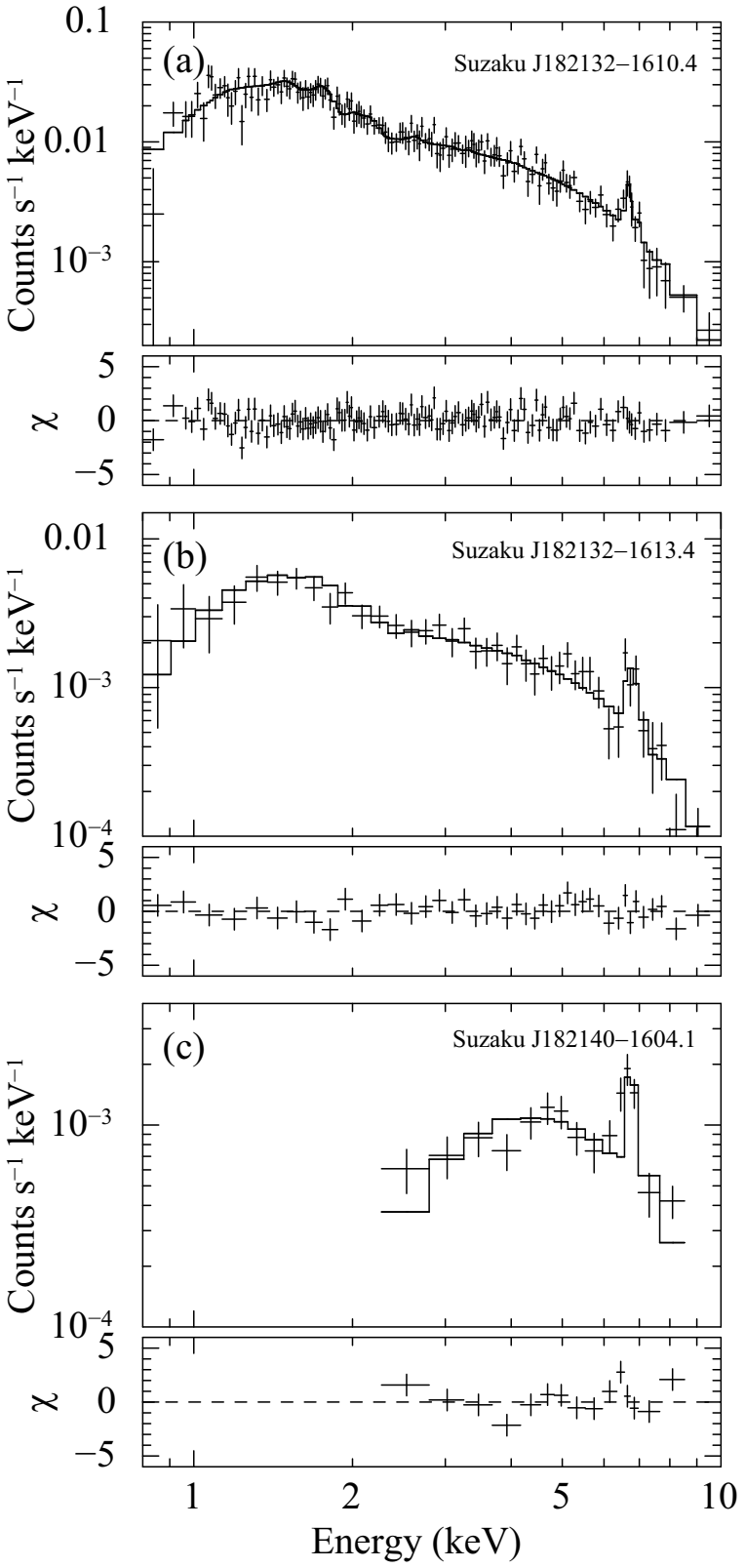

Figure 4.32: Background-subtracted spectra of (a) Suzaku J182132–1610.4, (b) Suzaku J182132–1613.4, and (c) Suzaku J182140–1604.1.

Table 4.14: Best-fit parameters of three point sources in the M 17 EAST region

Pars.	Unit	Suzaku J182132–1610.4	Suzaku J182132–1613.4	Suzaku J182140–1604.1
$N_{\rm H}$	(10^{21} cm^{-2})	3.3 ± 0.6	$4.6^{+2.0}_{-1.5}$	91^{+29}_{-24}
$k_{\rm B}T$	(keV)	6.1 ± 0.7	$9.5^{+3.5}_{-2.7}$	$12.7^{+6.7}_{-3.3}$
Z	(solar)	0.3 ± 0.1	$0.9^{+0.5}_{-0.4}$	$2.9^{+4.1}_{-1.5}$
$F_{\rm X}$	(10^{-13} erg s cm^{-2})	9.5 ± 0.3	2.3 ± 0.1	3.4 ± 0.2
$L_{\rm X}{}^*$	(10^{32} erg s^{-1})	55	1.3	3.8
χ^2/d.o.f.		181.6/209	72.4/81	45.8/25

* The absorption-corrected X-ray luminosity in the 1.0–8.0 keV band. A distance of 2.1 kpc is assumed.

4.3.5 Diffuse sources

As was claimed by Dunne et al. (2003), the surface brightness is the highest near the cluster core and spreads out westward in a fan-like form, indicating that the emission originates from the cluster core. We therefore extracted source photons from five concentric pie-shaped regions with radii of 3′–6′, 6′–9′, 9′–12′, 12′–15′, and 15′–18′, centered at the cluster center. We excluded the regions around the three point sources in M 17 East field. The background events were accumulated from the M 17 BG field in the same detector coordinate with the source regions. M 17 West observation was performed ~ 1.5 yr earlier than the M 17BG observation. Since the amount of the OBF contaminant changed significantly during this interval (figure 3.13), we processed raw spectra in the following way to compensate for the difference in the quantum efficiency: (1) We subtracted the NXB provided by the XIS team. Since the NXB count rates anti-correlate with COR2, we compiled night Earth observations so that the COR2 distribution becomes the same with that of the source observation. (2) The vignetting including the spatial non-uniformity of the OBF contaminant was corrected by multiplying the effective area ratio between the source and the background regions for each energy bin of the background spectra. On the other hand, for M 17 East field observed just before the M 17 BG observation, we simply subtracted the background photons from source photons.

Although we collected photons avoiding the point source regions, spill-over photons may contaminate the diffuse emission spectra. Using `xissim`, we estimate the spill-over fraction from the point sources to the diffuse source regions and subtracted them from the diffuse emission spectra. For regions 2–4, we summed the events from M 17 West and East fields.

The resultant spectra were fitted with an APEC model attenuated by interstellar extinction. The best-fit model parameters and spectra are shown in figure 4.33 and table 4.15.

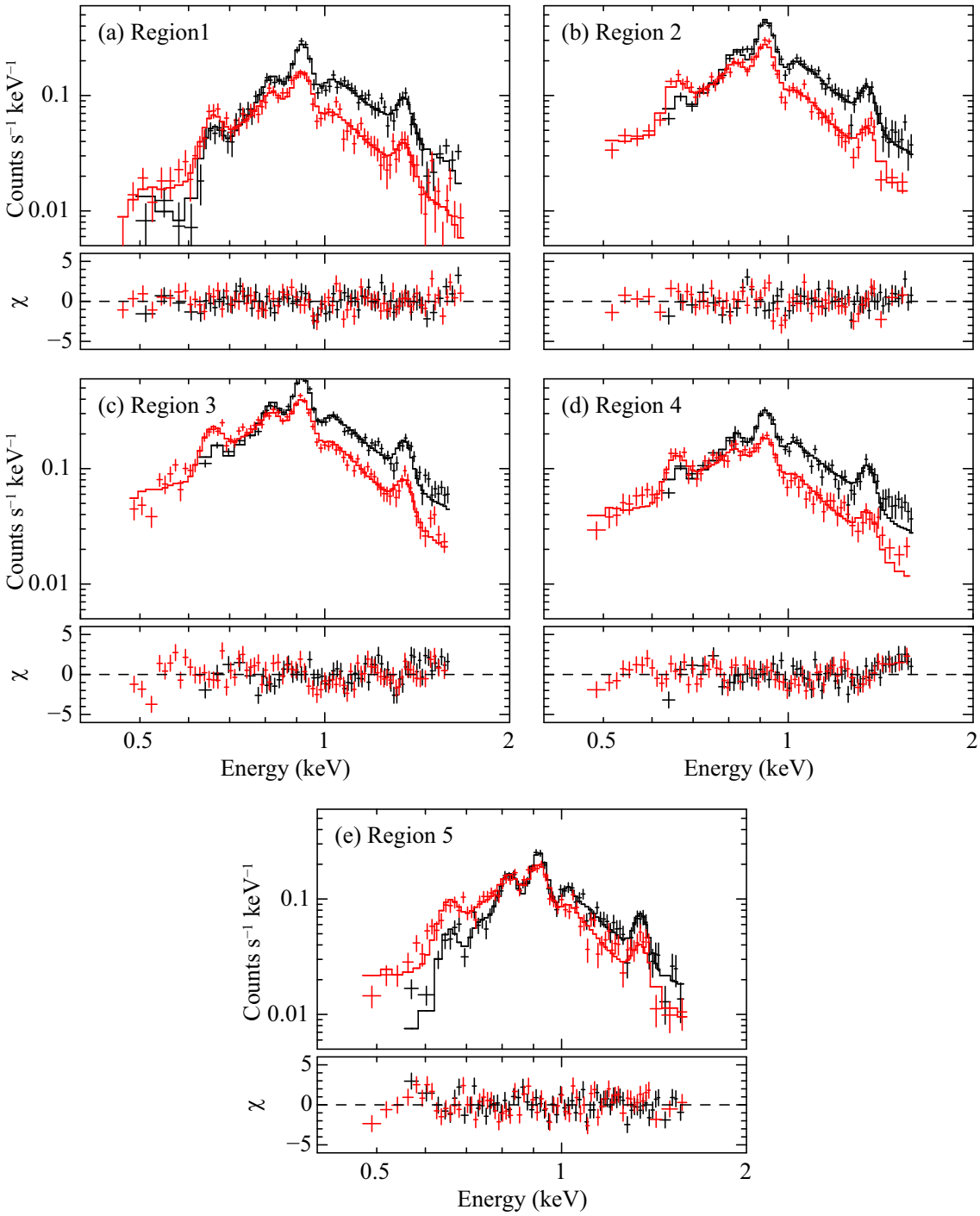

Figure 4.33: Background-subtracted spectra of diffuse emission in the M 17 East region in the 0.4–2.0 keV band. Lower panels show the residual between the data and the best-fit model. The summed FI and BI spectra are shown in black and red.

Table 4.15: Best-fit parameters of the APEC model for the diffuse emission in the M 17 West field.*

Par.	Unit	Region 1	Region 2	Region 3	Region 4	Region 5
$N_{\rm H}$	(10^{21} cm^{-2})	5.3 ± 0.3	4.4 ± 0.3	4.1 ± 0.2	4.0 ± 0.2	4.0 ± 0.2
$k_{\rm B}T$	(keV)	0.23 ± 0.01	0.23 ± 0.01	0.23 ± 0.01	0.24 ± 0.01	0.25 ± 0.01
$Z_{\rm O}$	(solar)	0.04 ± 0.01	0.03 ± 0.01	0.03 ± 0.01	0.06 ± 0.01	0.10 ± 0.01
$Z_{\rm Ne}$	(solar)	0.10 ± 0.01	0.09 ± 0.01	0.08 ± 0.01	0.14 ± 0.01	0.20 ± 0.02
$Z_{\rm Mg}$	(solar)	0.09 ± 0.01	0.09 ± 0.01	0.07 ± 0.01	0.11 ± 0.02	0.17 ± 0.02
$Z_{\rm Fe}$	(solar)	0.05 ± 0.01	0.05 ± 0.01	0.05 ± 0.01	0.07 ± 0.01	0.12 ± 0.01
$S_{\rm X}$†	(10^{-14} erg s^{-1} cm^{-2} arcmin^{-2})	2.34 ± 0.05	1.77 ± 0.03	1.79 ± 0.03	2.00 ± 0.04	1.60 ± 0.05

* The uncertainties indicate the 90% confidence range.

† X-ray surface brightness in the 0.5–2.0 keV band.

4.3.6 HXD-PIN Analysis

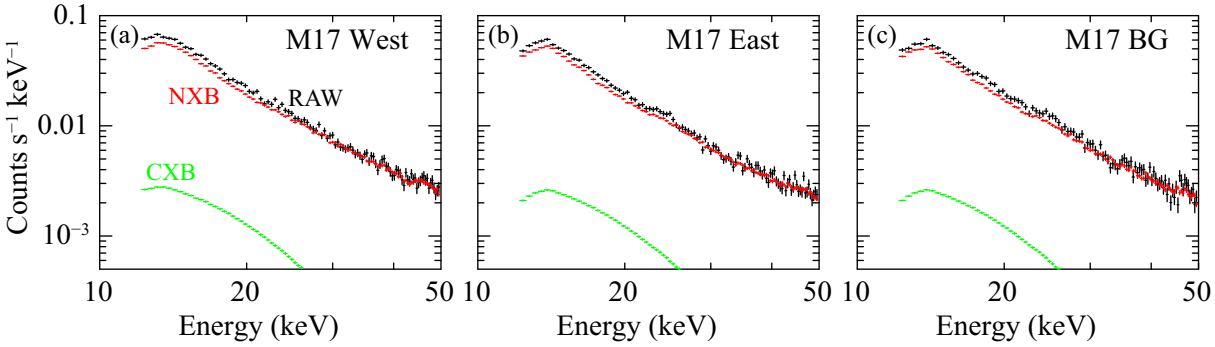

Figure 4.34: PIN spectra of the M 17 region observations. The raw spectra, reconstructed NXB spectra, and estimated CXB spectra are shown in black, red, green respectively.

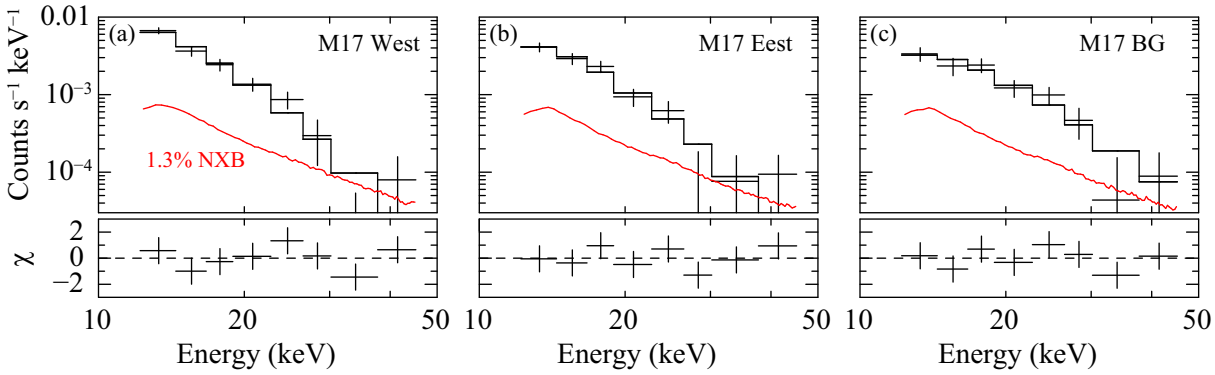

Figure 4.35: Background-subtracted PIN spectra of the M 17 regions. Both the NXB and CXB are subtracted in data shown with crosses. Solid black lines show the best-fit power-law model. The NXB reproducibility is shown in red lines. Lower panels show the residual between the data and the best-fit model.

We used the PIN data processed with the pipeline processing ver 2.0. In this process, data are discarded during the elevation angles below 5° and COR less than 6 GV. Slightly tighter screening criteria yield shorter net exposures for PIN than XIS (table 4.11). We used the time-dependent NXB model constructed as a function of PINUD provided by the HXD team. We also corrected the source exposure for the instrumental dead time, which reduced exposure time by $\sim 7\%$.

The raw spectra of each observation are shown in figure 4.34 overlaid with simulated cosmic X-ray background (CXB) and NXB spectra. CXB spectra were made using the model

by Boldt (1987) and Gruber et al. (1999) in the same manner as Reeves et al. (2007). After subtracting the CXB and NXB, we see excess counts in the $\sim$ 13–30 keV band above the current background uncertainty (figure 4.35). We fitted each spectrum with simple power-law, which yielded acceptable results (table 4.16).

Table 4.16: Best-fit parameters of PIN spectra of the M 17 regions

Obs. Name	Γ	$F_{\rm X}{}^{*}$	$L_{\rm X}{}^{\dagger}$	χ^2/d.o.f.
M 17 West	$3.3^{+0.6}_{-0.5}$	5.1 ± 0.5	2.7	5.7/6
M 17 East	$3.0^{+0.7}_{-0.6}$	4.2 ± 0.5	2.2	4.4/6
M 17 BG	$1.9^{+0.7}_{-0.6}$	5.5 ± 0.9	2.9	4.4/6

* The X-ray flux in the 15–30 keV band in the unit of 10^{-12} erg s^{-1} cm^{-2}. The source is assumed to be at the HXD nominal position.

† The X-ray luminosity in the 15–30 keV band in the unit of 10^{33} erg s^{-1}. A distance of 2.1 kpc is assumed.

4.4 Arches Cluster

4.4.1 Objectives

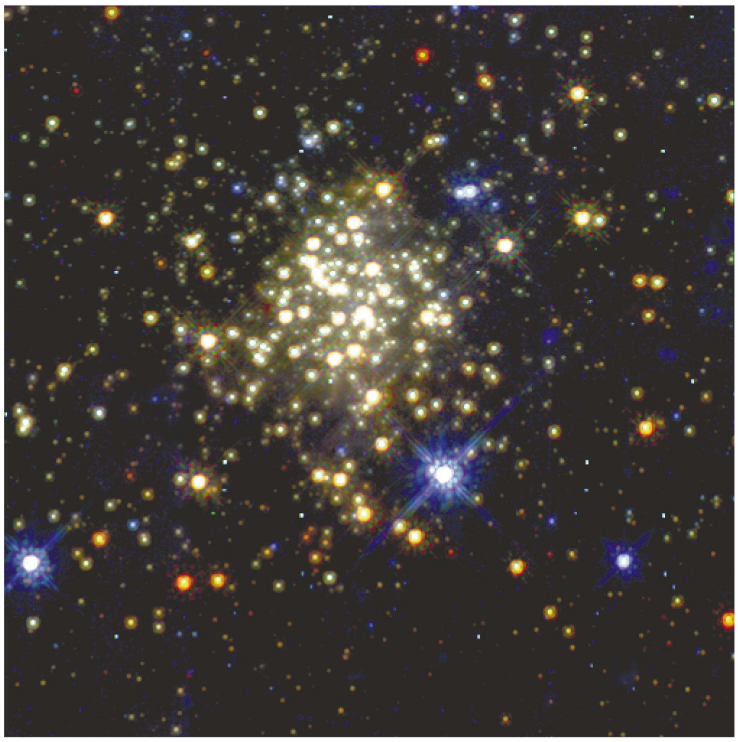

Figure 4.36: HST image of the Arches cluster (Figer et al., 1999b). Red, green, and blue scales show the flux in F205W, F160W, and F110W, respectively.

The central ~ 200 pc of our Galaxy is particularly rich in curious spatial and spectral features. One of the features distinctively seen in the Galactic center region is the diffuse iron Kα line emission at ~ 6.4 keV (Koyama et al., 1996). The line originates from neutral or low-ionized iron (hereafter quoted as Fe I), but its ionizing mechanism is not yet understood. Two major ideas have been developed. One is fluorescence from photo-ionized iron (Sunyaev et al., 1993; Koyama et al., 1996; Revnivtsev et al., 2004). The X-ray spectrum from the Sagittarius B2 cloud, which is characterized by the strong ~ 6.4 keV emission line and the ~ 7.1 keV iron K edge, is best accountable by this model (Koyama et al., 1996; Murakami et al., 2000). Another idea is that iron is ionized by accelerated electrons (Yusef-Zadeh et al., 2002b; Predehl et al., 2003; Wang et al., 2006).

The distribution of the diffuse 6.4 keV emission is highly asymmetric around the Galactic center with a bias in the north-east direction (Koyama et al., 1996, 2007b) and appears

filamentary (Park et al., 2004). Of particular interest is the 6.4 keV emission associated with the Arches cluster, which is one of the richest and the most densely packed massive star clusters in our Galaxy.

The Arches cluster has a total mass of $\sim 10^4\ M_\odot$, a compact size with a diameter of $\sim 15''$ (~ 0.6 pc at an assumed distance of 8.5 kpc), a stellar mass density of $\sim 3 \times 10^5\ M_\odot\ \mathrm{pc}^{-3}$, and an estimated age of 2–4.5 Myr (Nagata et al., 1995; Cotera et al., 1996; Serabyn et al., 1998; Figer et al., 1999b; Blum et al., 2001; Yang et al., 2002; Stolte et al., 2002; Figer et al., 2002; Figer, 2005). It contains $\sim 5\%$ of all the known Wolf-Rayet stars in our Galaxy (Figer, 2005), which are characterized by a large mass loss rate reaching $\sim 10^{-4}\ M_\odot\ \mathrm{yr}^{-1}$ (Lang et al., 2001, 2005). The level of high mass star-forming activity of the Arches cluster, which can be measured by the number of O stars, is comparable only to NGC 3603 (Moffat, 1983), W49A (Conti & Blum, 2002; Alves & Homeier, 2003), and Westerlund 1 (Clark et al., 2005) in our Galaxy and R136 at the center of 30 Doradus (Campbell et al., 1992) in the Large Magellanic Cloud.

Yusef-Zadeh et al. (2002) first reported the detection of two point sources in addition to diffuse emission from this region using the Chandra X-ray Observatory (Weisskopf et al., 2002). The extended X-ray emission is elongated beyond the cluster boundary with a size of $\sim 60'' \times 90''$ and its spectrum can be fit with a thermal model with a temperature of ~ 5.7 keV in addition to a ~ 6.4 keV line (Yusef-Zadeh et al., 2002). Based on these claims, the hard diffuse emission is considered an example of the cluster wind plasma, which is a collection of interacting stellar winds from massive stars in a cluster (Cantó et al., 2000; Raga et al., 2001; Silich et al., 2004; Rockefeller et al., 2005). However, the poor spectrum of the extended emission does not allow a conclusion to be drawn about a thermal origin. Law & Yusef-Zadeh (2004) cautioned that the continuum emission can also be fit by a power-law, and can thus be explained by non-thermal emission. Recent results based on a longer exposure Chandra observation by Wang et al. (2006) indicated that the cluster wind is only seen at the cluster center, and the majority of the diffuse emission is composed of a strong 6.4 keV line and a power-law continuum emission of non-thermal origin.

In order to understand the nature of the X-ray emission in the Arches cluster and the diffuse 6.4 keV emission ubiquitous in, but exclusive to, the Galactic center region, hard-band X-ray spectroscopy with high signal-to-noise ratio (S/N) is obviously a key. The bandpass includes both thermal (Fe XXV Kα and Fe XXVI Kα at ~ 6.7 and ~ 7.0 keV) and fluorescent (Fe I Kα and Kβ at ~ 6.40 and ~ 7.05 keV) features as well as the iron K absorption edge feature at ~ 7.11 keV. The underlying power-law continuum, if it ever exists, is visible at energies $\gtrsim 8$ keV, where the thermal contribution plays a minor role. Moreover, the hard X-rays penetrate through the large attenuation of $A_V \sim 30$ mag common toward the Galactic center region (Morris & Serabyn, 1996).

Here, we present the results of a spectroscopic study of the hard emission in the Arches cluster using the Suzaku Observatory. The XIS onboard Suzaku provides high S/N spectra in the hard-band aided by the excellent spectroscopic performance of the CCDs and the large effective area of the X-ray optics. To compliment the moderate spatial resolution of Suzaku, we refer to the recent Chandra results by Wang et al. (2006) and results obtained by our own reduction of the same dataset.

4.4.2 Observations & Reduction

Four observations of the Galactic center region were conducted using Suzaku (table 4.17). The aim points and roll angles among four observations are almost identical. The events were removed when they were taken during the elevation angles below 5°, the day earth elevation angles below 10°, and the SAA passages. The net exposure after this filtering is ~ 220 ks in total. For the first and second observations, we corrected for the CTI and fine-tuned the energy gain across the chips assuming that the center energy of Fe and S Kα lines in the diffuse spectrum is spatially uniform. These calibration processes were performed using the same dataset with the presented analysis. Resultantly, the systematic energy uncertainty of XIS is as low as $\sim +3/-6$ eV at 6 keV. The details of the calibration of the Galactic center datasets are described in Koyama et al. (2007b). The third and fourth observation data (ObsID=100048010 and 102013010) were processed with ver. 2.3 pipeline software.

Table 4.17: Observation log of the Arches cluster.

Start Date	ObsID	R. A.	Decl.	$t_{\rm exp}$*
		(J2000.0)		(ks)
2005-09-23	100027010	$17^{\rm h}46^{\rm m}02^{\rm s}$	$-28°55'32''$	48
2005-09-30	100037040	$17^{\rm h}46^{\rm m}02^{\rm s}$	$-28°55'32''$	46
2006-09-08	100048010	$17^{\rm h}46^{\rm m}03^{\rm s}$	$-28°55'36''$	69
2007-09-03	102013010	$17^{\rm h}46^{\rm m}03^{\rm s}$	$-28°55'39''$	57

* Exposure time after good time interval filtering described in the text.

4.4.3 Band-limited Images & Source list

Figure 4.38 shows the band-limited XIS images in the (a) 6.3–6.5, (b) 6.6–6.8, and (c) 7.5–10.0 keV bands. The former two bands contain Kα emission lines from iron at low and high ionization stages, respectively. The 7.5–10.0 keV image complements the one below

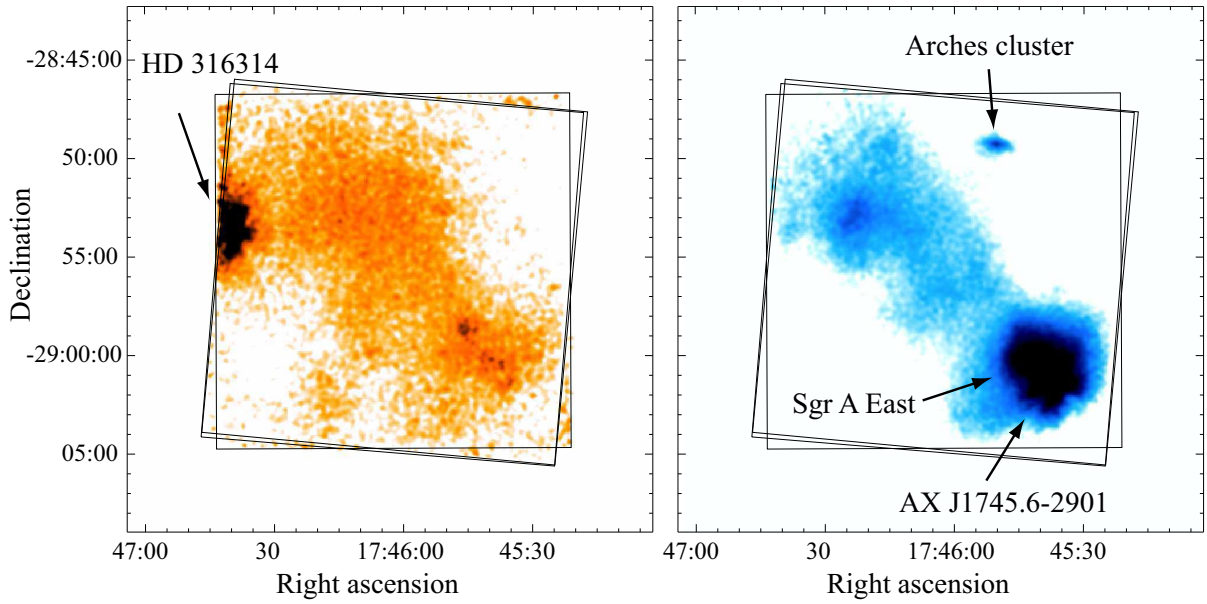

Figure 4.37: XIS images in the (a) 0.7–2.0 keV and (b) 2.0–5.0 keV bands. The making of the figures and symbols follow that of figure 4.24.

Table 4.18: Source list in the Sgr A East region

Source Name	Position (J2000.)	
	RA	Dec
Arches cluster	$17^{h}45^{m}50^{s}$	$-28°49'22''$

8.0 keV by Chandra; the effective area at 8 keV of Suzaku XIS is larger than that of Chandra ACIS by more than ten-fold. A significant excess is seen at the position of the Arches cluster in all bands, which is elevated from the diffuse emission at the north east of the Galactic center. Due to the limited spatial capability of Suzaku XIS, it is difficult to discriminate point sources from the underlying diffuse emission in the Arches cluster.

The 7.5–10.0 keV image (figure 4.38c) morphologically resembles the 6.4 keV image (figure 4.38a) more than the 6.7 keV image (Fig. 4.38b). In particular, both the 7.5–10.0 keV and the 6.4 keV images have a local excess centered at the radio arc bubble located at about (l, b)=(0.13°, –0.11°). The correlation between the 6.4 keV emission and the radio arc bubble was found by Rodríguez-Fernández et al. (2001). Also, the 6.7 keV image has the dominating peak at the Saggitarius A East, while the 6.4 keV and 7.5–10.0 keV images have extended emission across the field with a similar surface brightness.

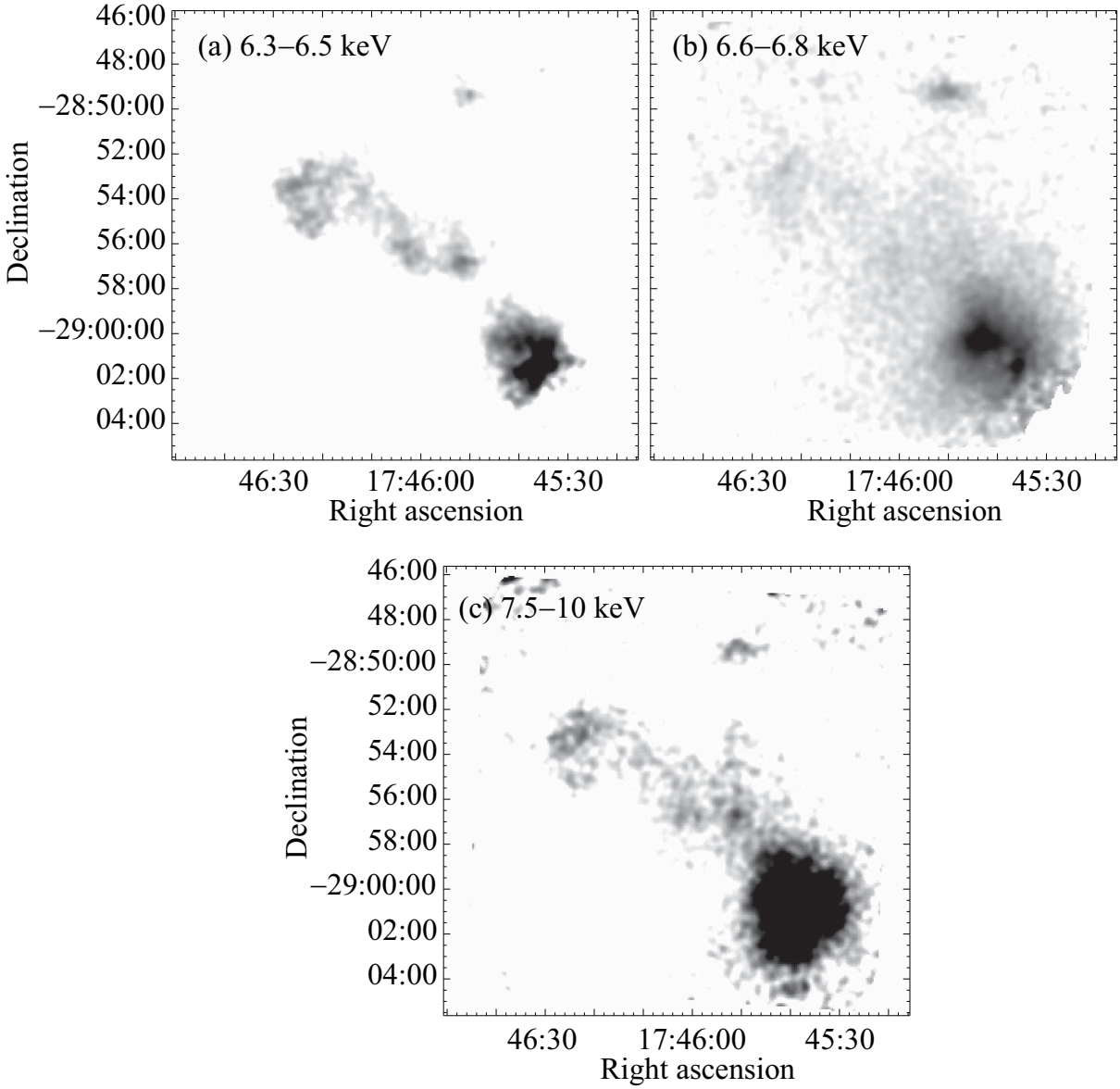

Figure 4.38: XIS images with a smoothing of $\sigma = 8''$ in (a) the 6.3–6.5 keV band, (b) the 6.6–6.8 keV band, and (c) 7.5–10.0 keV band. The NXB is subtraceted and the exposure correction is applied.

4.4.4 Spectral Analysis

The source photons are collected from a circle centered at the local intensity peak of the XIS image. The background are from a position devoid of intense diffuse emission and at a similar off-axis angle. We examined several position for the background and found that

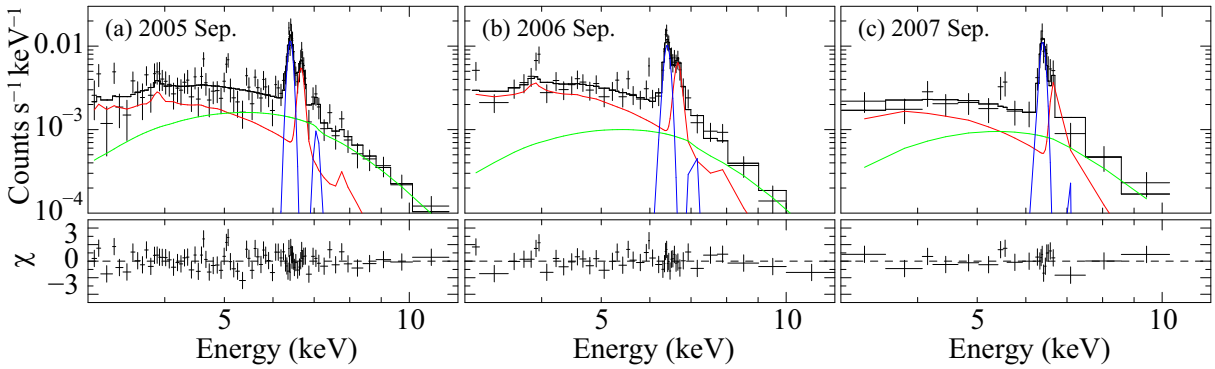

Figure 4.39: Background-subtracted spectra of the Arches cluster in 3–12 keV. The thermal, power-law, and Gaussian components are shown in red, green, and blue, respectively.

the spectrum above ~ 3 keV is intense to the background, On the other hand, the spectrum below ~ 3 keV is contaminated by inhomogeneous diffuse emission prevailing the Galactic center region, and hence is ignored hereafter. A radius of $1'.6$ is used for the background, while a smaller radius of $1'.4$ is used for the source region to increase the signal-to-noise ratio.

Figure 4.39 shows the background-subtracted spectra in each observation. The spectra shows intense emission lines in the 6.0–8.0 keV band over a hard continuum. The three most conspicuous lines are attributable to the Kα line from highly ionized iron (Fe XXV) at $\sim$6.7 keV, and Kα and Kβ lines from neutral or low-ionized iron (Fe I) at $\sim$6.4 and $\sim$7.1 keV, respectively. The existence of Fe XXV Kα in addition to Ca XIX Kα ($\sim$3.9 keV) and Ni XXVII Kα+ Fe XXV Kβ (7.8–7.9 keV) lines indicates a thermal plasma with a temperature of a few keV, while Fe I K lines and a hard continuum up to $\sim$12 keV suggest additional components.

The events of the first and second observations were summed, while the third and forth observations were treated separately. We first fitted the summed first and second spectrum with photo-electrically absorbed thin-thermal plasma (APEC; Smith et al. 2001) model to determine the plasma temperature ($k_{\rm B}T$) and the amount of interstellar extinction ($N_{\rm H}$).

The abundance relative to solar was derived separately for elements with prominent emission lines. Two Gaussian components were added to the model to account for the lines at ~ 6.4 and ~ 7.1 keV. Their line center and flux of the 7.1 keV were fixed to 1.103 and 0.113 times those of the 6.4 keV line. The widths of the lines were consistent with zero. The resultant best-fit model was marginally acceptable with the null hypothesis probability of the χ^2 value (P_{χ^2}) of 0.01. A significant residual above $\sim$7 keV obviously requires an additional component. We added a power-law component to reach an acceptable fit. An additional thermal component also yielded an acceptable fit, but the best-fit temperature of > 20 keV is unphysical. We therefore continued with the power-law component.

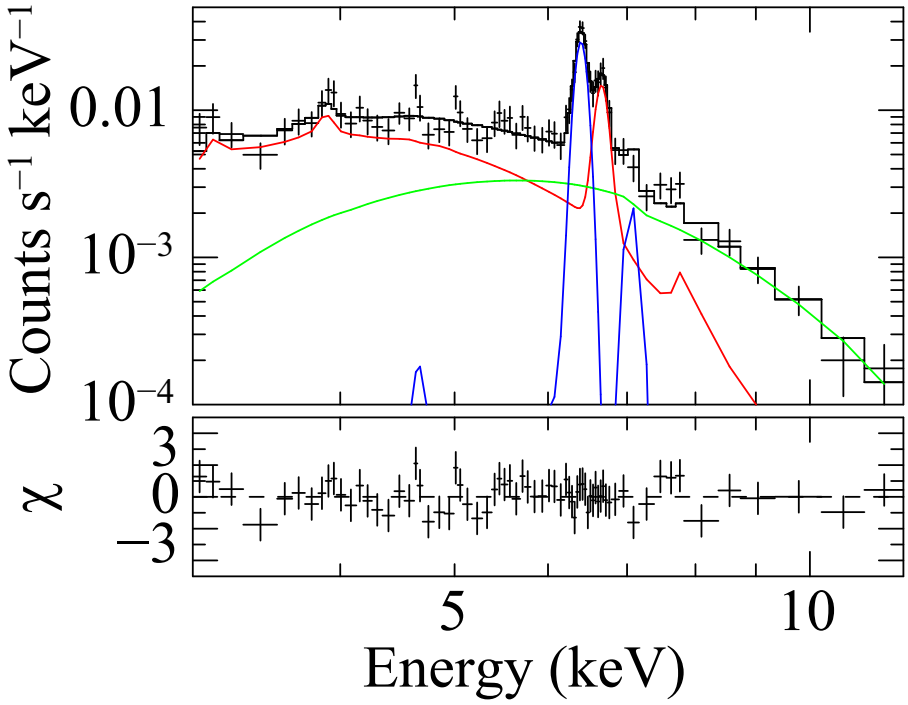

Figure 4.40: XIS spectrum of the Arches cluster. Data from four observations are summed. Symbols follow figure 4.39

The final fit result (P_{χ^2} =0.28) is summarized in table 4.19. Here, we fixed the abundance to be solar for all the elements upon the confirmation that the best-fit value is consistent with solar. By separating the Fe I Kβ line at ∼7.05 keV, the Fe XXVI Kα line at ∼ 6.97 keV and the Fe K edge at ∼ 7.11 keV are found to be absent. The absence of the Fe XXVI line as well as the existence of the Fe XXV line contributes for a tight constraint of the plasma temperature. The $N_{\rm H}$ is common for all the components. The fitting results are shown in table 4.19.

For the third and fourth observations, we fixed $N_{\rm H}$, $k_{\rm B}T$, and Γ to the best-fit values derived above due to the limited photon statistics. The normalization of the thermal and power-law components and Gaussian line parameters were consistent with the first and second observations.

Finally, we summed all the events from four observations, and performed spectral analysis in the same way of the first and second observation data. We obtained more constrained parameters (table 4.19).

Table 4.19: Best-fit parameters for the Arches cluster

Observation	Absorption	Thermal		Power-law		Gaussian	
	$N_{\rm H}$	$k_{\rm B}T$	$f_{\rm th}{}^{*}$	Γ	$f_{\rm PL}{}^{*}$	E	N
	(10^{23} cm^{-2})	(keV)	(erg s^{-1} cm^{-2})		(erg s^{-1} cm^{-2})	(eV)	(10^{-5} cm^{-2} s^{-1})
1st & 2nd	$1.4^{+0.5}_{-0.4}$	$2.2^{+1.8}_{-0.7}$	$5^{+8}_{-3}\times10^{-13}$	0.72 ± 0.7	$7^{+21}_{-5}\times10^{-13}$	6407^{+7}_{-5}	$2.1^{+0.4}_{-0.3}$
3rd	1.4 (fixed)	2.2 (fixed)	$8\pm2\times10^{-13}$	0.72 (fixed)	$5\pm2\times10^{-13}$	6408^{+14}_{-16}	2.6 ± 0.4
4th	1.4 (fixed)	2.2 (fixed)	$7\pm3\times10^{-13}$	0.72 (fixed)	$8\pm4\times10^{-13}$	6399^{+17}_{-23}	$2.7^{+0.5}_{-0.6}$
All merged	1.6 ± 0.4	$1.9^{+0.6}_{-0.4}$	$6^{+7}_{-3}\times10^{-13}$	$0.60^{+0.74}_{-0.31}$	$7^{+14}_{-4}\times10^{-13}$	6404^{+9}_{-8}	2.4 ± 0.3

* Values in the 3.0–10.0 keV band.

Chapter 5

Discussion

In this chapter, we discuss the nature and the X-ray production mechanisms of diffuse and discrete sources. In section 5.1, making use of the infrared data, we discuss the nature of the bright Suzaku X-ray source in the Galactic center to be a WR star. Section 5.2 is devoted for the interpretaion of the X-ray emission mechanisms of the discrete and diffuse sources in the Carina Nebula. In section 5.3, we speculate the nature of the newly detected three discrete sources. We also discuss the X-ray emission mechanisms of previously known three sources and the diffuse sources. We study the X-ray emission mechanisms of discrete and diffuse sources in the Arches cluster in section 5.4. The cross-regional study is presented in section 5.5.

Contents

5.1 A New Wolf-Rayet Star in the Galactic Center

5.1.1 Chandra and XMM-Newton Counterparts

Table 5.1: Observation log of the Sgr North region.

Start Date	Observatory	ObsID	R. A. (J2000.0)	Decl. (J2000.0)	$t_{\rm exp}$* (ks)	$\theta^{\dagger}$ (′)
2000-09-23	XMM-Newton	0112970201	$17^{\rm h}47^{\rm m}21^{\rm s}$	–28°09′02″	11	11.7
2000-10-27	Chandra	1036	$17^{\rm h}47^{\rm m}22^{\rm s}$	–28°11′36″	35	10.5
2001-07-16	Chandra	2271	$17^{\rm h}47^{\rm m}28^{\rm s}$	–28°16′29″	10	9.5
2001-07-16	Chandra	2274	$17^{\rm h}46^{\rm m}42^{\rm s}$	–28°10′23″	10	5.7
2001-07-16	Chandra	2285	$17^{\rm h}46^{\rm m}18^{\rm s}$	–28°20′23″	10	7.9
2003-03-12	XMM-Newton	0144220101	$17^{\rm h}47^{\rm m}23^{\rm s}$	–28°09′15″	34	10.4
2006-09-21	Suzaku	501040010	$17^{\rm h}46^{\rm m}46^{\rm s}$	–28°22′51″	70	7.4
2006-09-24	Suzaku	501040020	$17^{\rm h}46^{\rm m}46^{\rm s}$	–28°22′51″	50	7.4

* Exposure time after removing periods with high background level. The exposure times for the XMM-Newton observations refer to those obtained with the EPIC-pn camera.
† Angular distance of the source from the optical axis.

We retrieved the archived Chandra (Weisskopf et al., 2002) and XMM-Newton (Jansen et al., 2001) data to study the long-term behaviors of the source, and to locate its position more precisely using telescopes of smaller HPDs than that of Suzaku. Four Chandra observations using the Advanced CCD Imaging Spectrometer (ACIS: Garmire et al. 2003) and two XMM-Newton observations using the European Photon Imaging Camera (EPIC: Turner et al. 2001; Strüder et al. 2001), which is comprised of two MOS and a PN, were found to cover the Suzaku source (table 5.1).

Within the Suzaku positional uncertainty of 50″, we found only one Chandra source (CXOGC J174645.3–281546) in Muno et al. (2006b) and one XMM-Newton source

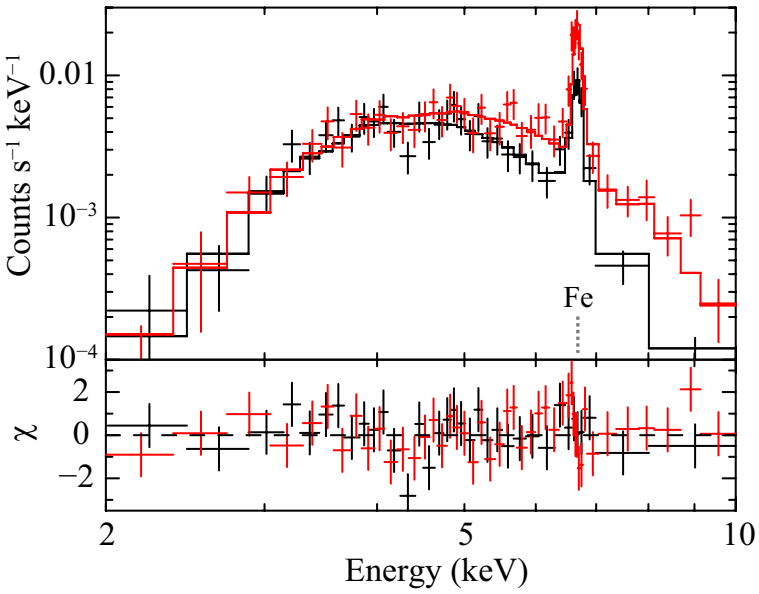

Figure 5.1: Background-subtracted EPIC spectra. The pn spectrum is shown in red, while the merged MOS spectrum is in black. The symbols follow figure 4.4.

Table 5.2: Best-fit spectral parameters.*

Parameter	Unit	XMM-Newton
$N_{\rm H}$	(10^{23} cm^{-2})	$2.3^{+0.4}_{-0.3}$
$k_{\rm B}T$	(keV)	$3.8^{+0.7}_{-0.7}$
$Z_{\rm Ar}$	(solar)	$2.9^{+7.1}_{-2.9}$
$Z_{\rm Ca}$	(solar)	$0.9^{+2.8}_{-0.9}$
$Z_{\rm Fe}$	(solar)	$0.9^{+0.2}_{-0.2}$
$F_{\rm X}$†	(10^{-12} erg s^{-1} cm^{-2})	$1.05^{+0.07}_{-0.07}$
$L_{\rm X}$‡	(10^{34} erg s^{-1})	2.9
χ^2/d.o.f.		69.9/74

* The uncertainty indicates the 90% confidence ranges of the fit.
† Energy flux in the 2.0–8.0 keV band.
‡ Absorption-corrected luminosity in the 2.0–8.0 keV band.
A distance of 8 kpc is assumed.

(2XMMp J174645.2–281547) in the Second XMM-Newton Serendipitous Source Pre-release Catalogue, XMM-Newton Survey Science Centre (2006). Also, hereafter we refer the Suzaku source as CXOGC J174645.3–281546.

Since no spectroscopic and temporal behaviors are presented for both of the Chandra

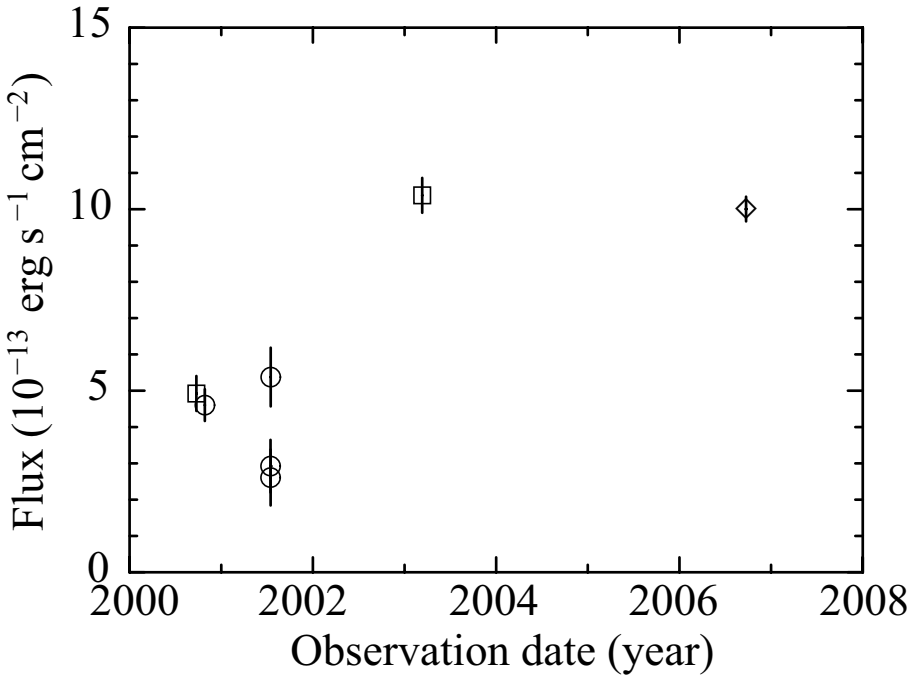

Figure 5.2: Long-term trend of X-ray flux in the 2.0–8.0 keV using XMM-Newton (squares), Chandra (circles), and Suzaku (a diamond). Error bars on the data points are plotted at the 90% confidence level.

and XMM-Newton sources in the literatures, we analyze the data and present the results here. One of the two XMM-Newton observations showed a net exposure of ~ 34 ks after removing data during high background. Spectra with high statistics were obtained from MOS and PN, for which we conducted spectral fits in a similar manner as with the Suzaku spectrum. The best-fit model and parameters are shown in figure 5.1 and table 5.2, respectively. Although the emission lines are less conspicuous in the XMM-Newton data, the Suzaku and XMM-Newton results are consistent with each other.

For the remaining one XMM-Newton and four Chandra observations, the photon statistics were too poor for a detailed spectral analysis, due to short exposures, chip gaps, and large off-axis angles of the source position. We therefore applied the best-fit Suzaku model to derive their flux.

Figure 5.2 shows a long-term flux variation, which spans ~ 6 years at seven different epochs. Although no flux variation within each observation is found, a long-term variation having a factor ~ 2 is clearly found.

5.1.2 Longer Wavelength Data

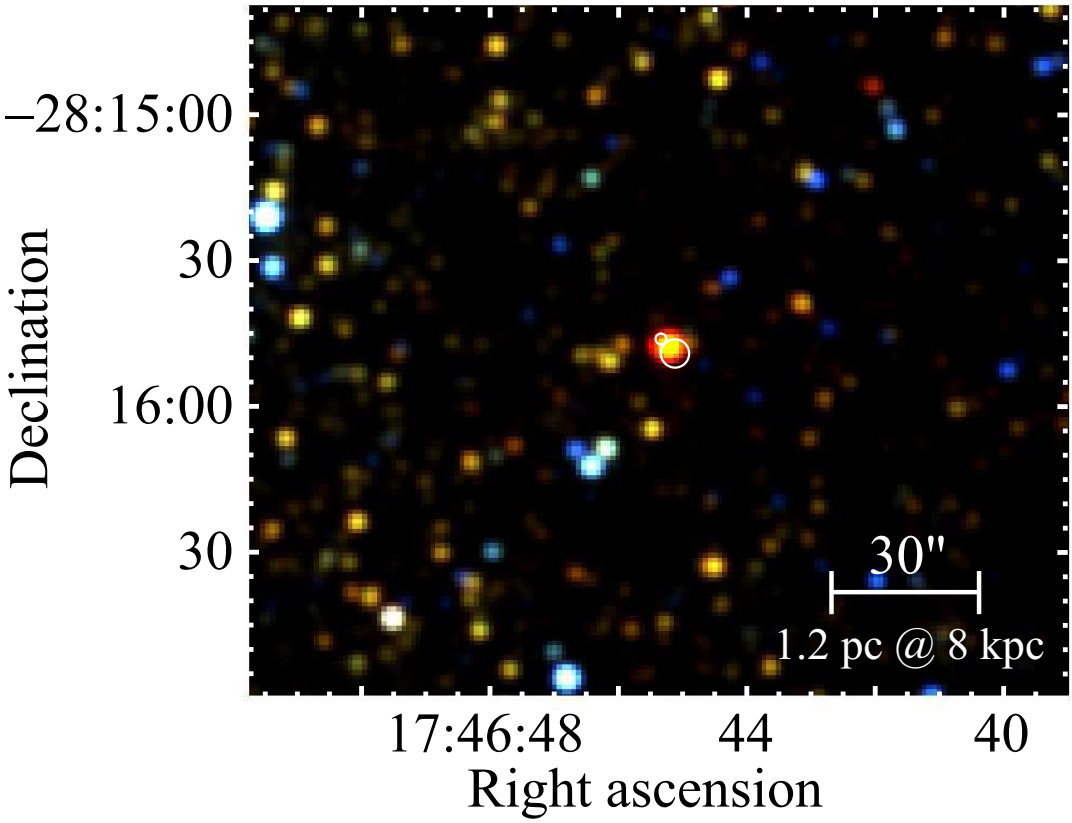

Figure 5.3: 2MASS image around CXOGC J174645.3–281546. J, H, and K band intensities are shown in blu, green, and red, respectively.

We retrieved other databases to characterize the multi-wavelength features of CXOGC J174645.3–281546. Because of the extreme extinction, the source is inaccessible in the optical bands.

In the near-infrared (NIR) bands, we examined the Two Micron All-Sky Survey (2MASS: Cutri et al. 2003; Skrutskie et al. 2006) and the NIR Galactic center survey (Nishiyama et al., 2006) using the Simultaneous Infrared Imager for Unbiased Survey (SIRIUS: Nagashima et al. 1999; Nagayama et al. 2003) on the Infrared Survey Facility (IRSF) telescope. In the mid-infrared (MIR) bands, we used the Midcourse Space Experiment (MSX: Egan et al. 2003) and the Galactic Legacy Infrared Mid-Plane Survey Extraordinaire program (GLIMPSE: Benjamin et al. 2003) using the Spitzer Space Telescope (Werner et al., 2004).

Figure 5.3 shows an NIR pseudo-color image, in which an isolated point-like source (2MASS J17464524–2815476 and MSX C6 G000.7036+00.1375) is found in the 2MASS and

MSX images within the positional uncertainty range of the Chandra source. The source is very bright and red with 2MASS magnitudes of (J, H, K_s) = (> 15.4, 10.0, > 7.2) mag. The J- and K_s-band magnitudes are upper limits due to nearby source contamination. In the SIRIUS data, while the K_s-band is unavailable due to saturation, the magnitudes of (J, H) = (15.53, 10.05) were derived with photometric errors of ~ 0.01 mag.

In the MIR bands, the source is in the linearity range in the MSX photometry, but is too bright in Spitzer images, from which no meaningful photometry was obtained. Figure 5.4 shows the spectral energy distribution (SED) in the 1.2–30 μm band. We fitted the data with a single-temperature blackbody and an assumed extinction proportional to the inverse square of the wavelength. We found the best-fit blackbody temperature ($T_{\rm BB}$) of 980 ± 20 K, with a visual extinction ($A_{\rm V}$) of 31 ± 1 mag, and a bolometric luminosity ($L_{\rm bol}$) of $(8.3 \pm 0.5) \times 10^4\ L_\odot\,(d/8.0\ [\mathrm{kpc}])^2$.

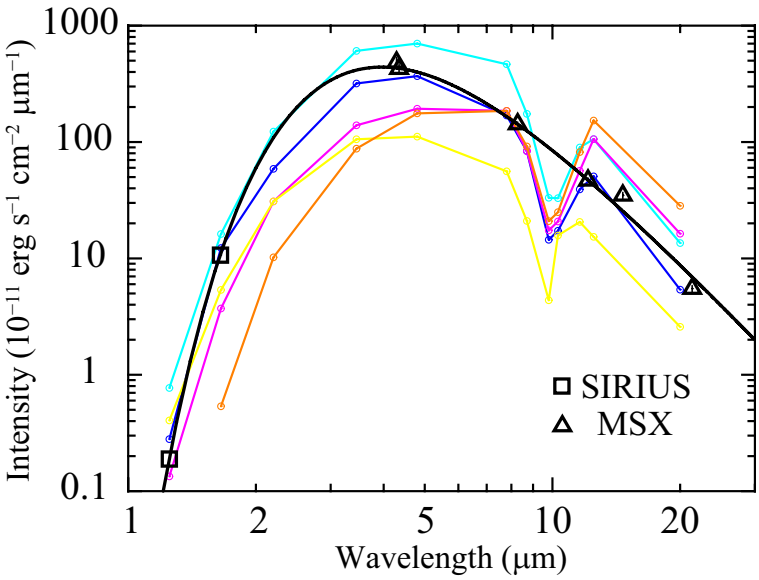

Figure 5.4: SED constructed from SIRIUS (open squares) and MSX (open triangles) photometry. The solid curve shows the best-fit blackbody model with $T_{\rm BB}$ = 980 K, $A_{\rm V}$ = 31 mag and $L_{\rm bol}$ = $8.3 \times 10^4\ L_\odot$. SEDs of the eponymous Quintuplet cluster members (Okuda et al., 1990; Figer et al., 1999a) are also shown with colors for comparison.

5.1.3 Location of Extinction Matter

Adopting $N_{\rm H}/A_{\rm V} = 1.79 \times 10^{21}$ cm^{-2} mag^{-1} (Predehl & Schmitt, 1995), $A_{\rm V} = 31$ mag is converted to $N_{\rm H} \sim 5.6 \times 10^{22}$ cm^{-2}. This is far smaller than that determined with the X-ray of $N_{\rm H} \sim 2.4 \times 10^{23}$ cm^{-2}. Since the visual extinction of 31 mag is the typical value toward

the Galactic center (Catchpole et al., 1990), the excess X-ray absorption is probably due to local obscuring matter that radiates the detected IR emission. If such an obscuring matter with solar abundance spherically surrounds the X-ray source, the 6.4 keV line with an EW of ~ 200 eV should be detected (Inoue, 1985). The lack of 6.4 keV line (EW < 50 eV) requires either that the iron abundance is $\lesssim 0.25$ solar or that the local matter is concentrated in front of the source along the line of sight.

5.1.4 Nature of the Source

WR Binary Origin

The SED of CXOGC J174645.3–281546 in the IR bands is very similar to those of the eponymous Quintuplet cluster members (figure 5.4). The five stars have cool ($T \sim 1000$ K) spectra and are bright (~ 7 mag in the K-band). The deep absorption at ~ 10 μm is due to interstellar silicate. The lack of either emission lines or intrinsic absorption features (Okuda et al., 1989; Figer et al., 1999a) allows no spectral classification, though their luminosity of $\sim 10^5$ $L_\odot$ corresponds to those of supergiant stars. These intriguing stars were recently spatially resolved (Tuthill et al., 2006). Two (GCS 3–2 and GCS 4 of Nagata et al. 1990, or Q2 and Q3 of Moneti et al. 2001) out of five showed beautiful pinwheel nebulae of dust plume, which are seen in a few WC stars (Tuthill et al., 1999; Monnier et al., 1999). Circumstellar dust emission with temperatures of 700–1700 K is a common character of WC stars (Williams et al., 1987).

Interestingly, the two sources that exhibit the pinwheel morphology are the brightest hard X-ray sources (Law & Yusef-Zadeh, 2004; Wang et al., 2006) among the Quintuplet members. Since both the pinwheel dust plumes and the hard X-ray emission indicate fast wind-wind collision (Tuthill et al., 1999; Monnier et al., 1999; Oskinova et al., 2003), this coincidence is not probably accidental. The summed spectrum of three X-ray emitting sources (GCS 3-2, GCS 4, and source D of Nagata et al. 1990) in the Quintuplet cluster is very hard ($kT \sim 9$ keV) and shows a hint of iron K emission line, but the luminosity is smaller by ~ 2 orders of magnitude (7.6×10^{32} erg s^{-1} in the 0.3–8.0 keV band; Wang et al. 2006) than CXOGC J174645.3–281546. In the colliding wind binary scenario, the X-ray luminosity scales as $L_{\rm X} \propto D^{-1}$ (Stevens et al., 1992), where D is the binary orbital separation. The large X-ray luminosity of CXOGC J174645.3–281546 indicates the close separation, and the moderate flux variation having a factor of ~ 2 can be interpreted as the variation of the separation due to the orbital motion.

Some of evolved massive star+OB star systems have very large X-ray luminosities up to $\sim 10^{35}$ erg s^{-1} in the 0.5–10.0 keV band with thermal spectra with a temperature of $\gtrsim 2$ keV

and an iron abundance of 1–2 (η Carinae: Tsuboi et al. 1997, Hamaguchi et al. 2007b; WR 140: Koyama et al. 1994, Pollock et al. 2005, A1 S, A1 N, and A2 in the Arches cluster; Wang et al. 2006). The X-ray spectral property of CXOGC J174645.3–281546 coincides with those of these massive star binaries, though near- and mid-IR spectroscopy and high spatial resolution observations are essential for further constraints. All of the observational results are consistent with the idea that CXOGC J174645.3–281546 is a WC star+massive star binary near the Galactic center, which has local obscuring matter (figure 5.5).

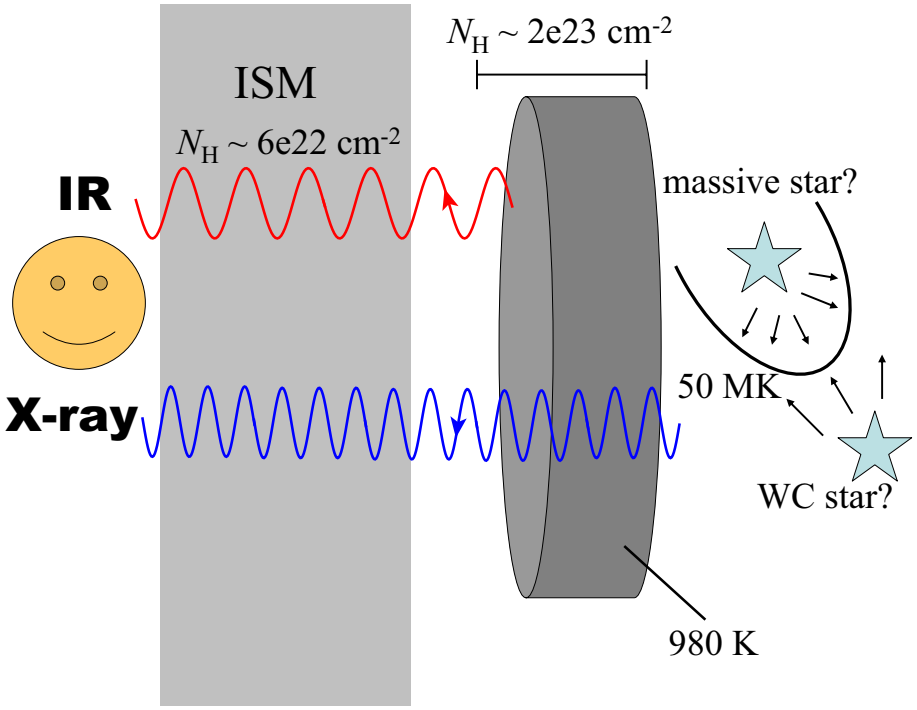

Figure 5.5: Cartoon of the source system. Winds from the primary WC star and the companion massive star collide to produce X-rays. The obscuring material of $N_{\rm H} \sim 2 \times 10^{23}$ cm^{-2} around the binary system is heated to $T \sim 980$ K by photospheric emission to emit IR. Whereas the IR emission suffers only interstellar medium (ISM) extinction, the X-ray emission is subject to additional intrinsic absorption.

Because the initial mass of a WR star exceeds $\sim$20 $M_\odot$ and the age is less than $\sim$6 Myr (Maeder & Meynet, 1987; Massey et al., 1995; Meynet & Maeder, 2005), we naturally expect that WR stars are found in large young star clusters, assuming a usual initial mass function. Our source, however, seems to be isolated (figure 5.3). Muno et al. (2006a) and Mauerhan et al. (2007) also recently discovered such isolated massive stars in the Galactic center region. One possibility is that these stars were formed initially in a cluster, and the cluster dissipated due to the strong tidal force of the Galactic center (Portegies Zwart et al., 2002a). Future IR and X-ray observations with a higher spatial resolution and sensitivity may reveal that

either this source is really a cluster member, or truly an isolated star.

Other Possible Origins

The most populous class of hard X-ray sources that exhibits iron K-shell emission lines is cataclysmic variables (CVs). The X-ray luminosity of CXOGC J174645.3–281546 of 3×10^{34} erg s^{-1} is at the brightest end of CVs. The bolometric luminosity of $\sim 10^5\ L_\odot\,(d/8.0\ [\mathrm{kpc}])^2$, however, is far larger than CVs, because most of the optical companions of CVs are late-type main-sequence stars. The spectra of CVs are characterized by hard continuum, with three iron K-shell emission lines at 6.4 keV, 6.7 keV, and 6.97 keV. The equivalent widths of both the 6.4 keV and 6.7 keV lines are, however, around 100–200 eV, although in some cases that of the 6.7 keV line shows an exceptionally high value possibly due to resonance scattering (Terada et al., 2001). The 6.97 keV/6.7 keV flux ratio of CVs is larger than 0.1, indicating that the ionization temperature is higher than $\sim$4 keV (Ezuka & Ishida, 1999; Hellier & Mukai, 2004; Rana et al., 2006). CXOGC J174645.3–281546 has a significantly larger equivalent width of the 6.7 keV line ($\sim$ 1 keV) and lower flux ratio of the 6.97 keV/6.7 keV lines than those of CVs. The upper limit of 50 eV for the 6.4 keV line, on the other hand, can not give any constraint on the possibility of a CV. Altogether, CXOGC J174645.3–281546 is very unlikely to be a CV.

The X-ray spectra of YSOs are characterized by a thin thermal plasma with a temperature of 1–5 keV and a metal abundance of around 0.3 solar in the quiescent phase (Feigelson et al., 2002; Imanishi et al., 2003; Ozawa et al., 2005). The CXOGC J174645.3–281546 iron abundance of 0.8 ± 0.1 solar is higher than the typical YSO value of 0.3 solar, but is not exceptional. Although the ratio of the X-ray and bolometric luminosity ($L_\mathrm{X}/L_\mathrm{bol}$) of 10^{-5} is in the range of low-mass YSOs (Imanishi et al., 2001; Feigelson et al., 2002), the absolute luminosities are too high for a YSO if CXOGC J174645.3–281546 is located at 8 kpc. The possibility still remains that CXOGC J174645.3–281546 is a foreground YSO in a dense molecular cloud.

5.2 Carina Nebula

5.2.1 Discrete Sources

WR 25

WR 25 is a very bright WR star in the optical band ($V \sim 8.1$ mag). From the WN-type emission lines and O-type absorption lines (Smith, 1968), this object is classified as a WN6h+O4f binary (Smith et al., 1996; van der Hucht, 2001). The X-rays from WR 25 were detected by Einstein for the first time (Seward et al., 1979). The luminosity is unusually high ($\sim 10^{34}$ ergs s^{-1} in the 0.5–10.0 keV band; Raassen et al. 2003) and shows a year-scale variability (Pollock & Corcoran, 2006). After the report by Pollock & Corcoran (2006), Gamen et al. (2006, 2008) discovered a periodicity in radial velocity of the N IV emission line at λ =4058 Å for the first time, which should arises from the binary motion. The orbital period is 207.7 ± 0.1 days and the eccentricity is 0.56 ± 0.01.

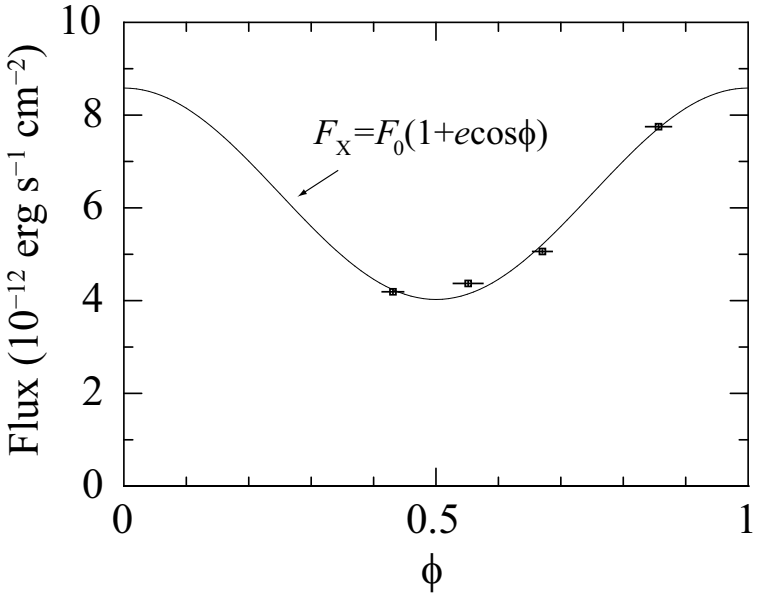

Figure 5.6: Long-term flux variation of WR 25 as a function of orbital phase. Best-fit Stevens' model is shown with a solid line.

Figure 5.6 shows the long-term X-ray flux variation of WR 25 as a function of the orbital phase (Gamen et al., 2006). The X-ray flux clearly depends on the orbital phase. Stevens et al. (1992) argued that the X-ray luminosity is proportional to the inverse of the binary orbital separation in the wind collision scenario. Since the binary separation D is expressed as $D \propto (1 + e\cos\phi)^{-1}$, the X-ray flux from a colliding-wind binary ($F_{\rm CWB}$) scales

as $F_{\rm CWB} \propto 1 + e\cos\phi$. Allowing e to vary, we fitted the light curve with the above function (figure 5.6). The best-fit value of e was ~ 0.3, which is significantly lower than that derived by Gamen et al. (2008). This indicates that the wind collision alone is not responsible for the X-ray emission.

To separate the X-ray flux into the intrinsic and colliding-wind component, we fixed e to 0.56 and added a constant value, i.e., we fitted the flux with a function $F_{\rm X} = F_0 + F_1(1 + 0.56\cos\phi)$. The best-fit values are $F_0 = 2.2 \pm 0.1 \times 10^{-12}$ and $F_1 = 4.1 \pm 0.1 \times 10^{-12}$ erg s^{-1} cm^{-2} in the 1.0–8.0 keV band.

HD 93205

Although HD 93205 is a binary of two high mass stars (O3 V + O8 V; Conti & Walborn 1976) with a large eccentricity ($e = 0.42$; Morrell et al. 2001), the X-ray emission is soft and steady, as was pointed out by a previous study (Albacete-Colombo et al., 2008). Assuming that $L_{\rm bol} = 1.3 \times 10^6\ L_\odot$, we obtain $L_{\rm X}/L_{\rm bol} \sim 1 \times 10^{-7}$, the typical value of massive stars (Lucy & White, 1980). HD 93205 does not show a signature of wind collision probably because they are too close ($a_1 \sin i \sim 1.0 \times 10^7$ km and $a_2 \sin i \sim 2.4 \times 10^7$ km; Morrell et al. 2001). If we adopt the inclination angle of $\sim 60^\circ$ calculated by Benvenuto et al. (2002), the separation is comparable to the radius of an O3 V star, 15 $R_\odot$ (Cox, 2000). Since the critical point of stellar wind acceleration is located at the distance of ~ 6 times the stellar radius (Abbott 1980, figure 2.6), the stellar winds from the two stars probably collide before they are accelerated enough to produce hard X-rays. Morrell et al. (2001) reported an apsidal motion at a rate of $0.^\circ032 \pm 0.^\circ0031$ per cycle. They argued that tidal and rotational distortions is the main cause of this apsidal motion, which also supports the closeness of the binary.

HD 93250

HD 93250 has some features similar to WR 25. The temperatures of HD 93250 are $k_{\rm B}T_{\rm low} = 0.62$ (0.59–0.65) keV and $k_{\rm B}T_{\rm high} = 3.1$ (2.9–3.3) keV, while those of WR 25 are $k_{\rm B}T_{\rm low} = 0.62$ (0.61–0.63) keV and $k_{\rm B}T_{\rm high} = 2.33$ (2.27–2.39) keV (table 4.9). The Fe abundance in HD 93250 is 0.36 (0.22–0.50) solar and 0.28 (0.25–0.31) solar in WR 25. The only clear difference is the X-ray luminosity with a factor of 4–8 (depending on the orbital phase of WR 25). These similarities in the spectral shapes indicate that some fraction of the X-ray in HD 93250 arises from wind collision, although there is no evidence for binarity from optical observations.

5.2.2 Diffuse Sources

Comparison with Previous Results

In section 4.2., we selected three regions according to the morphology in the 0.5–2.0 keV band (figure 4.8), and performed spectral analysis. The spectra were fitted with single temperature plasma model and emission above 2 keV was not found. On the other hand, the spectra in Hamaguchi et al. (2007) have harder components. This difference probably arises from the choice of photon extraction regions. Hamaguchi et al. (2007) chose larger regions with areas of ~ 110 and ~ 70 arcmin^2, while we accumulated photons from smaller regions that have high surface brightness with areas of $\sim$ 10–20 arcmin^2 to obtain higher signal-to-noise ratios. Hamaguchi et al. (2007) attributed the difference of spectral shape in north and south regions to the difference of the metal abundance. However, we found that the absorption columns and temperatures also show significant spatial variations. The temperature of diffuse 1 and 2 regions is ~ 0.55 keV and the absorption value is small, while the temperature of diffuse 3 region is lower (~ 0.18 keV) and the absorption column is typical of this field (table 4.10).

5.2.3 The Plasma Properties

Since the absorption columns of diffuse 1 and 2 are significantly smaller than other sources in this region, it is likely that the emitting source is located in front of the Carina Nebula and may not be physically related to it. The iron abundance is ~ 5 times larger than Ne or O which implies a type Ia SN origin.

Diffuse 3 is likely to be located at the Carina Nebula distance from its absorption column. Assuming a distance of 2.3 kpc, we can estimate the plasma mass. From the spectral analysis, a volume emission measure of $\sim 10^{58}$ cm^{-3} is obtained. If we further assume that the plasma is uniformly distributed in an ellipsoid of 1 pc$\times$1 pc$\times$2 pc, the electron density and the plasma mass are 5 cm^{-3} and 1.5 $M_\odot$. This amount of plasma can be fueled either by WR 25 with $\dot{M} \sim 3.6 \times 10^{-5}$ $M_\odot$ yr^{-1} (Crowther et al., 1995) or O stars in Tr 14 and Tr 16 within 10^5 yr. We see no N emission line at 0.5 keV and obtained upper-limit values of N/O<0.5 and N/Fe<0.3.

5.3 M 17

5.3.1 Discrete Sources

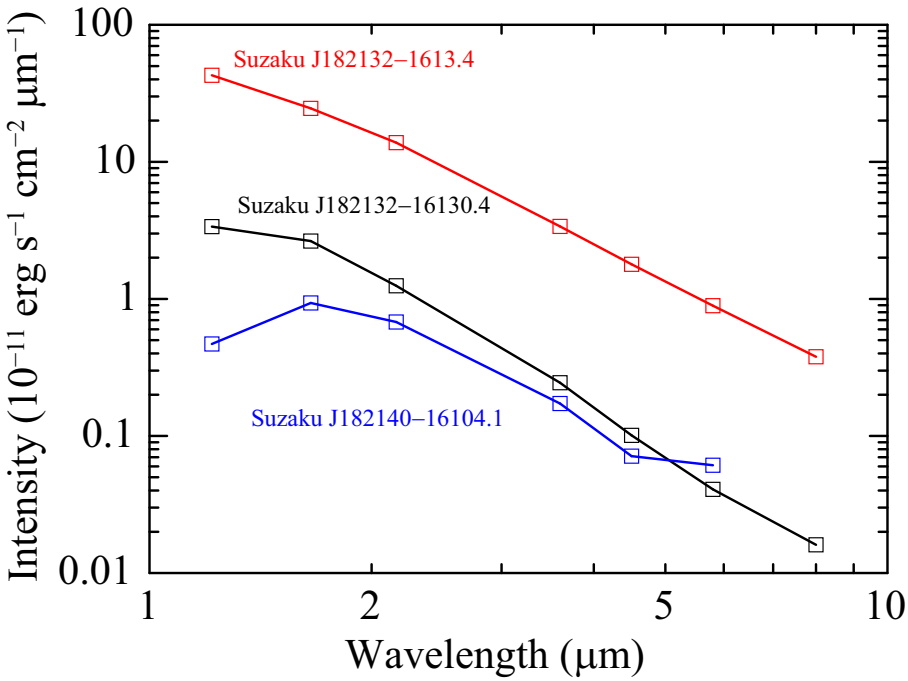

Figure 5.7: NIR to MIR SED of three point sources in the M17 east field. 2MASS and Spitzer of Suzaku J182132–1610.4, Suzaku J182132–1613.4, and Suzaku J182140–1604.1 are shown in black, red, and blue squares respectively.

We detected three point sources in the M17 East field. In order to identify their nature, we retrieved databases of other wavelengths. We examined 2MASS All-sky Point Source Catalog (Cutri et al., 2003; Skrutskie et al., 2006) and GLIMPSE (Benjamin et al., 2003). We found counterparts for all three sources in both catalogs (table 5.3). Their SEDs are shown in figure 5.7.

Suzaku J182132–1610.4

The absorption column ($N_{\rm H}$) of Suzaku J182132–1610.4 (table 4.14) is consistent with the typical value of $A_{\rm V} = 2$ mag in this region (Hoffmeister et al., 2008) using $N_{\rm H}/A_{\rm V} = 1.79 \times 10^{21}$ cm^{-2} mag^{-1} (Predehl & Schmitt, 1995). After correcting for the distance modulus and the extinction, the magnitude and the color indicate that this is a B8 V star. Since

intermediate mass stars are dim in the X-ray and Suzaku J182132–1610.4 shows flux variability with a time-scale of ~ 10 ks similar to those seen in young stellar objects (Imanishi et al., 2003; Getman et al., 2008), a probable nature is a foreground (~ 200 pc) young stellar object. In this case, the absorption is mainly of an intrinsic origin but not of ISM origin. The absorption column is typical of young stellar objects (Feigelson et al., 2005).

Suzaku J182132–1613.4

The $N_{\rm H}$ value of Suzaku J182132–1613.4 is also typical to this region. The J, H, and K magnitudes of Suzaku J182132–1613.4 are consistent with a B0 V star at a distance of 2.1 kpc. However, the X-ray spectrum is too hard and has a too high $L_{\rm X}/L_{\rm bol}$ value ($\sim 10^{-6}$) compared with the conventional value of $\sim 10^{-7}$ (Lucy & White, 1980; Pallavicini et al., 1981). We speculate that this object is also a binary comprised of a B0 V star and an unresolved massive companion.

Suzaku J182140–1604.1

This source, in contrast to the previous two sources, shows a high $N_{\rm H}$ value and a very strong iron K emission line with an EW of ~ 2 keV. The probable counterpart shows red excess ($J-H \sim 1.85$ mag). From the NIR brightness, it is unlikely to be a background active galactic nucleus. A possible nature is an embedded protostar.

OI 352

OI 352 is classified as an O8 V star based on UBV photometry (Ogura & Ishida, 1976). This source is too bright and too hard for a single O8 V star, which indicates the X-ray emission is of wind collision origin. The absorption column is larger than those of diffuse sources and diffuse emission is seen in the NIR image (figure 4.20), implying that this source is embedded in a molecular cloud.

M17 North

M17 North is not point like with the PSF of XRT. Broos et al. (2007) detected ~ 10 sources from this region. Together with the fact that the absorption column ($N_{\rm H} = 2.4 \pm 0.3 \times 10^{22}$ cm^{-2}) is consistent with those of molecular cloud clumps A8–A13 in Wilson et al. (2003), M17 North is likely to be embedded young stellar objects. The temperature ($k_{\rm B}T = 2.7^{+0.5}_{-0.3}$ keV, table 4.13) is a typical value of class-I protostars (Imanishi et al., 2003).

OB association

We detected Kα emission lines from highly ionized ions (figure 4.31c). The spectrum of the OB association is comprised of hundreds of point sources, but the emission from an O4–O5 binary dominates the spectrum. Broos et al. (2007) claimed that both components of the binary (sources 543 and 536) have plasma temperatures exceeding 10 keV. However, the strong Fe XXV Kα line at 6.7 keV and the weak Fe XXVI Kα line at 7.0 keV in the XIS spectrum (figure 5.10c) do not support such high temperatures.

Table 5.3: Counterparts of three unidentified point sources in the M17 East field

Source ID	2MASS source			Spitzer source			
	J (mag)	H (mag)	K (mag)	3.6 μm (mag)	4.5 μm (mag)	5.8 μm (mag)	8.0 μm (mag)
Suzaku J182132–1610.4	2MASS J18213225–1610285			SSTGLMC G015.1779–00.9065			
	12.42 ± 0.02	11.58 ± 0.02	11.34 ± 0.02	11.06 ± 0.05	11.05 ± 0.08	11.00 ± 0.12	10.68 ± 0.22
Suzaku J182132–1613.4	2MASS J18213201–1613239			SSTGLMC G015.1334–00.9285			
	9.66 ± 0.02	9.16 ± 0.02	8.73 ± 0.02	8.21 ± 0.04	7.93 ± 0.04	7.65 ± 0.4	7.25 ± 0.03
Suzaku J182140–1604.1	2MASS J18214023–1604128			SSTGLMC G015.2850–00.8857			
	14.56 ± 0.03	12.71 ± 0.02	12.00 ± 0.02	11.44 ± 0.05	11.43 ± 0.09	10.56 ± 0.11	—

5.3.2 Diffuse Sources

Contamination to the Extended Emission

The spectra of the diffuse emission in figure 4.33 are contaminated by other sources of emission. We evaluate the levels of contamination by unresolved point sources, the Galactic Ridge X-ray emission (GRXE), the cosmic X-ray background (CXB), and the local hot bubble (LHB), and argue that their contributions to the background-subtracted spectra are negligible. About 70% of the XIS field is covered in the Chandra observation which has a much better spatial resolution and sensitivity for faint point sources (Townsley et al., 2003; Broos et al., 2007). Among the five sub-regions, the region 2 has a complete coverage by Chandra. We therefore use this sub-region as a representative to evaluation the levels of various contaminations.

First, we examine the contribution of unresolved point sources. We extracted 19 point sources from the ACIS data in the region 2, constructed the composite spectrum, and fitted it with a thermal plasma model. The spectrum of each source is too poor to fit individually, so we assume that all sources have the same spectral shape that best describes the composite spectrum. Using their positions, flux, and the assumed spectral shape, we generated their XIS events using a ray-tracing simulator (`xissim`; Ishisaki et al. 2007). In figure 5.8, we compare the integral of the simulated spectra of unresolved point sources (PS1) to the observed diffuse spectrum (pluses). In the displayed observed spectrum, we subtracted the NXB spectrum but not the background spectrum in the neighboring region. The point source contribution accounts for $\sim 8\%$ of the emission in the 0.4–1.8 keV band.

To have an estimate of the maximum contamination to the lines, we repeated the same procedure using the model with the maximum allowable abundance values in the best-fit model for simulating unresolved point source events. The resultant integrated spectrum (PS2) is also shown in figure 5.8. At the Ne IX line at 0.92 keV, the contribution by the point sources accounts only for $<10\%$ of the observed emission.

Second, we derive the GRXE contribution, which is ubiquitous along the Galactic Plane at Galactic longitudes (l) of $|l| \lesssim 45^\circ$ (Kaneda et al., 1997; Sugizaki et al., 2001). We refer to a Chandra result (Ebisawa et al., 2005) for the spectral shape in the soft band and to a Rossi X-ray Timing Explorer result (Revnivtsev et al., 2006) for the surface brightness at the position of M17 ($l \sim 15^\circ$). The GRXE contribution to the observed emission is estimated to be $\sim 3\%$ and is shown in figure 5.8.

Third, for the CXB contribution, we consulted the Suzaku XIS observation of the North Ecliptic Pole (Fujimoto et al., 2007) both for the spectral shape and the surface brightness. The CXB was observed and fitted by a power-law model. We convolved the model with the

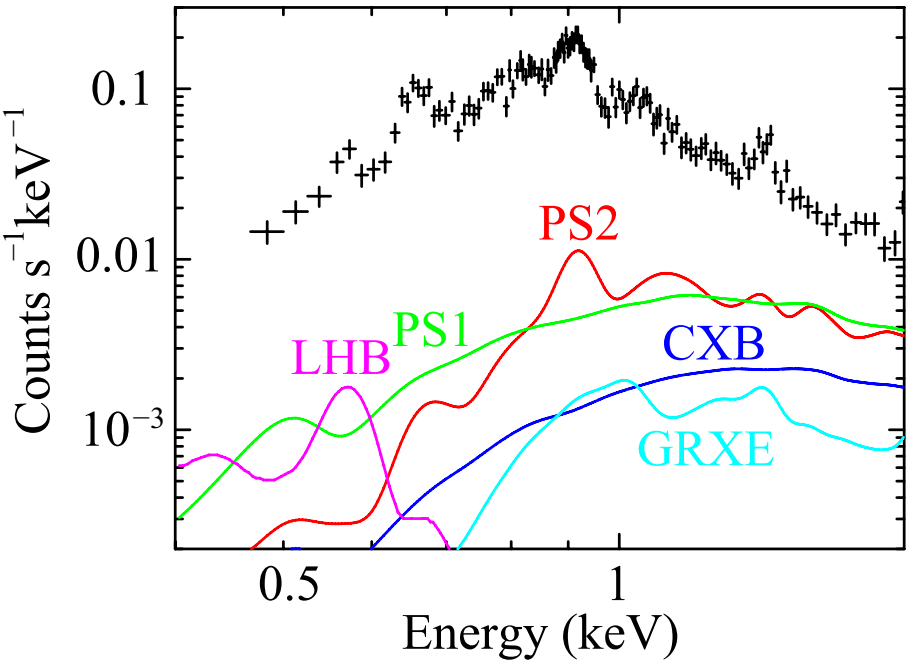

Figure 5.8: Comparison of the observed diffuse spectrum to the simulated spectra of contaminating sources. The NXB signal is subtracted from the observed spectrum. PS1 and PS2 are for the contribution of unresolved point sources with different spectral models, GRXE for the Galactic Ridge X-ray emission, CXB for the cosmic X-ray background, and LHB for the local hot bubble. None of them play a significant contribution. Moreover, most of them are removed by subtracting a background spectrum from the neighboring region.

XIS responses and found that the contribution is $\sim 2\%$.

Finally, we constrain the contribution by the LHB emission. We estimate its surface brightness to be $\sim 4\times10^4$ counts s^{-1} arcmin^{-2} in the PSPC R1 and R2 bands (Snowden et al., 1998). We assume that the spectrum is a thin-thermal plasma (the Raymond-Smith model; Raymond & Smith 1977) with a temperature of 0.1 keV. With the derived emission measure of $\sim 2.8 \times 10^{-3}$ cm^{-6} pc, the LHB contributes $\sim 2\%$ of the observed emission.

None of the above components play a significant role in the observed diffuse spectrum. Moreover, we removed most of them by subtracting a background spectrum from a neighboring region. The background events show no indication of time variability caused by solar flares (Fujimoto et al., 2007). We conclude that the background-subtracted XIS spectrum represents the spectrum of the uncontaminated diffuse emission quite well.

The background spectrum accounts for $\sim 35\%$ of the source spectrum of the sub-region "diffuse 1". Besides the NXB contributing $\sim 7\%$ of the source flux, the sum of unresolved point sources, GRXE, CXB, and LHB contributes $\sim 15\%$. Therefore, emission with a flux of $\sim 13\%$ of the source flux is additionally included in the background spectrum. The contribution from the bright sources outside of the extraction region is negligible. We attribute the remaining emission to the diffuse emission in the background region. If this is the case, the flux estimate of the diffuse emission (table 4.15) is underestimated by $\sim 13\%$.

Comparison with Previous Studies

We compare our results with the previous works using ROSAT (Dunne et al., 2003) and Chandra (Townsley et al., 2003; Broos et al., 2007). We derived that the diffuse spectrum is explained by an absorbed single temperature thin-thermal plasma model of $k_{\rm B}T \sim 0.25$ keV and $N_{\rm H} \sim 4.5 \times 10^{21}$ cm^{-2}. The total luminosity (0.5–2.0 keV) in the combined diffuse1–6 regions is $\sim 5.2\times10^{33}$ erg s^{-1}.

The ROSAT study (Dunne et al., 2003) shows that the total luminosity of the diffuse emission is $\sim 2.5\times10^{33}$ erg s^{-1}. The smaller estimate than our result is more noticeable if we consider that the ROSAT value was derived from a larger area and in a wider energy range (0.1–2.4 keV). This stems from an underestimate of the extinction. Without a sufficient spectral resolution to resolve lines, two different models were not disentangled in the ROSAT PSPC spectra; one is a low plasma temperature with a large extinction (~ 0.2 keV and $\sim 10^{22}$ cm^{-2}) and the other is a high plasma temperature with a small extinction (~ 0.7 keV and $\sim 10^{20} - 10^{21}$ cm^{-2}). Dunne et al. (2003) derived the luminosity based on the latter, but our spectroscopy shows that the former should be in the case.

The best-fit XIS value of $N_{\rm H}$ is consistent with that presented in the Chandra study

(Townsley et al., 2003), in which $N_{\rm H} = (4 \pm 1) \times 10^{21}$ cm^{-2}. However, the plasma temperatures are different between the two studies. In Chandra, the primary component of $k_{\rm B}T = 0.6 \pm 0.1$ keV and the secondary component of ~ 0.13 keV were claimed. In Suzaku, however, we confirmed that a single temperature component of ~ 0.25 keV is adequate from the diagnosis of resolved oxygen and neon lines.

Spatial Difference of the Plasma Properties

A high signal-to-noise ratio spectrum by XIS enabled us to conduct spatially-resolved spectroscopy of the diffuse emission. The plasma temperature and the chemical composition are uniform. The Chandra study (Townsley et al., 2003) also show no evidence for spatial variation of plasma temperature.

The observed uniformity indicates that the entire plasma is at a thermal equilibrium in the observed spatial scale of ~ 10 pc, unless the plasma is patchy at equilibria locally by magnetic confinement. The global equilibrium is reasonable considering the fact that the plasma sound crossing time ($\sim 4 \times 10^4$ yr) is much smaller than the time scale of the system ($\sim 10^6$ yr), thus the constant pressure is achieved (Weaver et al., 1977). Here, we used the plasma volume and the electron density as ~ 100 pc^3 and ~ 1 cm^{-3}, respectively, by assuming that the plasma distribution has a conical shape with its apex at the OB association and with a filling factor of 1. Given the uniformity of the plasma temperature and pressure, we speculate that the density is also spatially uniform.

The observed surface brightness, however, is different among the sub-regions (figure 4.24a, table 4.15). It is ~ 1.3 times more intense in the region 1 than region 2. This is not attributable entirely to the different extinction, as $N_{\rm H}$ is larger in the sub-region 1 than in 2. Because the plasma has a uniform temperature and density, we speculate that the difference of the surface brightness is likely due to the different line-of-sight depths or different filling factors.

With the derived plasma volume and the density, the total mass of the plasma is $\sim 2\ M_\odot$. This is comparable to the integrated ejecta mass by stellar winds at a mass loss rate of $\sim 10^{-6}\ M_\odot$ for $\sim 10^6$ yr and agrees with the estimates by the previous works (Dunne et al., 2003; Townsley et al., 2003). We also speculate that the swept-up and evaporated ISM does not make a significant contribution to the plasma mass.

Chemical Composition

The chemical composition of the diffuse emission is revealed for the first time in this study. The metallicity of the diffuse emission is 0.1–0.3 solar (table 4.15), which is signifi-

cantly lower than those derived for the discrete sources (0.3–1.5 solar). The metal abundances relative to each other in the diffuse emission are consistent with solar among O, Mg, and Fe (Anders & Grevesse, 1989), but Ne is enhanced in all three sub-regions by a factor of $\sim$2 (table 4.15). This is also evident in the simultaneous spectral fits of the three sub-regions, in which we tied the abundance values of these elements. The resultant values are $Z_{\rm O} = 0.12$ (0.11–0.13), $Z_{\rm Ne} = 0.22$ (0.21–0.25), $Z_{\rm Mg} = 0.10$ (0.08–0.12), and $Z_{\rm Fe} = 0.12$ (0.11–0.13) solar.

Such Ne enhancement from other metals is widely seen in coronally active stars (Brinkman et al., 2001; Kastner et al., 2002; Audard et al., 2003; Imanishi et al., 2003; Stelzer & Schmitt, 2004; Maggio et al., 2007) for unknown reasons. We consider that the Ne enhancement is an intrinsic feature of the diffuse plasma, and is not influenced by the contamination of Ne-enhanced point sources spectra (§ 5.3.2). One explanation for the anomaly is that the poorly-constrained solar Ne abundance is underestimated by a factor of a few (Drake & Testa, 2005; Liefke & Schmitt, 2006). This would account for the observed Ne enhancement in the M17 diffuse plasma as well.

The lack of a clear spatial variation of the chemical composition comprises a sharp contrast to the diffuse emission in the Carina Nebula (Hamaguchi et al., 2007), where the different abundance patterns across a similar spatial scale suggest the supernova origin for the emission. In the diffuse emission in M17, the O and Fe ratio is consistent with the solar abundance, which is another line of evidence against the supernova interpretation. If a supernova has occurred in M17, it should have been caused by a star earlier than the earliest (O4–O5) star in the OB association. Such a massive source causes a core-collapse–type supernova. It would have yielded a measurably larger ratio of O against Fe than the solar value by a factor of a few (Tsujimoto et al., 1995; Thielemann et al., 1996; Nomoto et al., 1997).

5.3.3 HXD signals

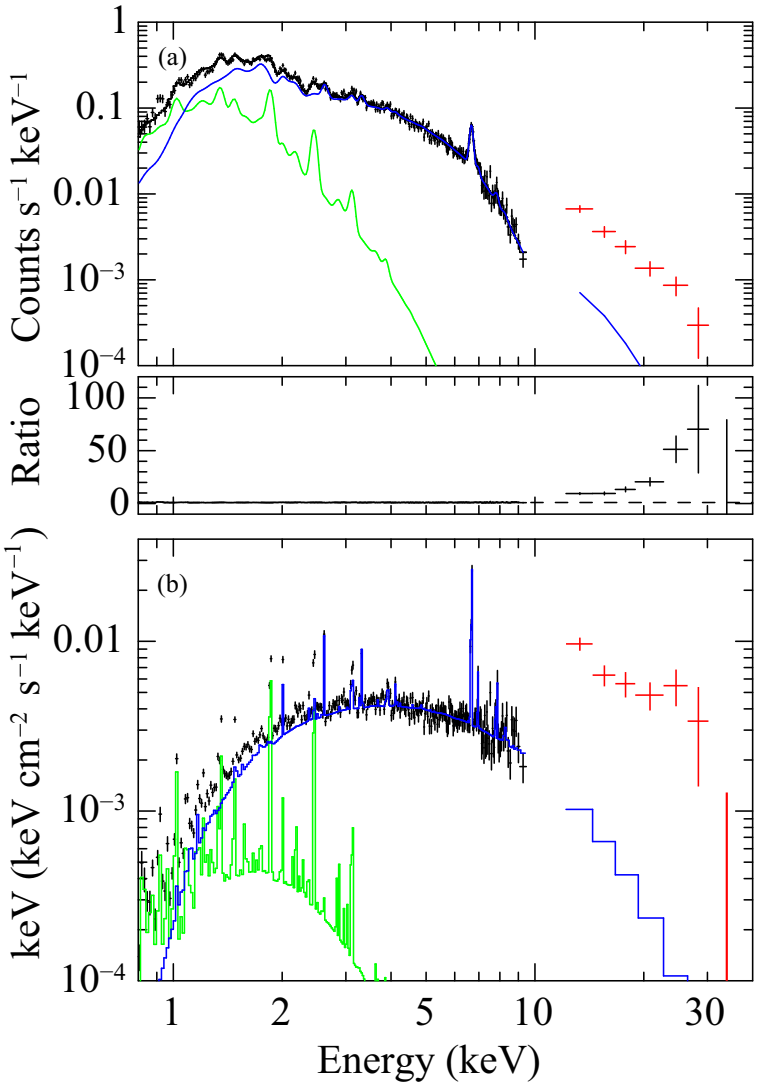

Figure 5.9: (a) Simultaneous fit of XIS (black) and PIN (red) spectra of M17 West. The low- and high- temperature components are respectively shown in green and blue. The lower panel shows the residual (data/model). (b) Unfolded νF_ν spectra.

In section 4.3.6, we detected significant signals with HXD/PIN in the 13–30 keV bands. We try to simultaneously fit the XIS and PIN spectra of OB association, the brightest object in the XIS FOV. Since the OB association is not located at the XIS nor HXD nominal position, the effective area of PIN decreases by $\sim 10\%$. We calculated corresponding arf using `hxdarfgen`, and applied it to the spectral analysis.

We fitted the XIS and PIN spectra simultaneously with two thermal components commonly modified by photoelectric absorption. Figure 5.9 shows the XIS and PIN spectra. The PIN data show large excess by a factor of 10–50 against the XIS. Any physical model cannot reproduce both the XIS and PIN spectra. Neither OI 352 nor M 17 North contributes to the PIN data. We conclude that the PIN signals are from outside the XIS FOV and inside the PIN FOV. The nearest bright source is AX J1819.2–1601. (figure 4.23, Sugizaki et al. 2001). At the position of AX J1819.2–1601, the effective area decreases by $\sim 80\%$ (See figure 6 of Takahashi et al. 2008). Extrapolating the power-law spectrum (table 4.16) to lower energy band, we estimate the 2.0–8.0 keV band flux to be ~ 2–4×10^{-10} erg s^{-1} cm^{-2}, which is larger than that reported in Sugizaki et al. (2001) by more than ten-fold.

Likewise, there is no bright source in the XIS FOVs in the observations of M 17 East and M 17 BG. Both of the nearest INTEGRAL sources 3EG J1824–1514 and AX J18192–1601 (figure 4.23) are out of HXD FOVs, which suggests that there are unknown bright hard X-ray sources in the FOVs of HXD but out of XIS FOVs.

5.4 Arches Cluster

5.4.1 Discrete Sources

Table 5.4: Observation Log

Obs ID	R. A. (J2000.0)	Decl. (J2000.0)	Date	$t_{\rm exp}$* (ks)	$\theta^\dagger$ ($'$)
945	$17^{\rm h}46^{\rm m}20^{\rm s}$	$-28°52'19''$	2000-07-07	49	7.2
2276	$17^{\rm h}46^{\rm m}05^{\rm s}$	$-28°46'28''$	2001-07-18	12	4.2
2284	$17^{\rm h}45^{\rm m}37^{\rm s}$	$-28°56'27''$	2001-07-18	11	7.8
4500	$17^{\rm h}45^{\rm m}56^{\rm s}$	$-28°49'01''$	2004-06-09	99	1.2

* Exposure time.
† Angular distance of the Arches cluster from the optical axis.

We retrieved the archived data taken by ACIS on-board Chandra and found that four observations cover the Arches cluster. ACIS has a field of view of $\sim 17'\times17'$ with a PSF radius of $\sim 0\farcs5$ at the optical axis and is sensitive in the 0.5–8.0 keV band with an energy resolution of ~ 150 eV at 6 keV and an effective area of ~ 50 cm^2 at 8 keV. The details of the observations are summarized in table 5.4. All the datasets were collected with the Timed Exposure mode, the nominal frame time, and the CCD temperature of –120°C.

Previous Chandra reports of the Arches cluster are based on ObsID=945 (Yusef-Zadeh et al., 2002), ObsID = 945, 2276, and 2284 (Law & Yusef-Zadeh, 2004), or ObsID = 4500 (Wang et al., 2006). We combine all the data in the presented analysis. Instead, we discard ObsID = 2284 because the observation is too short and the off-axis angle is too large. The total integration time of the three observations is ~ 160 ks, which is more than twice longer than the datasets used in the previous papers. We used the level 2 data processed at the Chandra X-ray Center. The known offset of the aspect solution[1] was compensated before merging the three datasets.

Figure 5.10 shows a close-up view of the Arches cluster. The four point-like sources were previously reported (Yusef-Zadeh et al., 2002; Law & Yusef-Zadeh, 2004; Wang et al., 2006). The ACIS frame was shifted so that A1S and A1N match their radio continuum counterparts (Lang et al., 2001). The photometric properties of these sources are summarized in table 5.4. No significant variation in the count rate is seen from all of these sources.

The three brightest sources are hard with almost all photons above 2 keV and are

[1]See http://cxc.harvard.edu/cal/ASPECT/fix_offset/ for detail.

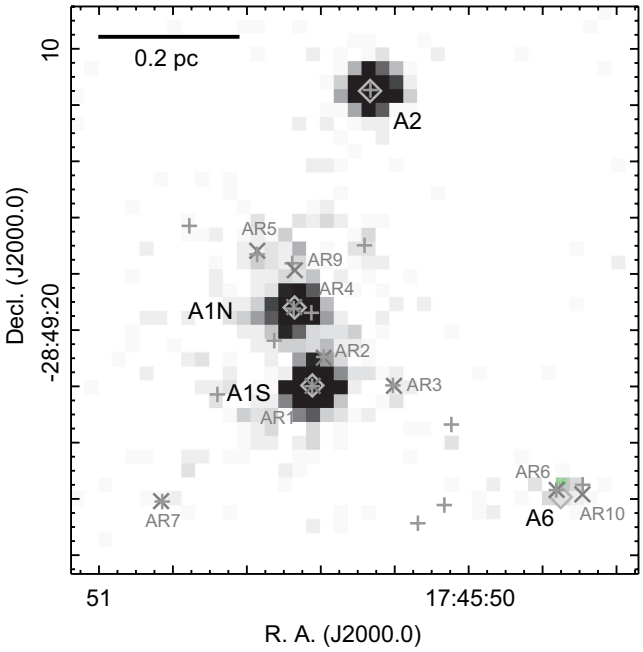

Figure 5.10: Close-up ACIS view of the Arches cluster using the best-focused ObsID=4500 data. The 0.5–8.0 keV intensity is plotted in linear scale to emphasize point-like emission. The position of X-ray, radio (Lang et al., 2001, 2005), and 30 brightest NIR (Figer et al., 2002) sources are represented by diamonds, crosses and pluses, respectively. The systematic offset of the NIR sources mentioned in (Lang et al., 2001) is corrected. Names of X-ray and radio sources are also shown. The upper one third of the field is out of the radio studies (Lang et al., 2001, 2005).

exceptionally bright among all near-by sources. Within 1.′4 around the cluster (the XIS source extraction region), the three sources alone account for $\sim 80\%$ of the total net count of all 21 point sources. There are dozens of sources with similar NIR brightness (Figer et al., 2002) yet no X-ray detections in the cluster. These NIR sources are considered to have less than ~ 10 counts, which is the lowest count of all the detected sources in the region. The three sources are thus an order of magnitude brighter than A6 and at least two orders of magnitude brighter than any other cluster members in the hard X-ray band.

Table 5.5: ACIS photometry of point sources.

ID*	R. A.† (J2000.0)	Decl.† (J2000.0)	C_{src}‡	C_{bkg}‡	P_{var}§	ME‖ (keV)	NIR#	Radio**
A1N	$17^h45^m50.46^s$	$-28°49'19.2''$	744	10.4	1.1×10^{-2}	3.5	N10, C5, B21, F7	AR4
A1S	$17^h45^m50.42^s$	$-28°49'21.9''$	1167	10.3	2.9×10^{-2}	3.7	N8, C8, B23, F6	AR1
A2	$17^h45^m50.26^s$	$-28°49'11.5''$	1031	20.6	4.4×10^{-1}	3.8	N5, C1, B26, F9	.....
A6	$17^h45^m49.74^s$	$-28°49'25.9''$	98	25.2	3.3×10^{-1}	4.3	F19	AR6

* Identification by Law & Yusef-Zadeh (2004) except for A6, which is a new source found in this study.
† The astrometric correction is applied to the X-ray data so that A1N and A1S match their VLA counterparts.
‡ Number of counts in the source region (C_{src}) and the contribution of background counts estimated from a surrounding region (C_{bkg}) in 0.5–8.0 keV.
§ The null hypothesis probability of the χ^2 value for the fit of light curves by a constant flux model.
‖ Median energy.
The NIR counteparts (N: Nagata et al. (1995), C: Cotera et al. (1996), B: Blum et al. (2001), and F: Figer et al. (2002)). The identification by Blum et al. (2001), Figer et al. (2002), and Lang et al. (2001) are compiled for the complete list.
** The radio counteparts (Lang et al., 2001). A2 is out of the study field by Lang et al. (2001, 2005).

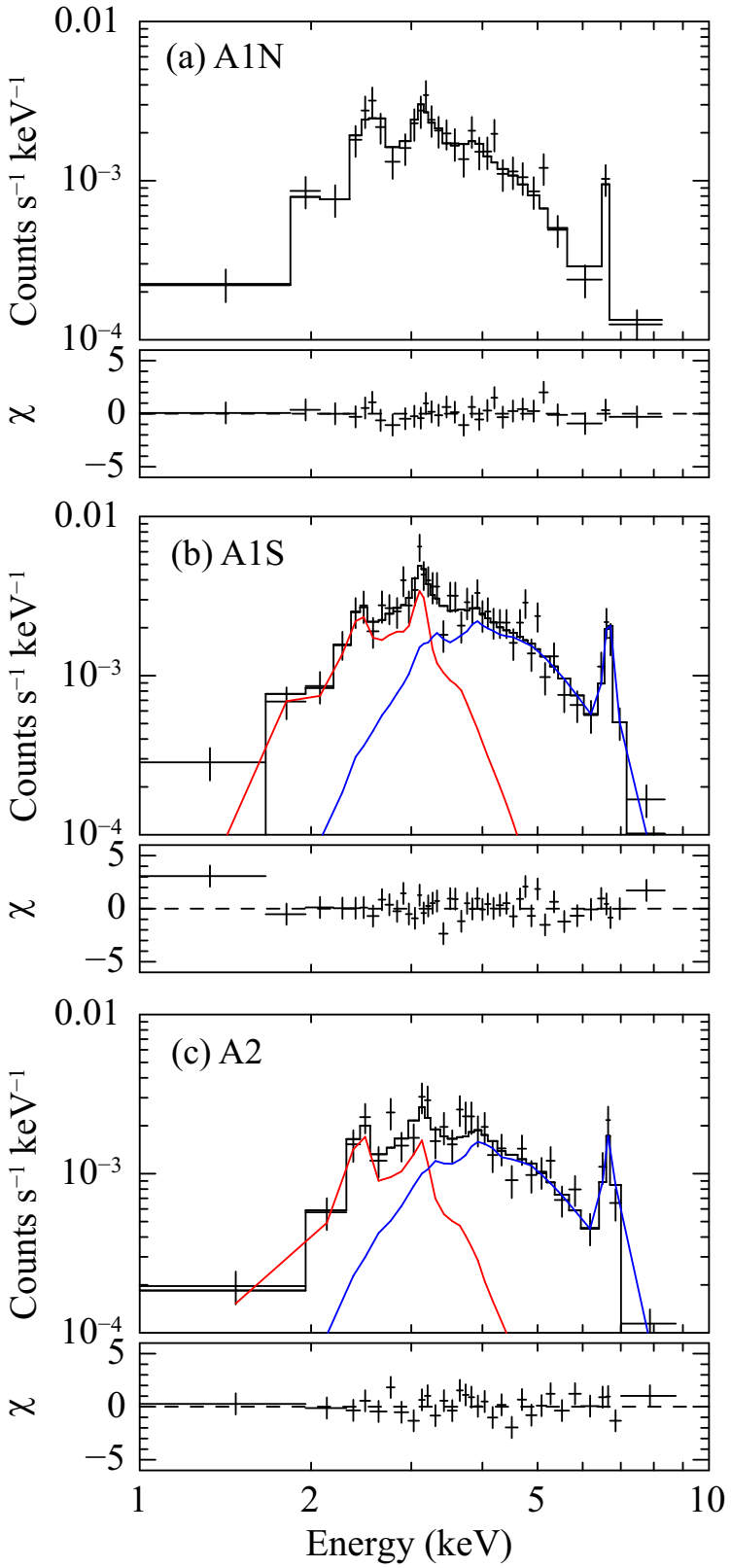

Figure 5.11: ACIS spectra and best-fit models of point sources: (a) A1N, (b) A1S, and (c) A2. Conspicuous emission lines are shown with arrows. The lower and higher temperature component are respectively shown with red and blue lines for A1S and A2.

The spectra of the three brightest X-ray sources are shown in figure 5.11. All the spectra are characterized by a strong cut-off at the soft end and emission lines from highly ionized ions including S XV ($\sim$ 2.4 keV), S XVI ($\sim$ 2.6 keV), Ar XVII ($\sim$ 3.1 keV), Ca XIX ($\sim$ 3.9 keV), and Fe XXV ($\sim$ 6.7 keV). From the intensity ratio of these lines, we can have a crude estimate of appropriate models for spectral fits. The brightest two sources (A1S and A2) show the Fe XXV line as well as the S XV line stronger than S XVI, requiring two thermal components of different temperatures. The faintest one (A1N) shows S XVI and no prominent Fe XXV, thus one-temperature model would be adequate.

Indeed, fits by two-temperature plasma for A1S and A2 and one-temperature plasma for A1N yielded acceptable fits. The best-fit parameters are summarized in table 5.6. Additional features of Gaussian lines and power-law tail, as was found in the XIS spectrum, are not confirmed in any of the spectra nor the composite spectrum of the three. The addition of these components in the fitting is not justified on a statistical basis, indicating that the point source spectra lack these components.

The fit by Yusef-Zadeh et al. (2002) was conducted for the composite spectrum of A1N and A1S, which was unavoidable due to the worse image quality of the ObsID = 945 data with the Arches cluster at a large off-axis angle. The composite spectrum deteriorates the information of S XV and S XVI line intensity of each source, wherein the former is stronger in A1S and the latter in A1N. As a result, it was impossible to decide whether a power-law or lower temperature component was necessary in addition to a higher temperature component.

We detected three bright and a faint point-like X-ray sources in the ACIS image. Most, if not all, of the emission in the three bright sources are from single stars (i.e., they are not the composite of unresolved multiple bright stars) for the following reasons. First, the radial profiles of the three sources perfectly fit with the PSF. We constructed an X-ray image deconvolved for the PSF using a maximum-likelihood reconstruction technique (Lucy, 1974), but no additional peak was found at near-by sources in the existing NIR and radio catalogs. Second, the positional coincidence of the X-ray and radio/NIR counterparts is superb with no measurable offset, suggesting that there are few blending sources.

The NIR identifications of the X-ray sources are given in table 5.5. Three of them (A1N, A1S, and A2) are detected by Blum et al. (2001) in their narrow-band images. From the He II (2.19 μm) and Brγ (2.17 μm) line ratio, Blum et al. (2001) discussed that these sources have a spectral type of either OIf4 or WN7–8. The degeneracy can not be solved by imaging information alone. Figer et al. (2002) presents high-resolution K-band spectra by NIRSPEC on the Keck II telescope. We confirmed N III (2.25 μm), Brγ, and He I (2.11 μm), He II (2.19 μm) emission as well as the deficiency of C IV (2.07 μm) in all these sources. We conclude that the three X-ray sources are WN7–8 stars. The remaining source (A6), on the other hand, has a featureless K-band spectrum without any strong H and He emission lines

Table 5.6: ACIS spectroscopy of point-like sources.

ID	$N_{\rm H}{}^{*}$ (10^{22} cm^{-2})	$k_{\rm B}T_{\rm high}{}^{*}$ (keV)	$k_{\rm B}T_{\rm low}{}^{*}$ (keV)	$F_{\rm X}{}^{*\dagger}$ (10^{-13} erg s^{-1} cm^{-2})	$L_{\rm X}{}^{\ddagger}$ (10^{33} erg s^{-1})
A1N	7.3 (6.2–8.7)	2.0 (1.6–2.6)	.....	1.3 (1.2–1.4)	2.3
A1S	15.1 (11.5–20.5)	2.5 (2.0–3.5)	0.4 (0.2–0.7)	2.3 (2.2–2.4)	15
A2	16 (9.1–21)	2.1 (1.5–4.5)	0.3 (0.2–0.9)	1.7 (0.52–4.4)	6.0

ID	$Z_{\rm S}{}^{*}$ ($Z_\odot$)	$Z_{\rm Ar}{}^{*}$ ($Z_\odot$)	$Z_{\rm Fe}{}^{*}$ ($Z_\odot$)	$P_{\chi^2}{}^{\|}$
A1N	2.7 (1.3–5.2)	2.7 (0.7–5.8)	1.6 (0.9–2.7)	0.92
A1S	0.7 (0.0–2.5)	5.6 (2.7–9.9)	1.8 (1.1–3.2)	0.45
A2	1.5 (0.6–3.1)	4.2 (0.7–8.5)	1.9 (1.1–2.6)	0.63

* Uncertainties in the paralentheses give the 90% confidence range. Those without the uncertainty indicate that they are fixed values.

† Energy flux in the 2.0–8.0 keV band.

‡ Absorption-corrected luminosity in the 2.0–8.0 keV band. A distance of 8 kpc is assumed.

§ The null hypothesis probability of the χ^2 value in the best-fit model.

(Figer et al., 2002). We consider, therefore, that it is likely an O star. It should be noted that this is the only source in Lang et al. (2001, 2005) with a negative index at 8.5 GHz, which is indicative of a colliding wind shock.

The three X-ray brightest sources are also among the twelve NIR brightest sources with an estimated initial mass of $\gtrsim 120\ M_\odot$ (Figer et al., 2002). Eleven of them (source 1–9, 11, 12 in Figer et al. 2002) are WN7–8 and the remaining one (source 9) is OIf4, based on the line ratio (Blum et al., 2001) and our inspection of the spectra presented in Figer et al. (2002); Najarro et al. (2004). Without an exception, the NIR brightest WN7–8 sources have radio continuum counterparts (Lang et al. (2001). Note that sources 9 and 11 are out of the radio study field). This is in sharp contrast with the hard X-ray result, in which only three of them are exceptionally bright and the remaining eight are fainter by more than two orders of magnitude. The NIR and radio emission may have the same origin, but the result strongly indicates that an additional factor (or several additional factors) is required for the hard X-ray production.

One plausible idea is the binarity (Law & Yusef-Zadeh, 2004). Among WR stars, those in a binary system with another massive star tend to have higher X-ray luminosity and harder

X-ray spectra (e.g., Pollock 1987). There has been no hint to suggest the binary nature of the X-ray sources in the Arches cluster, except for a possible K-band brightness change of A1N between Cotera et al. (1996) and Figer et al. (2002) after correcting a systematic offset between the two measurements. Long-term and homogeneous datasets in photometry or spectroscopy are necessary to test this idea.

It is interesting to note the extreme brightness of the brightest source A1S. Although the uncertainty is large, the estimated luminosity exceeds $\sim 10^{34.2}$ erg s^{-1} in the hard (2–8 keV) band alone. The luminosity in the soft (0.5–2.0 keV) band, which we can not quote due to the lack of photons in this range, would increase the value by a several factor. In fact, the luminosity of A1N is comparable to those of the brightest known stellar (=non-degenerated) X-ray sources in our Galaxy, including η Carinae (a luminous blue variable with $\sim 10^{34.6}$ erg s^{-1} in 0.5–10 keV; Corcoran et al. 2001), V444 Cygni (WN5+O6 with $\sim 10^{33.4}$ erg s^{-1} in 0.2–10 keV; Maeda et al. 1999), WR20a (WN6+WN6 with $\sim 10^{33.8}$ erg s^{-1} in 0.9–8.0 keV; Rauw et al. 2005), WR25 (WN6+O4f with $\sim 10^{34.5}$ erg s^{-1} in 0.5–8 keV; Evans et al. 2004), HD50896 (WN5 with $\sim 10^{32.9}$ erg s^{-1} in 0.5–10 keV; Skinner et al. 1998), WR147 (WN8+O8–9 with $\sim 10^{32.6}$ erg s^{-1} in 0.5–10 keV; Skinner et al. 1999), WR140 (WC7+O4–5 with $\sim 5 \times 10^{33}$ erg s^{-1} in 1–10 keV; Koyama et al. 1994), and γ^2 Velorum (WC8+O7.5 with $\sim 10^{32.6}$ erg s^{-1} in 0.5–10 keV; Stevens et al. 1996). Stars with higher luminosities are only seen in the R136 in 30 Doradus represented by CX5 (WN4.5 with $\sim 10^{35.1}$ erg s^{-1} in 2–8 keV; Portegies Zwart et al. 2002b; Townsley et al. 2006). The combination of the extreme mass loss rate ($\sim 2.2 \times 10^{-4}$; Lang et al. 2005), which is also one of the Galactic largest, and the possible binarity makes this source one of the brightest Galactic stellar source in the hard X-ray band.

5.4.2 Origin of Three Spectral Components

We identified three spectral components (thermal, power-law, and two Gaussian lines) in the XIS spectrum. Wang et al. (2006) conducted spatially-resolved Chandra spectroscopy of the Arches cluster in the 2–8 keV band and revealed a more detailed spatial structure upon the results by Yusef-Zadeh et al. (2002); Law & Yusef-Zadeh (2004). The Arches X-rays consist of three spatial components: (1) point-like sources with a thermal spectrum, (2) diffuse emission with a thermal spectrum in a $\sim 30''$ scale, and (3) diffuse emission with a ~ 6.4 keV line over a power-law continuum in a more extended scale ($\sim 60'' \times 90''$ by Yusef-Zadeh et al. 2002). The former two thermal components are concentrated at the cluster center, in which three brightest point sources dominates the total emission. The last non-thermal component extends toward the southeast direction of the cluster. We consider that the thermal component in the XIS spectrum is from the ensemble of point sources plus the thermal diffuse emission at the cluster center, while the ~ 6.4 keV and the accompanying

~ 7.1 keV lines as well as the power-law continuum are from the larger diffuse emission.

In order to compare directly the best-fit spectral model parameters between the ACIS and XIS spectra, we reduced the Chandra ACIS data and obtained the best-fit parameters for the composite of the three brightest point sources and the extended emission. The parameters from XIS and ACIS spectral analysis agree with each other with overlapping 90% confidence ranges. For the thermal component, the XIS spectrum has a temperature of 1.9 (1.5–2.7) keV and the APEC normalization of 3.2 (1.2–7.8) $\times 10^{-3}$ s^{-1} cm^{-2} keV^{-1}, while the ACIS spectrum has 2.0 (1.9–4.4) keV and 2.5 (1.8–3.0) $\times 10^{-3}$ s^{-1} cm^{-2} keV^{-1}. For the power-law component, the photon index in the XIS spectrum is 0.6 (0.3–1.3), while that in the ACIS diffuse spectrum is 1.2 (0.80–1.8). For the Gaussian lines, the photon flux of the ~ 6.4 keV line is 2.4 (2.1–2.7) $\times 10^{-5}$ s^{-1} cm^{-2} in XIS and 2.3 (2.0–2.9) $\times 10^{-5}$ s^{-1} cm^{-2} in ACIS. The equivalent width of the line against the power-law component is ~ 1.24 keV in XIS and ~ 1.25 keV in ACIS, indicating that the power-law flux as well as the line flux is consistent between the two.

5.4.3 Diffuse Medium

The high S/N spectra obtained with the XIS give a stringent constraint on the center energy of the ~ 6.4 keV line, which is an increasing function of the ionization stage of iron. The fluorescent line energy is also affected by whether and how the atom is bound in molecules, but the resultant shifts are negligible of $\sim$1 eV (Paerels, 1998). The best-fit value is consistent with the Kα line from neutral iron (6.40 keV). This is in agreement with the general understanding that most of iron in the ISM is in the form of dust (Sofia et al., 1994). However, slightly low ionization stages are also allowed up to about fourteenth (Fe XV; House 1969), including the systematic uncertainty of the XIS energy gain of ~ 6 eV.

5.4.4 Cause of Line and Power-law Emission

From the XIS spectrum (figure 4.40), we found that the power-law component extends up to ~ 12 keV and dominates the spectrum above ~ 8 keV. From the band-limited XIS images (figure 4.38), we noticed a similarity in the spatial distribution between the 7.5–10.0 keV and the 6.4 keV emission. This indicates that the power-law emission is related to the 6.4 keV line in the underlying physical process. Therefore, the power-law component and the Fe I lines need to be explained simultaneously. The equivalent width of the lines and the normalization of the power-law comprise two major observational tests to discriminate ideas on the origin of the emission. We examine two mechanisms (photoelectric ionization and electron impact ionization) and derive the conditions for the primary ionizing beam. In the

former, the Thomson scattering continuum and the fluorescence are respectively responsible for the power-law and the line emission. In the latter, non-thermal electron bremsstrahlung and the K shell vacancy filling after the electron ionization are considered.

Photoelectric Ionization

We first note that the lack of a prominent absorption edge feature at ~ 7.11 keV alone does not constitute evidence against photoionization (Revnivtsev et al., 2004). This is expected when the reflecting matter is optically-thin to the primary radiation. In fact, the optically-thin approximation is justified by the Chandra result on the Arches cluster, wherein the power-law emission suffers an extinction accountable only by the ISM extinction to the Galactic center region ($\sim 6\times10^{22}$ cm^{-2}; Wang et al. 2006).

We assume that the observed continuum emission does not include the direct X-rays. If it does, the equivalent width of the iron Kα fluorescent line is expected to be $\lesssim$180 eV (Reynolds & Nowak, 2003; Tsujimoto et al., 2005) for the solar abundance, which contradicts the observed value. The equivalent width of the fluorescent line against the Thomson scattering continuum is expressed as a function of the ratio between the photoelectric and Thomson scattering cross sections, the ratio of the target (electron and iron atom) densities, and the geometry; the Thomson scattering is angle-dependent while the fluorescence is spherically symmetric (Liedahl, 1998). Assuming that the incident X-ray spectrum is $I(E)$, the electron and iron densities of the reflecting medium are uniform ($n_{\rm e}$ and $n_{\rm Fe}$, respectively), the photoelectric absorption cross section by iron is $\sigma_{\rm P}^{\rm Fe}(E)$, the differential Thomson scattering cross section is $(d\sigma_{\rm T}/d\Omega)(\theta)$ where θ is the angle between the incident and scattered X-rays, the Kα fluorescence yield is $Y_{\rm K\alpha}$, and the K edge energy is χ, the equivalent width of the Kα line is given by

$$\begin{aligned} {\rm EW}_{\rm K\alpha} &= Y_{\rm K\alpha}\left(\frac{n_{\rm Fe}}{n_{\rm e}}\right)\left(4\pi\frac{d\sigma_{\rm T}}{d\Omega}(\theta)\right)^{-1} \\ &\times \left(\frac{\int_\chi^\infty dE I(E)\sigma_{\rm P}^{\rm Fe}(E)}{I(E=6.4\ {\rm keV})}\right). \end{aligned} \tag{5.1}$$

By substituting $Y_{\rm K\alpha}\sim 0.34$ (Kortright, 2001), $n_{\rm Fe}/n_{\rm e}\sim n_{\rm Fe}/n_{\rm H}\sim 3\times10^{-5}$ (Däppen, 2000) where $n_{\rm H}$ is the hydrogen density, $d\sigma_{\rm T}/d\Omega(\theta)\sim 4.0\times10^{-26}(1+\cos^2\theta)$ cm^2, $I(E)\propto E^{-\Gamma}$, and $\sigma_{\rm P}^{\rm Fe}(E)=2\times10^{-20}(E/7.1\ {\rm keV})^{-3}$ cm^2 (Gullikson, 2001), we obtain

$${\rm EW}_{\rm K\alpha} \sim 3\left(\frac{1}{\Gamma+2}\right)\left(\frac{6.4}{7.1}\right)^{\Gamma}\left(\frac{1}{1+\cos^2\theta}\right)\ {\rm keV}. \tag{5.2}$$

We can determine both ${\rm EW}_{\rm K\alpha}$ and Γ observationally, resulting in $\theta\approx 50$ degrees using the best-fit values. In practice, though, higher accuracy in the parameter determination is

required for a meaningful geometrical constraint. The observed $\mathrm{EW}_{\mathrm{K}\alpha}$ is easily explained by the photoionization interpretation. For the amplitude of continuum emission, the incident flux of $I(E) \sim 3 \times 10^7 (n_{\mathrm{e}}/10^2\ \mathrm{cm}^{-3})^{-1}\ \mathrm{s}^{-1}\ \mathrm{cm}^{-2}\ \mathrm{keV}^{-1}$ is required at 10 keV. Here, the diffuse medium is assumed to have a spherical shape of a 3 pc diameter. The estimate of the electron density is from Rodríguez-Fernández et al. (2001).

To summarize, the photoionization interpretation requires the following conditions: (1) the primary source is an external source, (2) the incident spectrum has a power of $\Gamma \sim 1$ and (3) a photon flux of $\sim 10^7\ \mathrm{s}^{-1}\ \mathrm{cm}^{-2}\ \mathrm{keV}^{-1}$ at 10 keV, (4) the direct emission is optically thin to the reflecting medium (i.e., $n_{\mathrm{H}} < 2 \times 10^5\ \mathrm{cm}^{-2}$), and (5) the reflecting geometry should satisfy the constraint on θ.

No source is found for the primary source in the vicinity at present. The point sources in the Arches cluster can be excluded. This is simply because the continuum emission by the Thomson scattering cannot exceed the illuminating thermal emission above the iron K edge energy, which is contrary to the XIS spectrum showing stronger non-thermal emission than thermal emission at the band (Fig. 4.40). Wang et al. (2006) also discussed that Arches point sources are too dim for the fluorescent lines.

Electron Ionization

Another favored interpretation for the cause of the ~ 6.4 keV line is the vacancy filling after the iron K shell ionization by low energy electrons with an energy of 10–100 keV. This was proposed to explain the Galactic ridge diffuse X-ray emission (Valinia et al., 2000), in which they claimed that the low energy electrons with a density of ~ 0.2 eV cm^{-3} and the power-law spectrum of an index of ~ 0.3 contribute significantly to both the observed line and continuum emission. Yusef-Zadeh et al. (2002b) and Wang et al. (2006) employed this model to account for the ~ 6.4 keV line observed in G0.13–0.13 and the Arches cluster in the Galactic center region, respectively.

The calculation of expected line and continuum intensity of this process requires numerical treatments because of the complex dependence of the cross sections on the electron and X-ray energy. A detailed computation is given in Tatischeff (2002). Two important things have to be considered. First, the electron beam is stopped at the surface of the hydrogen column. The stopping range for 10 and 100 keV electrons is $\sim 7{\times}10^{19} m_{\mathrm{H}}$ and $\sim 4{\times}10^{21} m_{\mathrm{H}}$ g cm^{-2} where m_{H} is the hydrogen mass (Tatischeff, 2002). Second, the energy conversion rate from the electron beam to the X-ray bremsstrahlung is quite small with an order of $\sim 10^{-5}$.

With these kept in mind, we can compare the expected and observed values. The equivalent width of the iron Kα line against the bremsstrahlung continuum is expected to be

~ 290 eV (Tatischeff, 2002), which is smaller than the observed value. An iron abundance of 4–5 times larger than the solar value needs to be introduced to reconcile the discrepancy, though no such indication is present for the Arches cluster. From the spectral fit of the XIS spectrum, we found that a solar abundance for iron accounts for the observed Fe XXV Kα line intensity over the continuum. Wang et al. (2006) suggested that the iron abundance is ~ 2 from the X-ray spectral fits of point sources in the cluster. Najarro et al. (2004) conducted near-infrared spectroscopy of the photospheric emission of Wolf-Rayet stars in the Arches cluster and found that the abundance is consistent with solar.

For the level of continuum emission, we can consult Figure 7 in Tatischeff (2002), which illustrates the X-ray production rate by the low energy electron impact. The injected electrons are assumed to have a total energy rate of 1 erg s^{-1} in an energy range of 10–100 keV and the power-law number density with an index of 2. At 10 keV, a continuum photon production rate of $\sim 8 \times 10$ s^{-1} keV^{-1} is expected. We observed $\sim 1.1 \times 10^{-5}$ s^{-1} cm^{-2} keV^{-1} at 10 keV in the XIS spectrum, which can be converted to $\sim 9.5 \times 10^{40}$ s^{-1} keV^{-1} at a distance of 8 kpc. Therefore, an electron injection rate of $\sim 1 \times 10^{39}$ erg s^{-1} is required. Assuming that the diffuse medium is "optically-thick" to the electron beam, we can derive the required flux of the injected electrons to be $\sim 2 \times 10$ erg s^{-1} cm^{-2} regardless of the target density. Integrating over the entire mass of the medium (Yusef-Zadeh et al., 2002b; Wang et al., 2006) may lead to a significant overestimation.

To summarize, the electron ionization interpretation requires the following conditions: (1) the electron beam has an incident flux of $\sim 2 \times 10^1$ erg s^{-1} cm^{-2} and (2) an index of ~ 2 for the injected power-law number density, and (3) 4–5 times larger abundance than solar for iron in the diffuse medium.

We do not have a list of electron accelerators with an estimated energy injection rate in the Galactic center region and further studies must be undertaken to elucidate the primary source. However, we can at least claim that the accelerated electrons by wind-wind collisions in the Arches cluster (Wang et al., 2006) are unlikely the case. This is simply because the total kinetic energy rate via stellar winds is smaller by an order than the required electron energy injection rate. Here the total energy rate is calculated from an assumed wind velocity of $\sim 10^3$ km s^{-1} and a mass loss rate of $\sim 10^{-4}$ $M_\odot$ yr^{-1} estimated by the free-free emission intensity at the centimeter continuum (Lang et al., 2005).

Protons accelerated via wind-wind collisions to have an MeV energy may cause both the bremsstrahlung and the iron line emission in a similar manner as electrons with several tens of keV. However, because the bremsstrahlung conversion rate for protons is as inefficient as that of electrons (Uchiyama et al., 2002), the protons ionization will encounter the same energy budget deficit.

Finally, heavy ions with an MeV amu^{-1} energy are also capable of producing the con-

tinuum emission by inverse bremsstrahlung and the iron line emission by K shell ionization. In this case, however, the resultant lines are broader and bluer than the case of proton or electron ionization by ~ 50 eV (e.g., Burch et al. 1971), which disagrees with the iron Kα line center determined from the XIS spectrum. Therefore, the ionization by heavy ions can be excluded regardless of whether they are accelerated by wind-wind collisions in the Arches cluster or somewhere else in the Galactic center region.

Chapter 6

Conclusions

In this chapter, we summarize our findings in each studied field and draw general conclusions from cross-regional points of view.

Contents

6.1 A New Wolf-Rayet Star in the Galactic Center

6.1.1 Summary of the Results

From the Galactic center survey, we found that a point-like and bright X-ray source with an intense Fe XXV Kα emission line is a new WR star. The spectrum was well reproduced

by an optically-thin thermal plasma model with a temperature of ~ 4 keV attenuated by an absorption column ($N_{\rm H}$) of $\sim 2 \times 10^{23}$ cm^{-2} and a luminosity of $\sim 3 \times 10^{34} \times (d/8 \text{ kpc})^2$ erg s^{-1} in the 2.0–8.0 keV band. The source has a very red counterpart in the near- and mid-infrared bands. The SED was fitted by a blackbody emission of $\sim 10^3$ K and an extinction of $A_{\rm V} \sim 31$ mag. The high temperature and large luminosity in the X-ray bands suggest that the source is a wind-wind colliding Wolf-Rayet binary. The infrared SED is very similar to those of eponymous Quintuplet cluster members, indicating that this source is a WC type.

6.1.2 Conclusion — Contribution to the Galactic Center Diffuse Emission

The intense 6.7 keV line found in our analysis and the large predicted number of undiscovered WR stars in the Galactic center region (section 2.2) lead us to speculate how much fraction of the Galactic center diffuse emission is accountable by the ensemble of WR stars.

The 6.7 keV line flux from CXOGC J174645.3–281546 is 2.5×10^{-13} erg s^{-1} cm^{-2}. the total flux of iron K-lines in the Galactic center region is $\sim 1.3 \times 10^{-10}$ erg s^{-1} cm^{-2} (Yamauchi et al., 1990). Since this value includes the 6.4 keV and 6.97 keV lines, it overestimates the 6.7 keV flux by a factor of 2–3. The detected point sources account for $\sim 10\%$ of the total flux of the 6.7 keV line (Wang et al., 2002; Muno et al., 2004a). Therefore, the 6.7 keV line of CXOGC J174645.3–281546 alone accounts for $\sim 4\%$ of that of the detected point sources and $\sim 0.4\%$ of that of the total diffuse flux.

The estimated number of WR stars in the inner 1 degree of the Galaxy is ~ 70, and the WR binary frequency is $\sim 39\%$ in the solar neighborhood (van der Hucht, 2001). We hence expect ~ 27 WR binaries in the Galactic center region. If 27 WR binaries have the same iron K line flux with CXOGC J174645.3–281546, $\sim 11\%$ of the iron K line flux in the Galactic center diffuse X-ray emission is explained by WR binaries. It has long been argued that CVs are the main contributor to the Galactic center diffuse X-ray emission (e.g., Wang et al. 2002). However, we propose that binaries of two massive stars such as CXOGC J174645.3–281546 would comprise a substantial fraction of 6.7 keV emission line in the Galactic center.

6.2 Discrete Sources

6.2.1 Summary of the Results

M 17

Although Suzaku did not resolve individual stars of the core of M 17, the major fraction of the X-ray emission from the OB association is due to the central O4–O5 binaries (CEN 1a and CEN 1b). The spectrum is composed of two optically-thin thermal plasma models of $k_{\rm B}T_{\rm low} \sim 0.6$ keV and $k_{\rm B}T_{\rm high} \sim 4$ keV. Suzaku J182132–1613.4 is a newly found source. The infrared brightness is consistent with a B0 V star. The X-ray spectra was well fitted with a high temperature ($k_{\rm B}T \sim 10$ keV) plasma. OI 352 is an isolated O8 star (Ogura & Ishida, 1976). The X-ray spectrum was well reproduced by two thermal components ($k_{\rm B}T_{\rm low} \sim 0.6$ keV and $k_{\rm B}T_{\rm high} \sim 4$ keV).

M17 North is comprised of $\sim$10 point-like sources. The spectrum was well fitted by heavily absorbed ($N_{\rm H} \sim 2 \times 10^{22}$ cm^{-2}) optically-thin thermal plasma model with a temperature of $\sim$3 keV. These spectral values are consistent with embedded protostars. Suzaku J182132–1610.4 shows flare-like time variability, but the IR brightness is inconsistent with low-mass young stellar object located at the distance of M 17. The source is probably a nearby object. The X-ray spectrum of Suzaku J182140–1604.1 is exceptionally hard. The prominent iron K line with an EW of $\sim$ 2 keV suggests a thermal nature of the emission. When fitted by an absorbed optically-thin thermal plasma model, the absorption column is $\sim 10^{24}$ cm^{-2} and the temperature is $\sim$ 13 keV. A possible origin is an embedded protostar.

The Carina Nebula

Hard X-rays with the 6.7 keV line were also found in some massive stars in the Carina region. The X-ray emission of WR 25 (WN6+O4f) in the Carina Nebula is bright ($L_{\rm X} \sim 10^{33.3}$ erg s^{-1} in the 1.0–8.0 keV band), hard ($k_{\rm B}T_{\rm high} \sim 2.3$ keV), and shows a phase-locked flux variation of a factor of $\sim$ 2.

The spectrum of HD 93205 (O3 V+O8 V) was well fitted by a single component with a temperature of $\sim$ 0.25 keV. The flux showed no significant variability among the four observations.

HD 93250 (O3 V, no known companion) has two thermal components of different temperatures ($k_{\rm B}T_{\rm low} \sim 0.6$ keV and $k_{\rm B}T_{\rm high} \sim 3$ keV) with a luminosity of $\sim 10^{32.7}$ erg s^{-1} in the 1.0–8.0 keV band.

The Arches cluster

The Arches cluster is one of the most densely packed young massive star clusters in our Galaxy. Among the 17 WR stars in the cluster, only three sources (A1N, A1S, and A2) were detected from the Chandra observations. The other sources, which are almost identical in infrared and radio properties, are dim in hard X-rays by a factor of more than 100. The three sources have hot thermal components with a temperatures of ~ 2 keV. The luminosities are $10^{33.4}$–$10^{34.2}$ erg s^{-1} in the 2.0–8.0 keV band.

6.2.2 Conclusion — Mechanism for the Hard X-rays from Massive Stars

All discrete massive sources except HD 93205 presented in this thesis have a hard thermal component ($k_{\rm B}T > 2$ keV) with a prominent Fe XXV Kα emission line at ~ 6.7 keV.

In WR 25, we saw that the binary orbital separation is a key parameter in hard X-ray production. The flux decreases as the separation increases. The fact that the X-ray flux modulates with the orbital motion clearly indicates that the X-ray production is a consequence of the binarity.

HD 93205 and the OB association of M 17 (mostly CEN 1a and CEN 1b) are also confirmed to be binaries of two massive stars by optical or NIR observations (Gamen et al., 2006; Conti & Walborn, 1976; Hoffmeister et al., 2008). HD 93205 is the only source that is a binary of two massive stars but lacks hard X-ray emission. The peculiarity of HD 93205 is the small separation of the two massive stars. These facts suggest that the stellar winds collide before the velocity exceed the sound velocity in HD 93205, and the distance between two massive stars should be larger than several times the stellar radius to produce hard X-rays.

The hard X-ray emission from massive stars presented in this thesis and other work is in sharp contrast with the conventional soft emission from single O stars. We deductively speculate that other massive stars with a hot component (A1S, A1N, A2, OI 352, HD 93250, CEN 1a, CEN 1b, and Suzaku J182132–1613.4) are also colliding-wind binaries. Indeed, CEN 1a and CEN 1b are found to have a binary nature. However magnetically-confined wind shock model cannot be excluded (section 2.4), hence monitoring spectroscopy of these objects in the optical and infrared bands is highly encouraged to confirm this hypothesis.

We also consider that not all the X-ray emission is a consequence of colliding winds. In WR 25, we expect a factor of ~ 3.5 in the X-ray flux variation assuming that all X-rays are phase-locked with the orbital modulation of $e = 0.56$, which is actually ~ 2 (table 4.6

and figure 5.6). The discrepancy is also seen in other colliding-wind WR star, WR 140, a smaller amplitude (figure 2.11) than that expected by the eccentricity determined by optical observations. We consider that this discrepancy stems from constant emission, which is probably intrinsic emission of the individual component.

The Arches cluster provides a uniform sample of 17 WR stars: They are located at almost identical distance from us and have similar ages. Among the 17 sources, only three sources are exceptionally bright in X-rays, although the NIR and radio properties are not special among the 17 sources. This indicates that $\sim 20\%$ of WR stars, in general, are colliding-wind binaries and emit hard X-rays.

6.3 Diffuse Sources

6.3.1 Summary of the Results

M 17

We clearly resolved emission lines from highly ionized O, Ne, Mg, and Fe for the first time. The line intensity ratios well constrain the plasma temperature to be ~ 0.25 keV. The absorption column of $\sim 4 \times 10^{21}$ cm^{-2} is typical to M 17. The temperature and chemical composition show no spatial variation across the studied field of ~ 10 pc.

The Carina Nebula

In contrast to M 17, the Carina diffuse emission shows a spatial variation. The emission in the west side of η Carinae shows a low temperature of ~ 0.2 keV, while that in the south side shows a higher temperature of ~ 0.5 keV. The 0.2 keV emission is absorbed with a typical value to this region ($N_{\rm H} \sim 4 \times 10^{21}$ cm^{-2}), while the 0.5 keV emission suffers a small absorption ($N_{\rm H} < 6 \times 10^{20}$ cm^{-2}). Figure 6.1 shows the metal abundances of the diffuse emission in M 17, "diffuse 1 and 2" (south to η Carinae), and "diffuse 3" (west to η Carinae).

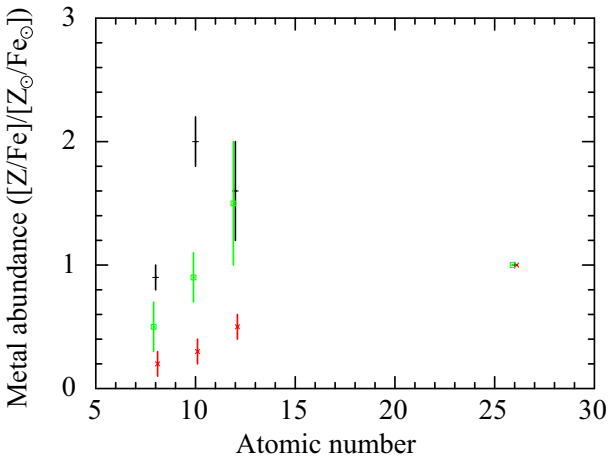

Figure 6.1: Metal abundance relative to Fe in the unit of solar abundances. Data for "Diffuse 1 and 2" and "Diffuse 3" in the Carina Nebula and M 17 are shown in red, green, and black, respectively.

The Arches Cluster

The Arches cluster exhibits a hard diffuse emission with a power-law index of ~ 0.7 and a Gaussian line from Fe I. The 7.5–10.0 keV image is similar to the 6.4 keV image, including the local excess at the Arches cluster, which suggests that the hard continuum and the Gaussian line are physically related.

6.3.2 Conclusion — Various origins of Diffuse Emission in Star-forming Regions

Wind-blown bubble

We consider that the diffuse X-ray emission in M 17 and the west to η Carinae are classical examples of stellar wind bubble. The spectroscopic characterization is presented for the first time for X-ray bubbles in star-forming regions, which has a temperature of ~ 0.2 keV and the O/Fe ratio of $\lesssim 1$ solar.

Table 6.1: Plasma parameters of M 17 and western Carina

Par.	Unit	M 17	Carina
$k_{\rm B}T$	(keV)	0.25	0.18
$n_{\rm e}$	($\rm cm^{-3}$)	1	5
l	(pc)	10	3
$L_{\rm X}$	(10^{33} erg $\rm s^{-1}$)	5	16
$S_{\rm X}$	(10^{-13} erg $\rm s^{-1}$ $\rm cm^{-2}$ $\rm arcmin^{-2}$)	2	2
V	($\rm pc^3$)	100	8
M	($M_\odot$)	2	1.5
$\dot{M}$	($10^{-5} M_\odot$ $\rm yr^{-1}$)	3	4
$E_{\rm th}$	(10^{48} erg)	3	1
$t_{\rm sys}$	(year)	10^6	10^5
$t_{\rm rad}$	(year)	10^7	10^7
$t_{\rm con}$	(year)	30	100

Table 6.1 shows the plasma temperature ($k_{\rm B}T$), the electron density ($n_{\rm e}$), the scale size (l), the X-ray luminosity ($L_{\rm X}$), the X-ray surface brightness ($S_{\rm X}$), the plasma volume (V), the plasma mass (M), the thermal energy ($E_{\rm th} = 3n_{\rm e}k_{\rm B}TV$), the age of the system ($t_{\rm sys}$), the radiative cooling time scale ($t_{\rm rad} = E_{\rm th}/L_{\rm X}$), and the conduction cooling time scale

($t_{\rm con} = E_{\rm th}/\kappa$, where $\kappa = 1.5 \times 10^{-17} \times (dT/dx) \times l^2$ erg s^{-1} is the thermal conductivity; Spitzer 1962) for the diffuse emission of M 17 and the west to η Carinae.

In M 17, if the plasma expands with the sound speed of ~ 250 km s^{-1} and the age of the system of 10^6 years, the size would become ~ 250 pc, which is larger than the observed value by more than ten-fold. This means that the plasma is suppressed or cooled by some sort of mechanism. We see a clear edge at the west end of the diffuse emission with a thickness of ~ 1 pc in M 17 (figure 4.24). This sharp darkening can be attributed to the thermal conduction between the hot plasma and cool ISM accumulated by the winds from OB stars at the core of M 17. Because the thermal conduction time scale is very short (~ 30 year, table 6.1), the cooling scale length is determined by sound speed of the conduction front. Multiplying the age of system ($\sim 10^6$ year), we expect the thickness to be ~ 3 pc, which is roughly consistent with the observed value. The uniform temperature is also justified by the fact that the thermal conduction works only near the contact surface.

It is unclear which star made the diffuse emission in the west to η Carinae. We here assume that WR 25, the closest object, made the stellar wind bubble. Since the mass-loss rate of WR 25 is comparable to that of OB association of M 17, we speculate that the difference of the plasma size between M 17 and west to η Carinae is due to the system age.

Supernova remnants

The other two diffuse sources (Diffuse 1 and 2) show very small absorption column towards the 0.5 keV emission. We argue that the emission is not physically related to the Carina Nebula but originates from a foreground object. A possible origin is a type Ia SNR, which is favored by the high O/Fe value of ~ 5.

Reflection by cold matter

The diffuse emission in the Arches cluster has a hard spectrum, and is obviously different in origin from diffuse emission in M17 and the Carina Nebula. We examined two ideas to account for both the power-law and Gaussian components: (1) X-ray photoionization that produces fluorescence lines and the Thomson scattering continuum and (2) electron impact ionization with subsequent K-shell vacancy filling and bremsstrahlung continuum. We concluded that whichever scenario is adopted, the photon or particle flux from the Arches cluster is too low to yield observed flux.

References

Abbott, D. C. 1980, ApJ, 242, 1183

Abbott, J. B., Crowther, P. A., Drissen, L., Dessart, L., Martin, P., & Boivin, G. 2004, MNRAS, 350, 552

Albacete Colombo, J. F., Méndez, M., & Morrell, N. I. 2003, MNRAS, 346, 704

Albacete Colombo, J. F., Flaccomio, E., Micela, G., Sciortino, S., & Damiani, F. 2007, A&A, 464, 211

Albacete-Colombo, J. F., Damiani, F., Micela, G., Sciortino, S., & Harnden, F. R., Jr. 2008, A&A, 490, 1055

Alves, J., & Homeier, N. 2003, ApJ, 589, L45

Anders, E., & Grevesse, N. 1989, Geochim. Cosmochim. Acta, 53, 197

Ando, M., Nagata, T., Sato, S., Mizuno, N., Mizuno, A., Kawai, T., Nakaya, H., & Glass, I. S. 2002, ApJ, 574, 187

Antokhin, I. I., Rauw, G., Vreux, J.-M., van der Hucht, K. A., & Brown, J. C. 2008, A&A, 477, 593

Antokhina, E. A., Moffat, A. F. J., Antokhin, I. I., Bertrand, J.-F., & Lamontagne, R. 2000, ApJ, 529, 463

Armandroff, T. E., & Massey, P. 1991, AJ, 102, 927

Audard, M., Güdel, M., Sres, A., Raassen, A. J. J., & Mewe, R. 2003, A&A, 398, 1137

Babel, J., & Montmerle, T. 1997, ApJ, 485, L29

Bahcall, J. N. 1969, Scientific American, 221, 29

Bahcall, J. N., Pinsonneault, M. H., & Wasserburg, G. J. 1995, Reviews of Modern Physics, 67, 781

Barlow, M. J., & Hummer, D. G. 1982, Wolf-Rayet Stars: Observations, Physics, Evolution, 99, 387

Bautz, M. W., Kissel, S. E., Prigozhin, G. Y., LaMarr, B., Burke, B. E., & Gregory, J. A. 2004, Proc. SPIE, 5501, 111

Beals, C. S. 1938, Trans. IAU, 6, 248

Bearden, J. A. 1967, Reviews of Modern Physics, 39, 78

Becklin, E. E., & Neugebauer, G. 1968, ApJ, 151, 145

Benjamin, R. A., et al. 2003, PASP, 115, 953

Benvenuto, O. G., Serenelli, A. M., Althaus, L. G., Barbá, R. H., & Morrell, N. I. 2002, MNRAS, 330, 435

Berghoefer, T. W., Schmitt, J. H. M. M., Danner, R., & Cassinelli, J. P. 1997, A&A, 322, 167

Bland-Hawthorn, J., & Cohen, M. 2003, ApJ, 582, 246

Blum, R. D., Schaerer, D., Pasquali, A., Heydari-Malayeri, M., Conti, P. S., & Schmutz, W. 2001, AJ, 122, 1875

Bochkarev, N. G. 1988, Nature, 332, 518

Boldt, E. 1987, Phys. Rep., 146, 215

Bouchet, L., et al. 1991, ApJ, 383, L45

Breysacher, J., Azzopardi, M., & Testor, G. 1999, A&AS, 137, 117

Brinkman, A. C., et al. 2001, A&A, 365, L324

Brogan, C. L., & Troland, T. H. 2001, ApJ, 560, 821

Broos, P. S., Townsley, L. K., Getman, K. V., Bauer, F. E., ACIS Extract, An ACIS Point Source Extraction Package (University Park: The Pennsylvania State Univ.) `http://www.astro.psu.edu/xray/docs/TARA/ae_users_guide.html`

Broos, P. S., Feigelson, E. D., Townsley, L. K., Getman, K. V., Wang, J., Garmire, G. P., Jiang, Z., & Tsuboi, Y. 2007, ApJS, 169, 353

Burch, D., Richartd, P., Blake, R. L. 1971, Phys. Rev. Lett., 26, 1355

Campbell, B., et al. 1992, AJ, 104, 1721

Cantó, J., Raga, A. C., & Rodríguez, L. F. 2000, ApJ, 536, 896

Cappellari, M., & Copin, Y. 2003, MNRAS, 342, 345

Castor, J. I., Abbott, D. C., & Klein, R. I. 1975, ApJ, 195, 157

Catchpole, R. M., Whitelock, P. A., & Glass, I. S. 1990, MNRAS, 247, 479

Chini, R., Elsaesser, H., & Neckel, T. 1980, A&A, 91, 186

Chiosi, C., & Maeder, A. 1986, ARA&A, 24, 329

Chrysostomou, A., Brand, P. W. J. L., Burton, M. G., & Moorhouse, A. 1992, MNRAS, 256, 528

Chu, Y. H. 1991, Wolf-Rayet Stars and Interrelations with Other Massive Stars in Galaxies, 143, 349

Chu, Y.-H., Chang, H.-W., Su, Y.-L., & Mac Low, M.-M. 1995, ApJ, 450, 157

Chu, Y.-H., Guerrero, M. A., Gruendl, R. A., García-Segura, G., & Wendker, H. J. 2003, ApJ, 599, 1189

Churchwell, E. 1990, A&A Rev., 2, 79

Clark, J. S., Negueruela, I., Crowther, P. A., & Goodwin, S. P. 2005, A&A, 434, 949

Conti, P. S., & Walborn, N. R. 1976, ApJ, 207, 502

Conti, P. S., & Blum, R. D. 2002, ApJ, 564, 827

Corcoran, M. F., et al. 2001, ApJ, 562, 1031

Cotera, A. S., Erickson, E. F., Colgan, S. W. J., Simpson, J. P., Allen, D. A., & Burton, M. G. 1996, ApJ, 461, 750

Cox, A. N. 2000, Allen's Astrophysical Quantities

Crowther, P. A., Hillier, D. J., & Smith, L. J. 1995, A&A, 293, 403

Crowther, P. A., Hadfield, L. J., Clark, J. S., Negueruela, I., & Vacca, W. D. 2006, MNRAS, 372, 1407

Cutri, R. M., et al. 2003, The IRSA 2MASS All-Sky Point Source Catalog, NASA/IPAC Infrared Science Archive. http://irsa.ipac.caltech.edu/applications/Gator/,

Däppen, W. 2000, in Allen's Astrophysical Quantities, ed. A. N. Cox (New York: Springer-Verlag), 27

Davidson, K., & Humphreys, R. M. 1997, ARA&A, 35, 1

De Becker, M., Rauw, G., Sana, H., Pollock, A. M. T., Pittard, J. M., Blomme, R., Stevens, I. R., & van Loo, S. 2006, MNRAS, 371, 1280

Diehl, S., & Statler, T. S. 2006, MNRAS, 368, 497

Donati, J.-F., Babel, J., Harries, T. J., Howarth, I. D., Petit, P., & Semel, M. 2002, MNRAS, 333, 55

Drake, J. J., & Testa, P. 2005, Nature, 436, 525

Dunne, B. C., Chu, Y.-H., Chen, C.-H. R., Lowry, J. D., Townsley, L., Gruendl, R. A., Guerrero, M. A., & Rosado, M. 2003, ApJ, 590, 306

Ebisawa, K., Maeda, Y., Kaneda, H., & Yamauchi, S. 2001, Science, 293, 1633

Ebisawa, K., et al. 2005, ApJ, 635, 214

Egan, M. P., et al. 2003, VizieR Online Data Catalog, 5114, 0

Evans, N. R., Seward, F. D., Krauss, M. I., Isobe, T., Nichols, J., Schlegel, E. M., & Wolk, S. J. 2003, ApJ, 589, 509

Evans, N. R., Schlegel, E. M., Waldron, W. L., Seward, F. D., Krauss, M. I., Nichols, J., & Wolk, S. J. 2004, ApJ, 612, 1065

Ezuka, H., & Ishida, M. 1999, ApJS, 120, 277

Feigelson, E. D., Broos, P., Gaffney, J. A., III, Garmire, G., Hillenbrand, L. A., Pravdo, S. H., Townsley, L., & Tsuboi, Y. 2002, ApJ, 574, 258

Feigelson, E. D., et al. 2005, ApJS, 160, 379

Feinstein, A. 1995, Revista Mexicana de Astronomia y Astrofisica Conference Series, 2, 57

Feldmeier, A. 1995, A&A, 299, 523

Feldmeier, A., Kudritzki, R.-P., Palsa, R., Pauldrach, A. W. A., & Puls, J. 1997, A&A, 320, 899

Felli, M., Massi, M., & Churchwell, E. 1984, A&A, 136, 53

Figer, D. F., McLean, I. S., & Morris, M. 1999a, ApJ, 514, 202

Figer, D. F., Kim, S. S., Morris, M., Serabyn, E., Rich, R. M., & McLean, I. S. 1999b, ApJ, 525, 750

Figer, D. F., et al. 2002, ApJ, 581, 258

Figer, D. F., Rich, R. M., Kim, S. S., Morris, M., & Serabyn, E. 2004, ApJ, 601, 319

Figer, D. F. 2005, Nature, 434, 192

Fitzgerald, M. P., & Mehta, S. 1987, MNRAS, 228, 545

Fujimoto, R., et al. 2007, PASJ, 59, S133

Gagné, M., Caillault, J.-P., Stauffer, J. R., & Linsky, J. L. 1997, ApJ, 478, L87

Gagné, M., Oksala, M. E., Cohen, D. H., Tonnesen, S. K., ud-Doula, A., Owocki, S. P., Townsend, R. H. D., & MacFarlane, J. J. 2005, ApJ, 628, 986

Gallo, E., & Fender, R. P. 2002, MNRAS, 337, 869

Gamen, R., et al. 2006, A&A, 460, 777

Gamen, R., et al. 2008, Revista Mexicana de Astronomia y Astrofisica Conference Series, 33, 91

Garmire, G. P., Bautz, M. W., Ford, P. G., Nousek, J. A., & Ricker, G. R., Jr. 2003, Proc. SPIE, 4851, 28

Getman, K. V., et al. 2005, ApJS, 160, 319

Getman, K. V., Feigelson, E. D., Broos, P. S., Micela, G., & Garmire, G. P. 2008, ApJ, 688, 418

Ghez, A. M., Salim, S., Hornstein, S. D., Tanner, A., Lu, J. R., Morris, M., Becklin, E. E., & Duchêne, G. 2005, ApJ, 620, 744

Grosdidier, Y., Moffat, A. F. J., Joncas, G., & Acker, A. 1998, ApJ, 506, L127

Gruber, D. E., Matteson, J. L., Peterson, L. E., & Jung, G. V. 1999, ApJ, 520, 124

Güdel, M., Briggs, K. R., Montmerle, T., Audard, M., Rebull, L., & Skinner, S. L. 2008, Science, 319, 309

Gullikson, E. M. 2001, in X-ray Data Booklet, ed. A. Thompson et al. (Berkeley: University of California), 1-38

Hanson, M. M., Howarth, I. D., & Conti, P. S. 1997, ApJ, 489, 698

Hamaguchi, K., et al. 2007, PASJ, 59, 151

Hamaguchi, K., et al. 2007b, ApJ, 663, 522

Harnden, F. R., Jr., et al. 1979, ApJ, 234, L51

Hellier, C., & Mukai, K. 2004, MNRAS, 352, 1037

Henning, T., Klein, R., Launhardt, R., Lemke, D., & Pfau, W. 1998, A&A, 332, 1035

Henley, D. B., Corcoran, M. F., Pittard, J. M., Stevens, I. R., Hamaguchi, K., & Gull, T. R. 2008, ApJ, 680, 70

Hillier, D. J., Davidson, K., Ishibashi, K., & Gull, T. 2001, ApJ, 553, 837

Hoffmeister, V. H., Chini, R., Scheyda, C. M., Schulze, D., Watermann, R., Nürnberger, D., & Vogt, N. 2008, ApJ, 686, 310

House, L. L. 1969, ApJS, 18, 21

Hyodo, Y., Tsujimoto, M., Hamaguchi, K., Koyama, K., Kitamoto, S., Maeda, Y., Tsuboi, Y., & Ezoe, Y. 2008a, PASJ, 60, 85

Hyodo, Y., Tsujimoto, M., Koyama, K., Nishiyama, S., Nagata, T., Sakon, I., Murakami, H., & Matsumoto, H. 2008b, PASJ, 60, 173

Imanishi, K., Koyama, K., & Tsuboi, Y. 2001, ApJ, 557, 747

Imanishi, K., Nakajima, H., Tsujimoto, M., Koyama, K., & Tsuboi, Y. 2003, PASJ, 55, 653

Inoue, H. 1985, Space Science Reviews, 40, 317

Ishisaki, Y., et al. 2007, PASJ, 59, S113

Jansen, F., et al. 2001, A&A, 365, L1

Jiang, Z., et al. 2002, ApJ, 577, 245

Kaneda, H., Makishima, K., Yamauchi, S., Koyama, K., Matsuzaki, K., & Yamasaki, N. Y. 1997, ApJ, 491, 638

Kastner, J. H., Huenemoerder, D. P., Schulz, N. S., Canizares, C. R., & Weintraub, D. A. 2002, ApJ, 567, 434

Kelley, R. L., et al. 2007, PASJ, 59, S77

Kim, S. S., Morris, M., & Lee, H. M. 1999, ApJ, 525, 228

Kobayashi, Y., Okuda, H., Sato, S., Jugaku, J., & Dyck, H. M. 1983, PASJ, 35, 101

Kokubun, M., et al. 2007, PASJ, 59, 53

Kortright, J. B. 2001, in X-ray Data Booklet, ed. A. Thompson et al. (Berkeley: University of California), 1-28

Koyama, K., Awaki, H., Kunieda, H., Takano, S., & Tawara, Y. 1989, Nature, 339, 603

Koyama, K., Maeda, Y., Tsuru, T., Nagase, F., & Skinner, S. 1994, PASJ, 46, L93

Koyama, K., Maeda, Y., Sonobe, T., Takeshima, T., Tanaka, Y., & Yamauchi, S. 1996, PASJ, 48, 249

Koyama, K., et al. 2007a, PASJ, 59, S23

Koyama, K., et al. 2007b, PASJ, 59, S221

Koyama, K., et al. 2007c, PASJ, 59, 245

Krabbe, A., et al. 1995, ApJ, 447, L95

Krause, M. O., & Oliver, J. H. 1979, Journal of Physical and Chemical Reference Data, 8, 329

Lada, C. J., Depoy, D. L., Merrill, K. M., & Gatley, I. 1991, ApJ, 374, 533

Lang, C. C., Goss, W. M., & Morris, M. 2001, AJ, 121, 2681

Lang, C. C., Johnson, K. E., Goss, W. M., & Rodríguez, L. F. 2005, AJ, 130, 2185

Law, C., & Yusef-Zadeh, F. 2004, ApJ, 611, 858

Leitherer, C., Robert, C., & Drissen, L. 1992, ApJ, 401, 596

Levato, H., Malaroda, S., Morrell, N., Garcia, B., & Hernandez, C. 1991, ApJS, 75, 869

Lewin, W. H. G., et al. 1976, MNRAS, 177, 83P

Liedahl, D. A. 1998, in Lecture Notes in Physics vol. 520, ed. J. van Paradijs, & J. A. M. Bleeker (Berlin: Springer-Verlag), 189

Liefke, C., & Schmitt, J. H. M. M. 2006, A&A, 458, L1

Lucy, L. B., & Solomon, P. M. 1970, ApJ, 159, 879

Lucy, L. B. 1974, AJ, 79, 745

Lucy, L. B. 1982, ApJ, 255, 286

Lucy, L. B., & White, R. L. 1980, ApJ, 241, 300

Maeda, Y., Koyama, K., Yokogawa, J., & Skinner, S. 1999, ApJ, 510, 967

Maeder, A., & Meynet, G. 1987, A&A, 182, 243

Maeder, A. 1990, A&AS, 84, 139

Maggio, A., Flaccomio, E., Favata, F., Micela, G., Sciortino, S., Feigelson, E. D., & Getman, K. V. 2007, ApJ, 660, 1462

Marchenko, S. V., et al. 2003, ApJ, 596, 1295

Massey, P., Johnson, K. E., & Degioia-Eastwood, K. 1995, ApJ, 454, 151

Massey, P., & Johnson, O. 1998, ApJ, 505, 793

Massey, P., & Duffy, A. S. 2001, ApJ, 550, 713

Massey, P., Olsen, K. A. G., & Parker, J. W. 2003, PASP, 115, 1265

Mauerhan, J. C., Muno, M. P., & Morris, M. 2007, ApJ, 662, 574

McCarthy, P. J., van Breugel, W., & Heckman, T. 1987, AJ, 93, 264

Mereghetti, S., Sidoli, L., & Israel, G. L. 1998, A&A, 331, L77

Meynet, G., & Maeder, A. 2005, A&A, 429, 581

Mikles, V. J., Eikenberry, S. S., Muno, M. P., Bandyopadhyay, R. M., & Patel, S. 2006, ApJ, 651, 408

Mitsuda, K., et al. 2007, PASJ, 59, S1

Moffat, A. F. J. 1983, A&A, 124, 273

Moffat, A. F. J., & Shara, M. M. 1987, ApJ, 320, 266

Moffat, A. F. J. 2008, Revista Mexicana de Astronomia y Astrofisica Conference Series, 33, 95

Moneti, A., Stolovy, S., Blommaert, J. A. D. L., Figer, D. F., & Najarro, F. 2001, A&A, 366, 106

Monnier, J. D., Tuthill, P. G., & Danchi, W. C. 1999, ApJ, 525, L97

Morrell, N. I., et al. 2001, MNRAS, 326, 85

Morris, M., & Serabyn, E. 1996, ARA&A, 34, 645

Morrison, R., & McCammon, D. 1983, ApJ, 270, 119

Muno, M. P., et al. 2003, ApJ, 589, 225

Muno, M. P., et al. 2004a, ApJ, 613, 326

Muno, M. P., et al. 2004b, ApJ, 613, 1179

Muno, M. P., Bower, G. C., Burgasser, A. J., Baganoff, F. K., Morris, M. R., & Brandt, W. N. 2006a, ApJ, 638, 183

Muno, M. P., Bauer, F. E., Bandyopadhyay, R. M., & Wang, Q. D. 2006b, ApJS, 165, 173

Murakami, H., Koyama, K., Sakano, M., Tsujimoto, M., & Maeda, Y. 2000, ApJ, 534, 283

Murakami, H., Koyama, K., & Maeda, Y. 2001, ApJ, 558, 687

Najarro, F., Figer, D. F., Hillier, D. J., & Kudritzki, R. P. 2004, ApJ, 611, L105

Nagashima, C., et al. 1999, Proceedings of Star Formation 1999, ed. T. Nakamoto, Nobeyama Radio Observatory, 397

Nagata, T., Woodward, C. E., Shure, M., Pipher, J. L., & Okuda, H. 1990, ApJ, 351, 83

Nagata, T., Woodward, C. E., Shure, M., & Kobayashi, N. 1995, AJ, 109, 1676

Nagayama, T., et al. 2003, Proc. SPIE, 4841, 459

Nakajima, H., et al. 2008, PASJ, 60, 1

Nielbock, M., Chini, R., Jütte, M., & Manthey, E. 2001, A&A, 377, 273

Nishiyama, S., et al. 2006, ApJ, 638, 839

Nomoto, K., Hashimoto, M., Tsujimoto, T., Thielemann, F.-K., Kishimoto, N., Kubo, Y., & Nakasato, N. 1997, Nuclear Physics A, 616, 79

Ogura, K., & Ishida, K. 1976, PASJ, 28, 35

Okuda, H., et al. 1989, The Center of the Galaxy, 136, 281

Okuda, H., et al. 1990, ApJ, 351, 89

Oskinova, L. M., Ignace, R., Hamann, W.-R., Pollock, A. M. T., & Brown, J. C. 2003, A&A, 402, 755

Owocki, S. P., & Cohen, D. H. 1999, ApJ, 520, 833

Ozawa, H., Grosso, N., & Montmerle, T. 2005, A&A, 438, 661

Ozawa, M., et al. 2009, PASJ, 61, accepted

Paerels, F. 1998, in Lecture Notes in Physics vol. 520, ed. J. van Paradijs, & J. A. M. Bleeker (Berlin: Springer-Verlag), 347

Paczynski, B. 1973, Wolf-Rayet and High-Temperature Stars, 49, 143

Pallavicini, R., Golub, L., Rosner, R., Vaiana, G. S., Ayres, T., & Linsky, J. L. 1981, ApJ, 248, 279

Park, S., Muno, M. P., Baganoff, F. K., Maeda, Y., Morris, M., Howard, C., Bautz, M. W., & Garmire, G. P. 2004, ApJ, 603, 548

Pavlinsky, M. N., Grebenev, S. A., & Sunyaev, R. A. 1994, ApJ, 425, 110

Pellegrini, E. W., et al. 2007, ApJ, 658, 1119

Petrovic, J., Langer, N., Yoon, S.-C., & Heger, A. 2005, A&A, 435, 247

Pfeffermann, E., et al. 1987, Proc. SPIE, 733, 519

Pollock, A. M. T. 1987, ApJ, 320, 283

Pollock, A. M. T., Corcoran, M. F., & Stevens, I. R. 2002, Interacting Winds from Massive Stars, 260, 537

Pollock, A. M. T., Corcoran, M. F., Stevens, I. R., & Williams, P. M. 2005, ApJ, 629, 482

Pollock, A. M. T., & Corcoran, M. F. 2006, A&A, 445, 1093

Porquet, D., Decourchelle, A., & Warwick, R. S. 2003, A&A, 401, 197

Portegies Zwart, S. F., Makino, J., McMillan, S. L. W., & Hut, P. 2001, ApJ, 546, L101

Portegies Zwart, S. F., Makino, J., McMillan, S. L. W., & Hut, P. 2002a, ApJ, 565, 265

Portegies Zwart, S. F., Pooley, D., & Lewin, W. H. G. 2002b, ApJ, 574, 762

Povich, M. S., et al. 2007, ApJ, 660, 346

Predehl, P., & Schmitt, J. H. M. M. 1995, A&A, 293, 889

Predehl, P., Costantini, E., Hasinger, G., & Tanaka, Y. 2003, Astronomische Nachrichten, 324, 73

Raassen, A. J. J., van der Hucht, K. A., Mewe, R., Antokhin, I. I., Rauw, G., Vreux, J.-M., Schmutz, W., Güdel, M. 2003, A&A, 402, 653

Raga, A. C., Velázquez, P. F., Cantó, J., Masciadri, E., & Rodríguez, L. F. 2001, ApJ, 559, L33

Rana, V. R., Singh, K. P., Schlegel, E. M., & Barrett, P. E. 2006, ApJ, 642, 1042

Rauw, G., et al. 2005, A&A, 432, 985

Rayner, J. T., Toomey, D. W., Onaka, P. M., Denault, A. J., Stahlberger, W. E., Vacca, W. D., Cushing, M. C., & Wang, S. 2003, PASP, 115, 362

Reeves, J. N., et al. 2007, PASJ, 59, 301

Revnivtsev, M. G., et al. 2004, A&A, 425, L49

Revnivtsev, M., Molkov, S., & Sazonov, S. 2006, MNRAS, 373, L11

Raymond, J. C., & Smith, B. W. 1977, ApJS, 35, 419

Reynolds, C. S., & Nowak, M. A. 2003, Phys. Rep., 377, 389

Rockefeller, G., Fryer, C. L., Melia, F., & Wang, Q. D. 2005, ApJ, 623, 171

Rodríguez-Fernández, N. J., Martín-Pintado, J., & de Vicente, P. 2001, A&A, 377, 631

Sakano, M., Imanishi, K., Tsujimoto, M., Koyama, K., & Maeda, Y. 1999, ApJ, 520, 316

Sanchawala, K., Chen, W.-P., Lee, H.-T., Chu, Y.-H., Nakajima, Y., Tamura, M., Baba, D., & Sato, S. 2007, ApJ, 656, 462

Schaller, G., Schaerer, D., Meynet, G., & Maeder, A. 1992, A&AS, 96, 269

Schultheis, M., et al. 1999, A&A, 349, L69

Sekiguchi, A., et al. 2008, PASJ, in prep.

Serabyn, E., Shupe, D., & Figer, D. F. 1998, Nature, 394, 448

Seward, F. D., Forman, W. R., Giacconi,R., Griffiths, R. E., Harnden, F. R., Jr., Jones, C., & Pye, J. P. 1979, ApJ, 234, L55

Seward, F. D., & Chlebowski, T. 1982, ApJ, 256, 530

Serlemitsos, P. J., et al. 2007, PASJ, 59, S9

Shibata, K., & Yokoyama, T. 1999, ApJ, 526, L49

Shore, S. N., & Brown, D. N. 1990, ApJ, 365, 665

Sidoli, L., Mereghetti, S., Israel, G. L., Chiappetti, L., Treves, A., & Orlandini, M. 1999, ApJ, 525, 215

Sidoli, L., Mereghetti, S., Israel, G. L., & Bocchino, F. 2000, A&A, 361, 719

Silich, S., Tenorio-Tagle, G., & Rodríguez-González, A. 2004, ApJ, 610, 226

Skinner, S. L., Itoh, M., & Nagase, F. 1998, New Astronomy, 3, 37

Skinner, S. L., Itoh, M., Nagase, F., & Zhekov, S. A. 1999, ApJ, 524, 394

Skinner, S. L., Zhekov, S. A., Güdel, M., & Schmutz, W. 2002, ApJ, 572, 477

Skrutskie, M. F., et al. 2006, AJ, 131, 1163

Smith, L. F. 1968, MNRAS, 138, 109

Smith, L. F., Shara, M. M., & Moffat, A. F. J. 1996, MNRAS, 281, 163

Smith, N., Egan, M. P., Carey, S., Price, S. D., Morse, J. A., & Price, P. A. 2000, ApJ, 532, L145

Smith, R. K., Brickhouse, N. S., Liedahl, D. A., & Raymond, J. C. 2001, ApJ, 556, L91

Smith, N. 2006, MNRAS, 367, 763

Snowden, S. L., Egger, R., Finkbeiner, D. P., Freyberg, M. J., & Plucinsky, P. P. 1998, ApJ, 493, 715

Soderberg, A. M., et al. 2008, Nature, 453, 469

Sofia, U. J., Cardelli, J. A., & Savage, B. D. 1994, ApJ, 430, 650

Spitzer, L. 1962, Physics of Fully Ionized Gases, New York: Interscience (2nd edition), 1962,

Stahl, O., Wolf, B., Gang, T., Gummersbach, C. A., Kaufer, A., Kovacs, J., Mandel, H., & Szeifert, T. 1993, A&A, 274, L29

Stelzer, B., & Schmitt, J. H. M. M. 2004, A&A, 418, 687

Stevens, I. R., Blondin, J. M., & Pollock, A. M. T. 1992, ApJ, 386, 265

Stevens, I. R., Corcoran, M. F., Willis, A. J., Skinner, S. L., Pollock, A. M. T., Nagase, F., & Koyama, K. 1996, MNRAS, 283, 589

Stolte, A., Grebel, E. K., Brandner, W., & Figer, D. F. 2002, A&A, 394, 459

Strüder, L., et al. 2001, A&A, 365, L18

Sugizaki, M., Mitsuda, K., Kaneda, H., Matsuzaki, K., Yamauchi, S., & Koyama, K. 2001, ApJS, 134, 77

Sunyaev, R. A., Markevitch, M., & Pavlinsky, M. 1993, ApJ, 407, 606

Takahashi, T., et al. 2007, PASJ, 59, 35

Takahashi, T., et al. 2008, PASJ, 60, 131

Tatischeff, V. 2002, astro-ph/0208397

Tawa, N., et al. 2008, PASJ, 60, 11

Terada, Y., Ishida, M., Makishima, K., Imanari, T., Fujimoto, R., Matsuzaki, K., & Kaneda, H. 2001, MNRAS, 328, 112

Thielemann, F.-K., Nomoto, K., & Hashimoto, M.-A. 1996, ApJ, 460, 408

Townsley, L. K., Feigelson, E. D., Montmerle, T., Broos, P. S., Chu, Y.-H., & Garmire, G. P. 2003, ApJ, 593, 874

Townsley, L. K., Broos, P. S., Feigelson, E. D., Garmire, G. P., & Getman, K. V. 2006, AJ, 131, 2164

Truemper, J. 1982, Advances in Space Research, 2, 241

Tsuboi, Y., Koyama, K., Sakano, M., & Petre, R. 1997, PASJ, 49, 85

Tsuboi, Y., Koyama, K., Murakami, H., Hayashi, M., Skinner, S., & Ueno, S. 1998, ApJ, 503, 894

Tsujimoto, T., Nomoto, K., Yoshii, Y., Hashimoto, M., Yanagida, S., & Thielemann, F.-K. 1995, MNRAS, 277, 945

Tsujimoto, M., Feigelson, E. D., Grosso, N., Micela, G., Tsuboi, Y., Favata, F., Shang, H., & Kastner, J. H. 2005, ApJS, 160, 503

Tsujimoto, M., et al. 2007b, ApJ, 665, 719

Tucker, W. H., & Gould, R. J. 1966, ApJ, 144, 244

Turner, M. J. L., et al. 2001, A&A, 365, L27

Tuthill, P. G., Monnier, J. D., & Danchi, W. C. 1999, Nature, 398, 487

Tuthill, P., Monnier, J., Tanner, A., Figer, D., Ghez, A., & Danchi, W. 2006, Science, 313, 935

Uchiyama, Y., Takahashi, T., & Aharonian, F. A. 2002, PASJ, 54, L73

Uchiyama, Y., et al. 2008, PASJ, 60, 35

Uchiyama, H., et al. 2009, PASJ, 61, accepted

Valinia, A., Tatischeff, V., Arnaud, K., Ebisawa, K., & Ramaty, R. 2000, ApJ, 543, 733

van der Hucht, K. A., Conti, P. S., Lundstrom, I., & Stenholm, B. 1981, Space Science Reviews, 28, 227

van der Hucht, K. A. 2001, New Astronomy Review, 45, 135

van der Hucht, K. A. 2006, A&A, 458, 453

Wang, Q. D., Gotthelf, E. V., & Lang, C. C. 2002, Nature, 415, 148

Wang, Q. D., Dong, H., & Lang, C. 2006, MNRAS, 371, 38

Weaver, R., McCray, R., Castor, J., Shapiro, P., & Moore, R. 1977, ApJ, 218, 377

Weisskopf, M. C., Brinkman, B., Canizares, C., Garmire, G., Murray, S., & Van Speybroeck, L. P. 2002, PASP, 114, 1

Werner, M. W., et al. 2004, ApJS, 154, 1

White, N. E., Giommi, P., & Angelini, L. 1994, IAU Circ., 6100, 1

Williams, P. M., van der Hucht, K. A., & The, P. S. 1987, A&A, 182, 91

Wilson, T. L., Fazio, G. G., Jaffe, D., Kleinmann, D., Wright, E. L., & Low, F. J. 1979, A&A, 76, 86

Wilson, T. L., Hanson, M. M., & Muders, D. 2003, ApJ, 590, 895

Wolf, C. J., & Rayet, G. 1867, Comptes Rendus Acad.Sci., 65, 292

Wood, D. O. S., & Churchwell, E. 1989, ApJ, 340, 265

Wrigge, M., Wendker, H. J., & Wisotzki, L. 1994, A&A, 286, 219

Wrigge, M. 1999, A&A, 343, 599

Yamauchi, S., Kawada, M., Koyama, K., Kunieda, H., & Tawara, Y. 1990, ApJ, 365, 532

Yamauchi, S., Koyama, K., Sakano, M., & Okada, K. 1996, PASJ, 48, 719

Yang, Y., Park, H. S., Lee, M. G., & Lee, S.-G. 2002, Journal of Korean Astronomical Society, 35, 131

Yusef-Zadeh, F., Law, C., Wardle, M., Wang, Q. D., Fruscione, A., Lang, C. C., & Cotera, A. 2002, ApJ, 570, 665

Yusef-Zadeh, F., Law, C., & Wardle, M. 2002b, ApJ, 568, L121

Acknowledgments

My deepest appreciation goes to Katsuji Koyama who introduced me to the X-ray astronomy and has been patiently encouraging me throughout my graduate course. I would like to express my gratitude to Masahiro Tsujimoto for his continuous mentoring on this work. I am grateful to Takeshi Go Tsuru and Hironori Matsumoto whose meticulous comments were of enormous help.

I would also like to thank to Hideki Uchiyama and Midori Ozawa who informed me of the latest information on the XIS calibration.

For the NIR study, I am indebted to Tetsuya Nagata and Shogo Nishiyama who offered me the SIRIUS data and gave me constructive comments. I appreciate Itsuki Sakon for his invaluable comments on the analysis of the MIR data.

My gratitude is also for Makoto Sawada and Masayoshi Nobukawa for making figures in this work and checking the manuscript. Aya Bamba, Hiroya Yamaguchi, Yoshitomo Maeda, Yohko Tsuboi, Kenji Hamaguchi, Yuichiro Ezoe, Shunji Kitamoto, and Hiroshi Murakami gave me insightful comments and suggestions.

I acknowledge financial support from the Japan Society for the Promotion of Science. The work is financially supported by the grants-in-aid for a 21st century center of excellence program "Center for Diversity and Universality in Physics" and the Global COE Program "The Next Generation of Physics, Spun from Universality and Emergence" by the Ministry of Education, Culture, Sports, Science and Technology of Japan.

This research has made use of data obtained from the Data ARchive and Transmission System at ISAS/JAXA, the High Energy Astrophysics Science Archive Research Center at the NASA/Goddard Space Flight Center, and the Two Micron All Sky Survey, which is a joint project of the University of Massachusetts and the Infrared Processing and Analysis Center/California Institute of Technology, funded by the National Aeronautics and Space Administration and the National Science Foundation. MSX was funded by the Ballistic Missile Defense Organization with additional support from NASA Office of Space Science. This research has also made use of the NASA/IPAC Infrared Science Archive, which is

operated by the Jet Propulsion Laboratory, California Institute of Technology, under contract with the National Aeronautics and Space Administration.